Fabrication Optimisation of Metal-Oxide-Metal Diodes

Linzi Emma Dodd

A Thesis presented for the degree of
Doctor of Philosophy

School of Engineering and Computing Sciences
Durham University

February 2014

Fabrication Optimisation of Metal-Oxide-Metal Diodes

Abstract

This thesis is based on the design, research and development of devices required to successfully recover waste heat and convert it into electrical power through the use of Microsystems Technology. This takes place using optical nano-antennas, in the same way a radio antenna picks up a radio station. The main aim of this project is the rectification of this signal into a useful DC voltage. Here we have used high frequency metal-oxide-metal (MOM) diodes, which involve the use of two dissimilar metals separated by a native oxide.

In order to make successful MOM diodes, the following must be considered: maximise the work function difference between the metals for asymmetry in I-V characteristics, produce a uniform oxide layer that is sufficiently thin (a few nm) for electron tunnelling to occur and reduce the diode size to sub-micron dimensions to increase the cut-off frequency. Currently the diodes consist of titanium, titanium oxide and platinum, which provides a high enough work function difference that the I-V characteristics show significant asymmetry and figure of merit values are among the best published. It has been found, using ToFSIMS and TEM analysis of the oxide, that the thickness of the oxide can be controlled between 1 nm and 7 nm using RIE etching and subsequent oxygen plasma regrowth. Different oxides have been fabricated with different stoichiometries depending on the process used. Furnace oxidation grows a complex oxide in the range 6.9 to 7.6 nm thick. By contrast a more simple oxide can be produced using a controlled reactive ion etch and subsequent plasma oxidation, with thicknesses in the range 1 to 6 nm.

The final significant issue involves the cross-sectional area of the diodes, which also determines their cut-off frequency. Extrapolation of existing diode results suggests that, if made sufficiently small, they would function at high enough frequencies for rectification of radiation in the terahertz regime. Furthermore, phase shift lithography has been used to demonstrate 200 to 400 nm lines in diode features, with alternative possible high scale processes discussed for future fabrication.

Declaration

The work in this thesis is based on research carried out at the School of Engineering and Computing Sciences, Durham University, England. No part of this thesis has been submitted elsewhere for any other degree or qualification and it is all my own work unless referenced to the contrary in the text.

Acknowledgements

I would like to thank my two supervisors, Prof. David Wood and Dr Andrew Gallant, for their endless support and thought provoking discussions throughout this project. I'd also like to thank Dr Claudio Balocco and Dr Dagou Zeze for their support.

I'd also like to acknowledge the contributions of Mr Leon Bowen and Dr Budhika Mendis for their support from the Physics department, namely the use of and advice regarding FIB, EDX and TEM analysis, and Dr Richard Thompson in Chemistry for RBS analysis, as well as Dr David Scurr at Nottingham University for his help with ToFSIMS analysis and understanding. Thank you to Dr Mark Rosamond for his help with both FIB preparation and the phase shift lithography processing as well as his support and advice during my PhD. I would also like to thank Dr Chris Pearson for his help with AFM analysis during the early stages of my PhD work and Mr John Gibson for his support.

My appreciation is also extended to my colleagues and friends within the department. Firstly, Alice Delcourt-Lançon for acting as my mentor in the early days and my friend thereafter. To Kieran Massey for his help and enthusiasm regarding the cryostat, for our numerous chats about LaTeX coding and conduction mechanisms. To the members of our group: Fred Hamlin, Ben Lyons, Alison Fisher, Paul Farrar, Carlo Hill, Matty Jones, Richard Stone and Samantha Shenton and Rachael Daunton.

Additionally I'd like to thank my family and friends for their support: My mam and Rob for their patience, love and understanding, as well as my dad, my grandparents and the rest of my family.

Dedicated to

Sharon Dodd

my mam

Thank you for always being there for the challenging times as well as the great ones

I love you

xxx

Publications

- L.E. Dodd, A.J. Gallant and D. Wood, "Optimizing MOM Diode Performance via the Oxidation Technique", *Proc. IEEE Sensors Conference*, pp. 176-179, 2011. DOI: 10.1109/ICSENS.2011.6127347.

- L.E. Dodd, A.J. Gallant and D. Wood, "Ti-TiOx-Pt Metal-Oxide-Metal Diodes Fabricated via a Simple Oxidation Technique". *Proc. Material Research Society Meeting*, vol. 1415, pp 41-46, November 2011. DOI: 10.1557/opl.2012.72.

- L.E. Dodd, A.J. Gallant and D. Wood, "Controlled reactive ion etching and plasma regrowth of titanium oxides of known thickness for production of metal-oxide-metal (MOM) diodes". *IET Micro and Nano Letters*, vol. 8, pp. 476 478, August 2013, DOI: 10.1049/mnl.2013.0177.

Contribution to Other Publications

- D. Wood, M. Chamberlain, A. Baragwanath, L.E. Dodd, C. Hill and A.J. Gallant, "Micromachined Devices for Use in Terahertz Applications". *Advances in Science and Technology 81 - Next Generation Micro/Nano Systems*, vol. 81, pp. 20-27, 2013,
  DOI: 10.4028/www.scientific.net/AST.81.20

Conferences

- *"Optimizing MOM Diode Performance via the Oxidation Technique"*, IEEE Sensors Conference, Limerick, Ireland, 28-31 October 2011 (oral presentation)
- *"Ti-TiOx-Pt Metal-Oxide-Metal Diodes Fabricated via a Simple Oxidation Technique"*, Materials Research Society (MRS) Fall Conference, Boston, MA, USA 2011 (oral presentation)
- *"Production of sub-micron metal-oxide-metal diodes using two novel techniques"*, International Conferences on Modern Materials and Technologies (CIMTEC), Montecatini Terme, Italy 2012 (poster presentation)
- *"Failure Mechanisms in Metal-Oxide-Metal (MOM) Diodes"*, Electronic Materials Conference (EMC), South Bend, IL, USA 2013 (oral presentation)
- *"Production of Metal-Oxide-Metal (MOM) Diodes Using Phase Shift Lithography"*, Electronic Materials Conference (EMC), South Bend, IL, USA 2013 (oral presentation)

Contribution to Other Conferences

- David Wood et al., *"Micromachined Devices for Use in Terahertz Applications"*, International Conferences on Modern Materials and Technologies (CIMTEC), Montecatini Terme, Italy 2012 (oral presentation)
- Carlo Hill et al., *"Zero Temperature Coefficient of Resistivity in Nichrome"*, Micromechanics and Microsystems Europe (MME), Esroo, Finland 2013 (poster presentation)

Contents

Nomenclature

Abbreviations

μTPV	Microthermophotovoltaic
AC	Alternating Current
ALD	Atomic Layer Deposition
CC	Curvature Coefficient
CC_{ZB}	Zero Bias Curvature Coefficient
DC	Direct Current
$EBIC$	Electron Beam Induced Current
EDX	Energy-Dispersive X-Ray Spectroscopy
$GPIB$	General Purpose Interface Bus
GSG	Ground Signal Ground
$IMPATT$	Impact Avalanche Transit Time
IR	Infrared Radiation
MST	MicroSystems Technology
MOM	Metal Oxide Metal
NIL	Nano-Imprint Lithography
$PDMS$	Polydimethylsiloxane
$R2R$	Roll to Roll
RF	Radio Frequency
SMU	Source and Measurement Unit
SSD	Self-Switching Diode
TEM	Transmission Electron Microscopy

$ToFSIMS$	Time of Flight Mass Spectrometry	
USB	Universal Serial Bus	
UV	Ultra-Violet	
VNA	Vector Network Analyser	

Symbols

α	Distance Between Trap Sites	m
β_v	Voltage Responsivity	$\mathrm{V\,W^{-1}}$
Δf	Bandwidth	Hz
ϵ	Thermal Emissivity	
η_A	Rectenna Efficiency	
η_a	Efficiency of Coupling Radiation to Antennas	
η_{CA}	Curzon-Ahlborn Efficiency	
η_C	Carnot Efficiency	
η_c	Efficiency of Coupling Antenna Modes to Diode Modes	
η_j	Efficiency of Tunnelling Junction	
η_s	Efficiency of Propagating the Energy to the Diode	
λ	Wavelength	m
λ_{th}	Thermal Conductivity	$\mathrm{Wm^{-1}K^{-1}}$
ϕ_m	Barrier Height Between Two Sites	eV
ϕ_{bn}	Barrier Height	V
ρ	Electrical Resistivity	$\Omega\,\mathrm{m}$
σ	Stefan-Boltzmann Constant	$\mathrm{W/(m^2\ K^4)}$
τ_0	Time Constant	s
τ_c	Trap Capture Time	s
τ_e	Trap Emission Time	s
ε_0	Permittivity of Free Space	$\mathrm{Fm^{-1}}$
ε_r	Relative Permittivity	
A	Surface Area	$\mathrm{m^2}$

$A*$	Effective Richardson Constant	$\mathrm{A\,m^{-2}\,K^{-2}}$
A_{ant}	Antenna Capture Area	$\mathrm{m^2}$
C_D	Diode Capacitance	F
c	Speed of Light	$\mathrm{m\,s^{-1}}$
d	Oxide Thickness	m
D^*	Detectivity	$\mathrm{mHz^{\frac{1}{2}}W^{-1}}$
E	Energy	J
e	Electron Charge	C
f_c	Cut-off Frequency	Hz
$\hbar$	Reduced Planck's Constant	Js
h	Planck's Constant	Js
I_{DC}	DC Current Output from Diode	A
J	Current Density	$\mathrm{Acm^{-2}}$
k	Boltsmann's Constant	$\mathrm{JK^{-1}}$
m^*	Free Electron Mass	kg
m_m	Effective Electron Mass in Metal	kg
m_{ox}	Effective Electron Mass in Oxide	kg
n	Ideality Factor	
n^*	Electron Density at Trap Sites	$\mathrm{m^{-3}}$
N_c	Density of States in Oxide Layer Conduction Band	$\mathrm{m^{-3}}$
N_T	Trap Concentration	$\mathrm{m^{-3}}$
N_v	Diode Non-Linearity	$\mathrm{A\,V^{-2}}$
NEP	Noise Equivalent Power	W
P_i	Incident Power	W
P_L	Power In at Diode	W
P_{dBm}	Power	dB
P_{IN}	Power In to Rectenna from Hot Reservoir	W
P_{mW}	Power	mW

P_{OUT}	Power Out from Rectenna to Hot Reservoir	W
P_{th}	Thermal Power Emitted from the Source	W
R_A	Antenna Resistance	Ω
R_v	Diode Resistance	Ω
S	Radiated Flux	Wm^{-2}
S_λ	Spectral Emittance	$\mathrm{Wm^{-2}sr^{-1}\mu m^{-1}}$
S_b	Seebeck Coefficient	VK^{-1}
T	Temperature	K
T_0	Ambient Temperature	K
T_C	Cold Temperature Reservoir	K
T_H	Hot Temperature Reservoir	K
V	Applied Voltage	V
V_n	Noise Voltage across Diode	$\mathrm{V\,Hz}^{-1}$
V_o	Voltage Output	V
V_{DC}	DC Voltage Output from Diode	V

Chapter 1

Introduction

This thesis presents the process development and analysis of metal oxide metal (MOM) diodes, with the aim of rectifying high frequency signals. These diodes are to be coupled with antennas, forming a 'rectenna' device. However, the devices have a wider range of possible applications, including IR camera devices, the detection of terahertz radiation and recovery of heat energy in the automotive and other industries. There are a number of other technologies, which exist to recover useful energy from heat, including thermoelectric devices and microthermophotovoltaics and it is hoped that the devices presented here could ultimately rival these. It is worth noting, however, that all devices are limited by Carnot efficiency.

Although the rectenna device consists of both an antenna and diode, the diode is the focus of this thesis as, once designed, the antennas are comparatively straightforward to make using standard lithographic processes. By contrast, the diode has three main fabrication concerns: the diode consists of two metals separated by an oxide layer which must be thin and uniform, the metals must be different to improve asymmetry of the diode characteristics, and the diode must be sufficiently small that high frequency rectification can occur. Through the fabrication and both electrical and physical analysis of devices, these critical factors are considered and diodes are produced with competitive results.

1.1 Thesis Objective and Organisation

Chapter 1

Chapter 1 introduces the thesis, outlines the motivation and validity of the research and also outlines each thesis chapter.

Chapter 2

Chapter 2 discusses infrared radiation and the need to recover this energy. Black-body emitter theory is discussed, as well as potential applications for energy recovery and/or detection, including IR camera and terahertz detection, with a focus on the automotive industry. Car exhaust pipes are highlighted as potential sources of infrared radiation, and the amount of energy available from an exhaust is discussed.

Chapter 3

This chapter discusses existing technologies which are used to recover heat. Thermoelectric devices in the automotive industry are discussed, as well as microthermophotovoltaic (μTPV) devices and rectenna devices. Various antenna designs are also discussed, as well as the Carnot efficiency associated with such devices, which will limit their efficiencies.

Chapter 4

Chapter 4 discusses the conduction mechanisms found in many types of diodes and also discusses which existing diode technologies could be useful. The aim is to determine which conduction mechanisms would be useful, which are currently designed into existing high frequency diodes and therefore which should be designed into fabricated diodes. Each of the conduction mechanisms varies in suitability for high frequency rectification and so the aim is to design and produce diode structures which will take these mechanisms into account.

Chapter 5

Chapter 5 discusses the main fabrication and analysis techniques used, including standard photolithography, phase shift lithography, metallisation, I-V analysis, interfacing with equipment, AFM, SEM, TEM, and ToFSIMS, and discusses their importance in analysing the devices fabricated.

Chapter 6

Chapter 6 details the device fabrication process of furnace oxidised diodes with dimensions down to 10 x 10 μm and the fundamental findings from the analysis of these diodes, including their I-V characteristics, curvature coefficients and current ratios. Both physical and electrical analysis is included: cryostat testing and conduction mechanism analysis, AC testing, DC testing as well as TEM, AFM, RBS and ToFSIMs. The failure mechanisms are also discussed.

Chapter 7

Chapter 7 discusses the oxide fabrication process development and subsequent improvements to the diode characteristics. Reduced size diodes were also produced and additional fabrication steps added to further improve the fabrication process and the subsequent electrical results from this devices.

Chapter 8

Chapter 8 concludes the findings of the thesis and discusses potential further work in this field of research, including device improvements.

Chapter 2

Infrared Radiation

2.1 Introduction

One of the most common forms of wasted energy is radiated heat, which is usually in the infrared (IR) part of the spectrum. Recovering such energy and converting it into a useful form could have a dramatic impact on global energy issues. In this chapter, blackbody emitter theory will be discussed to further detail the energy that is available, the frequency ranges and associated energy quantities which could be recovered or detected. Several potential applications for the detection/recovery of infrared radiation are also discussed, including infrared cameras, the detection of terahertz radiation and energy recovery in the automotive industry, thus showing that there is a demand for the ability to detect infrared radiation.

2.1.1 Blackbody Emitters

In classical physics, namely Maxwell's theory, light is a wave consisting of both electric and magnetic fields, with a smooth energy distribution. Although electromagnetic waves exhibit numerous characteristics of waves, they can also exhibit properties of particles, known as photons. This wave-particle duality is evident in the study of blackbody radiation.

The radiation from a blackbody source is emitted with a specific spectrum, which varies with the temperature of the object, with hotter objects having higher intensities at lower wavelengths, as seen in Figure 2.1. This was contrary to what

was expected, and was solved by a proposal by Max Planck, who suggested that atoms can only absorb or emit radiation in specific amounts, therefore energy is quantised.

In order to investigate how much energy would be available from a heat source at a given temperature, the blackbody emitter is discussed as an ideal case of a device emitting radiation at a given temperature. A blackbody has the following properties [1]:

- All incident radiation is absorbed, irrespective of direction or wavelength
- No surface can emit more energy than a blackbody for a given temperature and wavelength
- Radiation emitted is independent of direction, i.e. a blackbody is a diffuse emitter

Fundamentally, there is a direct relationship between absorption and emissivity, which can be used to help find the desired materials:

"A good absorber is a good emitter; and a poor absorber is a poor emitter" [2]

Furthermore, Kirchhoff's Law states that the spectral emissivity is equal to the spectral absorption under the same conditions. Planck's Law, as seen in Equation 2.1, can be used to determine the spectral emittance of a desired material.

$$S_\lambda = \frac{2\pi c^2 h}{\lambda^5} \frac{1}{e^{\frac{hc}{kT\lambda}} - 1} \tag{2.1}$$

where

S_λ = Spectral emittance [$\mathrm{Wm^{-2}sr^{-1}\mu m^{-1}}$]
c = Speed of light = $3 \times 10^8\,\mathrm{m\,s^{-1}}$
h = Planck's constant = $6.63 \times 10^{-34}\,\mathrm{Js}$
λ = Wavelength [m]
k = Boltzmann's constant = $1.38 \times 10^{-23}\,\mathrm{JK^{-1}}$

It can also be demonstrated that the spectral emittance of a blackbody has a maximum at a wavelength given by Wien's Law in Equation 2.2 [2]. As can be seen, the wavelength of maximum spectral emittance is inversely proportional to the temperature:

$$\lambda_{max} = \frac{hc}{4.9651kT} = \frac{\beta}{T} \tag{2.2}$$

Where:

$$\beta = \frac{hc}{4.9651k} = 0.0029\,\mathrm{m\,K}$$

It can also be shown that the total flux is proportional to the fourth power of the temperature, as seen in Equations 2.3 and 2.4 [2]:

$$S = \sigma(T^4 - T_0^4) \tag{2.3}$$

Where:

T = temperature of the material in question [K]

T_0 is the ambient temperature [K]

$\sigma = \frac{2\pi^5 k^4}{12c^2h^3} = 5.67 \times 10^{-8}\,\mathrm{W/m^2K^4}$ = Stefan-Boltzmann Constant

S = radiated flux or power per unit area

$$P_{th} = A\epsilon\sigma(T^4 - T_0^4) \tag{2.4}$$

Where:

A = surface area [$\mathrm{m^2}$]

ϵ = thermal emissivity

P_{th} = thermal power emitted from the body [W]

The thermal emissivity (ϵ) is essentially an efficiency (0 - 1) to translate the ideal expected power ($\epsilon = 1$) into what is measured from real surfaces ($\epsilon < 1$). The graph seen in Figure 2.1 is a visual representation of Planck's Law, with the derivative of this showing the maximum wavelength point for a given temperature, which can be calculated using Wien's Law. The integral of these curves can be used to determine the total flux of the system, which is also given by the Stefan-Boltzmann Law.

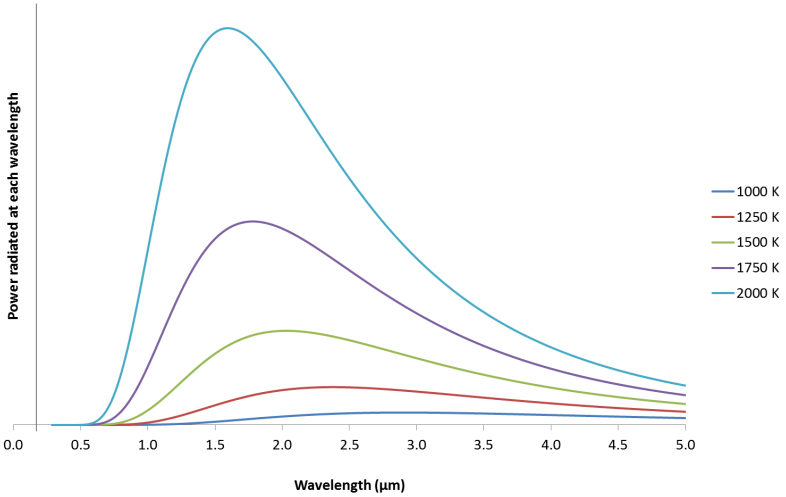

Figure 2.1 – *Blackbody characteristics for different temperatures*

As can be seen from Equation 2.5, hotter objects emit more energy than colder objects (per unit area). The amount of energy radiated is proportional to the temperature of the object to the fourth power. Furthermore, the hotter the object, the shorter the wavelength of the emitted energy.

$$E = kT = \frac{hc}{\lambda} \tag{2.5}$$

2.2 Potential Applications

2.2.1 IR Cameras

Infrared cameras are used to provide an image in the same way a standard camera does, only in the infrared rather than the visible spectrum. Infrared, or thermographic, cameras can be split into two main categories: cooled and uncooled. Cooled detectors are usually cryogenically cooled to 80 to 100 K and are under vacuum. The cooling is necessary to reduce the amount of radiation emitted by the camera itself to prevent it from affecting the imaging. These cooled cameras operate using various photodetectors, including semiconductor based devices.

Uncooled devices, by comparison, use sensors which operate at room temperature and therefore they usually rely on a change of resistance, current or voltage which

can be compared to an ambient reference temperature to provide a difference. These devices are much cheaper and smaller than their cooled counterparts but they provide less accurate results. They are usually manufactured using pyroelectric materials or microbolometers. Each of these devices would act as a single pixel, multiples of which can then be combined to create an image. The advantage of finding a sensor which could be used in an uncooled thermographic camera with improved pixel density or improved features such as range or frame rate for example would be desirable.

2.2.2 Terahertz Detection

Terahertz radiation is described as being in the 10^{12} Hz range, between the microwave and infrared regions of the electromagnetic spectrum. Terahertz radiation can penetrate certain materials such as plastics, paper and clothing and could therefore be used in security and threat detection. Furthermore, due to its low photon energy (approximately 1 million times less than x-rays), terahertz radiation is non-ionising and is therefore not thought to be dangerous to humans. As a result, terahertz radiation is also being trialled for medical applications, to detect cancers, for DNA analysis and for scanning injuries which are bandaged without disturbing the area of interest.

Materials also exhibit characteristic resonant responses, known as fingerprints, in the terahertz region, allowing real time differentiation between different materials and chemicals. Therefore terahertz radiation detectors would be very useful for gathering these results and interpreting them [3].

2.2.3 Automotive Industry

Due to the dependence on fossil fuels globally, as well as an awareness of their finite nature, there is currently a desire to try to reduce the use of these through either finding an alternating source of fuel or by increasing the efficiency of existing devices. One of the main consumers of fossil fuels is the automotive sector.

As can be seen in Figure 2.2, typical internal combustion petrol fuelled engines

use 25 to 30 % of the energy from the petrol to move the vehicle, with 40 to 45 % of the energy being dissipated as heat through exhaust gases [4]. If this heat energy could be harnessed in some way, the recovered energy could be used to power electrical items within the car, such as the audio equipment and perhaps the vehicle lighting. Even more efficient systems could alleviate the work load on the alternator and eventually replace the alternator altogether.

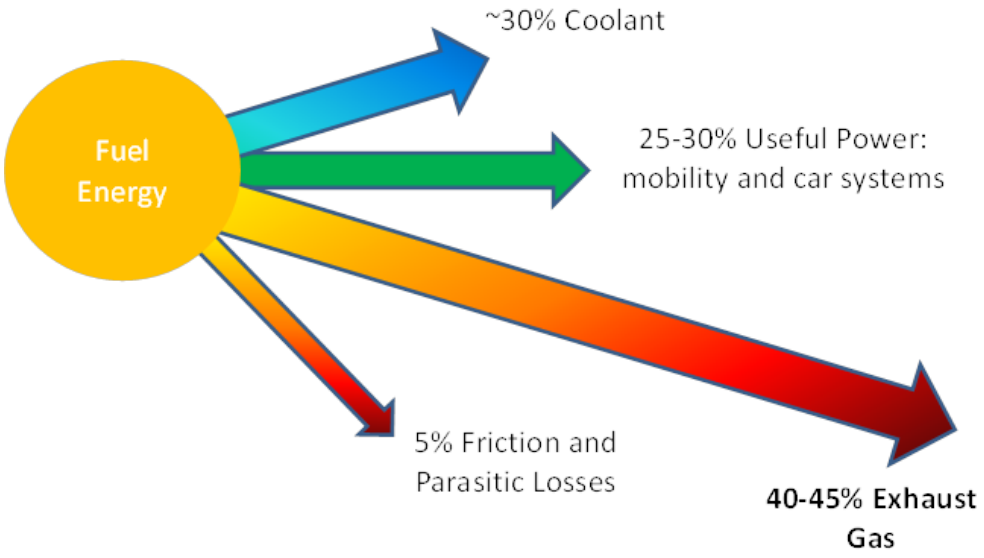

Figure 2.2 – *Representation of approximate fuel percentages within a vehicle*

Vehicle electrical demands [4]:

- 300 to 1500 W needed during typical consumer driving
- Additional 200 to 800 W needed if coolant pump is converted from mechanical to electric drive
- Additional 3000 to 5000 W needed to power air conditioning (again if converted from mechanical to electrical operation)

The above power ratings act as important step levels for the functionality of any device design with the aim of replacing one of these systems.

The question is how can the waste energy from combustion be successfully recovered? There are various methods, which will be discussed in Chapter 3.

Furthermore there are numerous additional vehicle conditions which must be taken into account:

- Limited space
- Shock and vibration issues
- Ambient air temperature from -40 to $52\,^{\circ}\mathrm{C}$
- Thermal cycling
- Long life required as cars can run for 15 years or longer

Automotive efficiency is a contemporary issue which is attracting a great deal of attention globally, with numerous different methods of energy recovery being tested and implemented in vehicles. Of these, regenerative braking is the most commercially advanced. It involves recovering energy from the vehicle during braking.

BMW have also designed an alternative system, called "Brake Energy Regeneration"; whereas in conventional cars the alternator is permanently driven by a belt connected to the engine, BMW's Brake Energy Regeneration system only activates the alternator when not accelerating, converting the previously wasted kinetic energy into electricity which is stored into the battery. This also means that when accelerating, the alternator is detached thus providing more engine power to the drive wheels. It is reported this technology improves efficiency by $3\,\%$ [5].

Many companies have also designed an auto start-stop system which, while saving energy when the vehicle has stopped, will not provide a large saving as it is only beneficial when the vehicle is stationary. Regenerative braking has a similar issue, only working when the vehicle is decelerating. There is currently no major device which recovers energy from a vehicle during standard, continuous motion of the vehicle. Replacing lighting with LED equivalents can be used to reduce the amount of energy dissipated. LED lighting has been shown to be able to save over two thirds of the energy used by incandescent lighting, which would equate to 1.4 billion gallons of fuel per year if every vehicle in the USA used all LED lighting.

This equates to a saving of 0.8 %, given that the annual fuel consumption of the USA in 2006 was 174.9 billion gallons [6].

Another concept is vehicles that are fuelled by alternative sources, such as hydrogen and electricity. Prototype hydrogen cars are currently available and electric cars are available for consumer purchase. However, there is a comparative lack of infrastructure in place to accommodate a large percentage of owners nationwide or globally. Hydrogen vehicles also have the negative consumer perception of being dangerous.

Internal combustion engine vehicles each have an exhaust pipe, which can reach temperatures of up to 1000 °C in extreme circumstances [4]. The exhaust pipe outer surface does then act as an emitter of heat, and provides an ideal opportunity for suitable devices to recover some of this energy.

Calculating the Amount of Energy Available

In order to verify the amount of energy available from an exhaust pipe, two methods of estimation were used and their results compared. The first approach is using engine power graphs from vehicle manufacturers to determine the output power at different engine speeds. This power can then be split into useful and waste energy, based on suggested numbers in Figure 2.2.

An alternative approach is the use of the Stefan-Boltzmann equation to calculate the approximate power density of the exhaust pipe based on the temperature profiles recorded using a FLIR A40 ThermoVision camera.

Power Calculations based on Manufacturer Estimations

Figure 2.2 gives a guide on how the chemical energy in petrol is dissipated as a result of combustion. Of the exhaust gas heat, 10 to 20 % is dissipated from the pipe surface, with the remaining heat being expelled as hot exhaust gas [7]. These values are, however, very dependent on a number of factors, including the design of the exhaust pipe system as well as the driving conditions.

Based on these estimations, the power available at different engine speeds can be calculated from the engine speed profile of the desired vehicle. The engine profile

graph of the Jaguar XJ from manufacturer's figures in [8] can be seen in Figure 2.3.

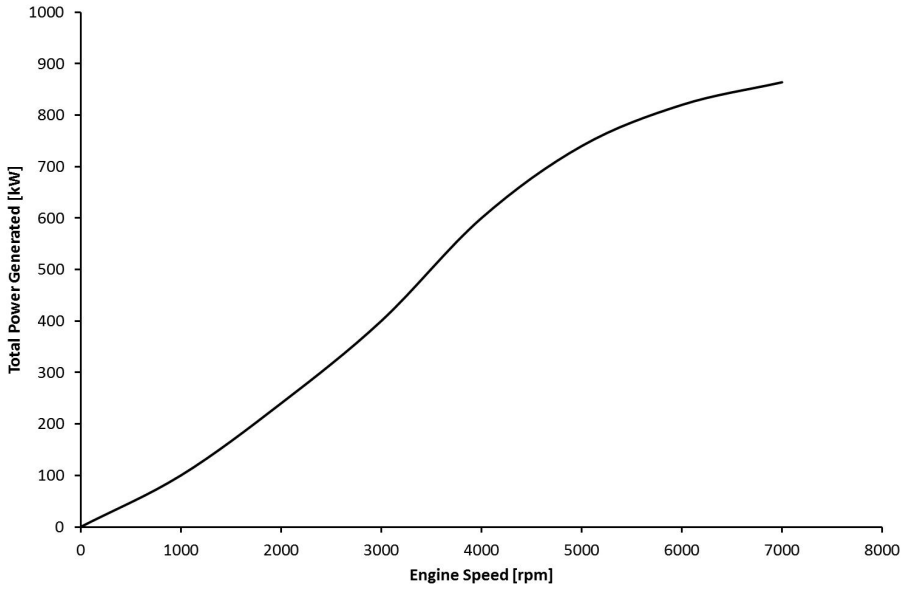

Figure 2.3 *– Total power generated from a Jaguar engine*

The y-axis shows the total power output, assuming an engine efficiency of 25 %. The rated power, i.e. that available at the driving wheel is 216 kW at 6100 rpm, therefore the total power is 864 kW.

Through a combination of these engine power graphs and the estimated engine efficiencies, the power available from an exhaust can be calculated at different engine speeds. Tables 2.1 and 2.2 show the results of these calculations. Table 2.1 refers to the Toyota Yaris for different engine speeds, while Table 2.2 refers to the Jaguar engine speeds. As can be seen, the Jaguar can reach much higher engine speeds than the Toyota Yaris, due to the Jaguar having a petrol engine and the Yaris using a diesel one. This further increases the difference in exhaust pipe power between the two models of vehicle.

Table 2.1 *– Power available from a Yaris engine given different engine speeds and efficiencies*

Rpm	Total Power Generated (kW) (40 % Efficient Engine)	Power at Exhaust (40 - 45 %) (kW)	Power at Exhaust Surface (10 - 20 %) (kW)
1000	47	19 - 21	2 - 4
2000	95	38 - 43	4 - 9
3000	**142**	**57 - 64**	**6 - 13**
3800	180	72 - 81	7 - 16

As can be seen, the estimation as to how much of the overall engine power actually dissipates through the exhaust pipe also has a large effect on the available power.

Table 2.2 *– Power available from a Jaguar engine given different engine speeds and efficiencies*

Rpm	Total Power Generated (kW) (25 % Efficient Engine)	Power at Exhaust (40 - 45 %) (kW)	Power at Exhaust Surface (10 - 20 %) (kW)
1000	100	40 - 45	4 - 9
2000	240	96 - 108	10 - 22
3000	**400**	**160 - 180**	**16 - 36**
4000	600	240 - 270	24 - 54
5000	740	296 - 333	30 - 67
6100	864	346 - 389	35 - 78

The total power generated by the Jaguar was calculated based on a specified

mechanical power output of 216 kW and an engine efficiency of 25 %. The Toyota Yaris, having a diesel engine, has a higher engine efficiency believed to be in the region of 40 % [9]. The stated mechanical power output of the Yaris is 66 kW [10]. Assuming an efficiency of 40 %, in total the engine generates 165 kW at 3800 rpm. Therefore, for other values of engine speed, a linear approximation has been used, resulting in the values seen in Table 2.1.

These two engines represent two very different cars, which approach opposing ends of the range of cars typically driven. The Yaris is very efficient and only has a small engine, whereas the petrol Jaguar is much less efficient, has a much larger engine and therefore loses more energy through the exhaust pipe. The majority of cars would fall in the range between these two extreme examples, which is why these particular models were chosen, in order to find the limits of the range associated with power available.

Power Calculations based on Exhaust Temperature Profiles

Having estimated the amount of power available from manufacturer values, an alternative method of estimating the amount of power available was through the use of temperature profile results. Given a known temperature and an ambient temperature, the radiated heat flux per unit area can be calculated by Equation 2.3, for a perfect blackbody emitter. Table 2.3 shows the relationships between the temperature, wavelength and radiated flux. The wavelength in this table is defined by Wien's Law, seen in Equation 2.2.

As can be seen, a power in the region of kilowatts is available per unit area, even at temperatures which are within the range of that of an exhaust pipe. Using the above information and the temperature profile of exhaust pipes, the total power available from an exhaust pipe was calculated. The IR camera was used to provide a temperature profile of the exhaust system on a car. This temperature profile was then used to help determine the temperature range that the emitter will operate in, which was initially believed to be from ambient to 600 °C, with temperatures of 1000 °C being achieved in extreme circumstances [4].

There are many factors which affect the exhaust temperature, including ambient

Table 2.3 *– Relationship between temperature, wavelength, frequency and radiated flux*

Temperature T (°C)	Wavelength $\lambda = \frac{\beta}{T}$ (μm)	Frequency $f = \frac{c}{\lambda}$ (THz)	Radiated Flux $S = \sigma(T^4 - T_0^4)$ (kWm^{-2})
50	8.98	33.41	0.19
100	7.77	38.59	0.67
150	6.86	43.76	1.39
200	6.13	48.93	2.41
250	5.54	54.10	3.82
300	5.06	59.28	5.69
350	4.65	64.45	8.12
400	4.31	69.62	11.21
450	4.01	74.79	15.07
500	3.75	79.97	19.82
550	3.52	85.14	25.59
600	3.32	90.31	32.51

temperature, how long the car has been running and at what speeds, as well as the effects of ambient cooling. Therefore, in order to gain an understanding of the extent to which this temperature profile can vary, numerous recordings were taken.

Access to the underside of the vehicle was achieved with the support of Stagecoach allowing the use of their pits. The imaging took place after the vehicles had been driven with different styles. The initial experiment involved the effects of a journey at low speeds on the temperature of the exhaust. An additional experiment took place after the vehicle has been operating with the engine at 3000 rpm. Further experimentation took place with both petrol and diesel vehicles to compare their temperature profiles. The video functionality of the camera captured the length of time taken for the exhaust to rise in temperature, with the vehicle idling and then running at high revolutions for a designated period of time.

As can be seen from Figure 2.4, the maximum temperature of the exhaust from

the diesel engine is 135 °C, which may seem low initially. This would mean that there is much less energy available for recovery. However, this is because more of the energy created in combustion is available to do mechanical work.

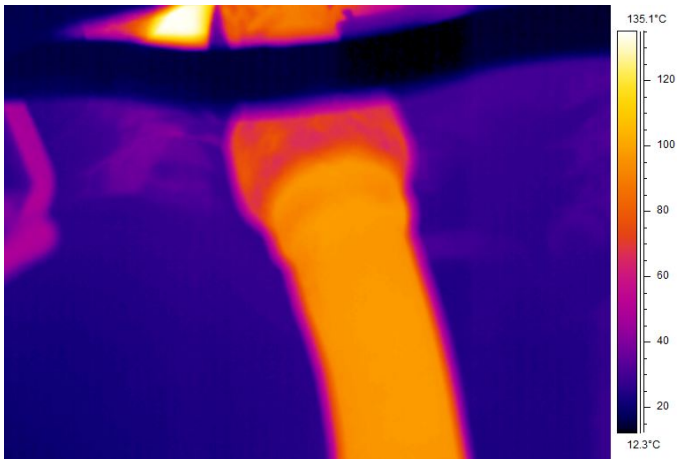

Figure 2.4 *– The exhaust pipe of a 1.4 l diesel Toyota Yaris at 3000 rpm (infrared)*

As can be seen from Figure 2.5, the equivalent point on a petrol exhaust pipe has a much higher temperature, in excess of 300 °C. It should, however, be noted that the engine of this petrol vehicle is much larger. A bigger engine provides more power as previously discussed, which in turn provides more waste heat, resulting in a higher exhaust temperature. The temperature is in the range of ambient to 330 °C.

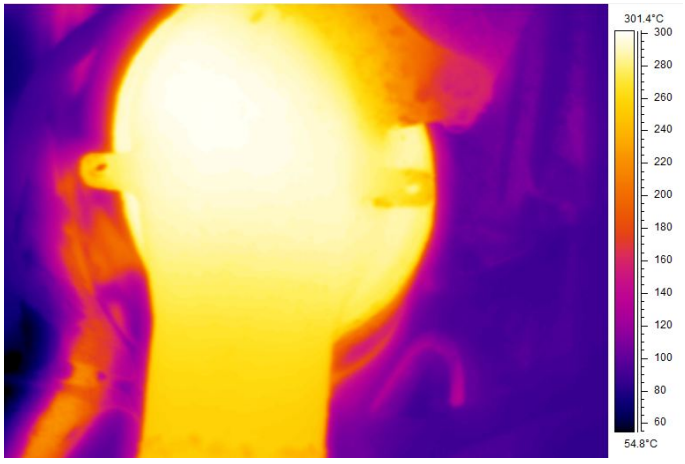

Figure 2.5 *– The exhaust pipe of a 4 l petrol Jaguar at 3000 rpm (infrared)*

As expected, the temperature decreases further down the exhaust away from

the engine, which means any energy scavenging which takes place will have to be optimised to accommodate this profile. Figure 2.6 shows the temperature profile of a Jaguar exhaust pipe, superimposed on a photograph of the underside of the car with the main part of the exhaust being 225 to 300 °C, with the cooler 100 °C region being a silencer.

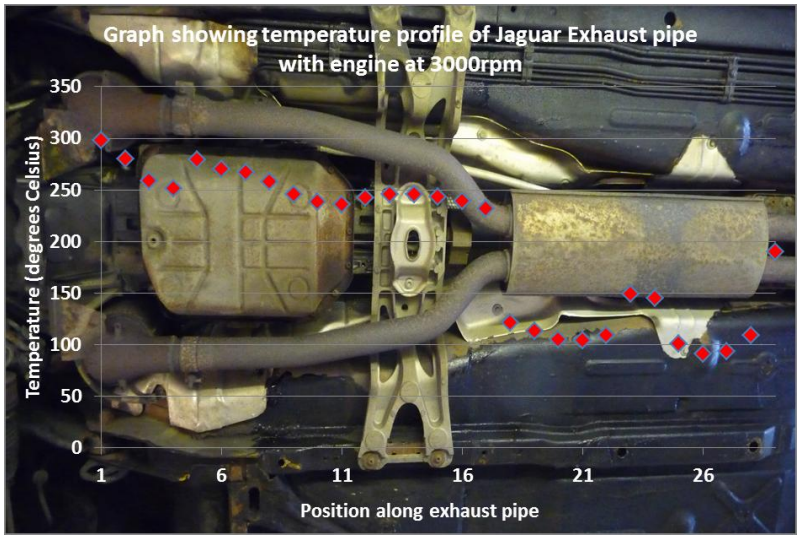

Figure 2.6 – *The exhaust pipe of a 4 l petrol Jaguar at 3000 rpm*

The sudden drop in temperature at the silencer is due to a difference in emissivity compared to the exhaust pipe, which is evident mid-way along the silencer, where a dark region on the surface causes a sudden increase in temperature. This is due to the thermal camera software assuming an emissivity of 1 in order to calculate the absolute temperature value. Therefore, the silencer region of Figure 2.6, while interesting, will not be included in future temperature profile analysis of the exhaust.

The powers calculated in Table 2.4 are based on the estimated exhaust pipe surface areas and a temperature of 100 to 150 °C for the Toyota Yaris and 250 to 330 °C for the Jaguar. The temperatures are based on temperature profiles, which were measured at Stagecoach Walkergate.

The powers in Table 2.4 were calculated using an estimation for the surface area of each exhaust pipe. As can be seen, the Jaguar exhaust has a significantly larger surface area; this car is much larger than the Yaris and has a double exhaust design. This, combined with the lower exhaust pipe temperatures on the Yaris, results in a large difference in available power. The temperature ranges recorded by the thermal

Table 2.4 *– Relationship between temperature, wavelength, frequency and radiated flux*

Car	Fuel Type	Engine Size ($litres$)	Total Surface Area (m^2)	Exhaust Temperature °C	Power (kW)
Toyota Yaris T3 D-4D (2003)	Diesel	1.4	0.7	100 - 150	0.5 - 1.0
Jaguar V8 Engine (1998)	Petrol	4.0	2.4	250 - 330	9.2 - 17.0

camera images have been extrapolated across the entire surface area to provide this estimation, as there would be hotter regions at one extreme of the exhaust and colder regions at the other.

It is also possible to calculate the wavelength of the radiation emitted from the exhaust pipe, given the temperatures stated above. Taking the two exhaust temperature profiles, and a range of 150 to 330 °C, Equation 2.2 can be used to calculate a wavelength range of 4.8 to 6.8 µm. This equates to a frequency range of approximately 44.1 to 62.5 THz.

Comparison Summary between Temperature and Power Estimations

A summary for the comparison between the estimated powers available from the Jaguar exhaust pipe at 3000 rpm can be seen in Table 2.5.

Table 2.5 *– Summary of available power from exhausts at* 3000 rpm

Calculation Method	Available Power (kW)
Temperature Profile 250 to 300 °C	**9 - 17**
Engine Efficiency Calculations	**16 - 36**

As can be seen from Table 2.5, two independent estimation methods have been

used to gain an appreciation of the amount of power available from a car exhaust pipe. Note Table 2.2 only gave figures for a 25 % efficient engine. Figure 2.2 shows that the efficiency of a petrol engine can be up to 30 %, which would reduce the lower limit in Table 2.2 at 3000 rpm from 16 to 13 kW. Both have concluded that there is a significant amount of power available, and furthermore the power ranges calculated overlap thus providing confidence in the calculations.

COMSOL Multiphysics Simulations

In order to further verify the findings of the amount of energy available from the exhaust pipe, COMSOL Multiphysics software has been used. COMSOL Multiphysics is a simulation tool which allows users to combine a number of different elements of physics, and to solve problems, which involve the bi-directional interaction of these physics elements. COMSOL was used to combine radiative heat transfer and fluid flow. This was achieved using two physics modules, which interact to provide one single, accurate solution. COMSOL also allows the user the choice between stationary and transient analysis.

The aim was to model a section of exhaust pipe and compare the surface parameters of the model exhaust pipe with the information found during both the temperature profiling experiments, and the power calculations. A transient analysis was also used to see how the exhaust pipe temperature varies in time, with different engine speeds.

The stationary analysis involved a section of pipe 0.28 m long, with a short section of pipe attached to the front, acting as a heat source in the same way the engine acts as a heat source to an actual exhaust. This length was chosen as it matches the length of sections of actual pieces of exhaust pipe obtaining during a visit to Calsonic Kansei, a local manufacturer of exhaust systems. Therefore, if further experiments were to take place with these pieces, the model could be used to verify these experimental results.

In this model the automatic mesh contained too many nodes, and hence too many degrees of freedom, to solve successfully. As a result, a swept mesh was used down the length of the exhaust pipe section. This involved providing a mesh on one

end of the pipe and then repeating this mesh pattern at defined intervals down the pipe. This, combined with manual selection of an appropriate solver, allowed the model to be solved successfully.

Results

The temperature profile of the exhaust pipe can be seen in Figure 2.7, which also shows the air flow around the pipe. Inside the pipe there is an air flow equivalent to the air flow through a Jaguar exhaust pipe at 3000 rpm, the same engine speed as the previous experiments. The air flow on the outside of the model is at a speed equivalent to the car travelling at 30 mph. As can be seen, the temperature inside the pipe is at a much higher temperature (1280 K) and the temperature gradient is high across the thickness of the pipe, which is being cooled by the external air.

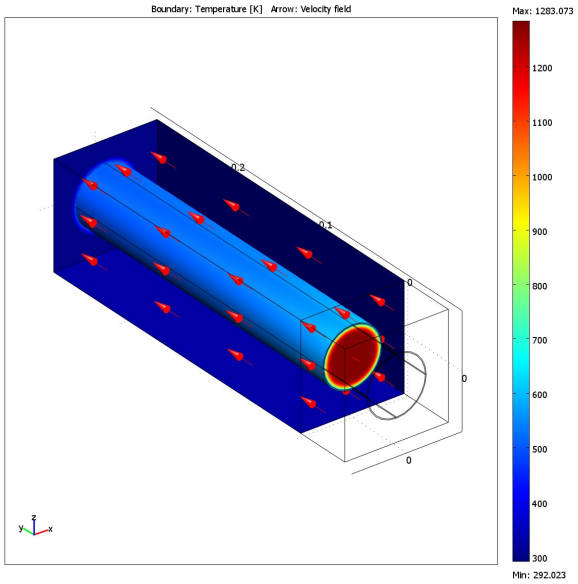

Figure 2.7 *– COMSOL model of temperature and velocity field of exhaust pipe with pre-extension heating unit visible (outlined)*

The surface temperature of the pipe varies between 495 K and 550 K, which can be seen in Figure 2.8, showing how the temperature varies down the 0.28 m length of the pipe section. This agrees with the previous experimentation on the Jaguar exhaust, which can also be seen in Figure 2.8. Due to computational resource limitations, only a 0.2 m section of pipe could be analysed. However, as can be seen the COMSOL model shows a close correlation to the experimental results, with the

main cause of variation being caused by the assumption in the COMSOL of a surface emissivity of 1, whereas the emissivity will vary with position on the exhaust pipe caused by surface defects.

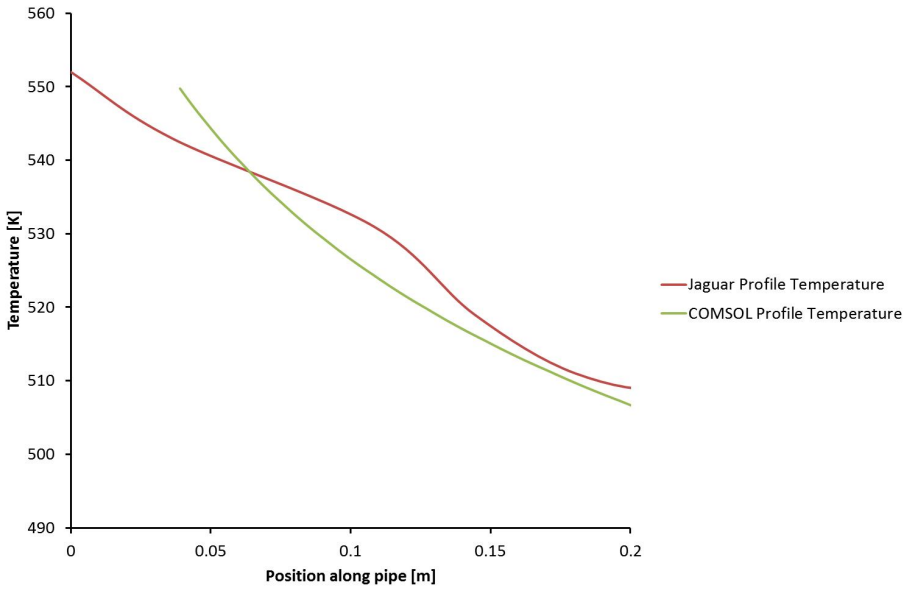

Figure 2.8 – *Temperature plot of COMSOL model and previous Jaguar temperature profile*

2.3 Infrared Radiation Conclusions

As has been discussed in this chapter, there is a great need for an energy recovery device which can reduce the amount of energy that is currently dissipated as infrared radiation in a multitude of applications. In the automotive industry, the amount of energy available has been quantitatively described and the significance discussed. Given two separate methods of estimation, the ranges of instantaneous power available from a car exhaust pipe overlap thus confirming the validity of the estimations. Furthermore the powers discussed are in the kilowatt range and therefore could have a significant impact on vehicle efficiency if recovered. Other applications, including the use of infrared laser detectors and infrared cameras have been discussed and their importance emphasised.

Chapter 3

Methods of Heat Energy Recovery

3.1 Introduction

Having demonstrated the need for infrared radiation detection and recovery devices in the previous chapter, this chapter discusses existing technologies with the ability to recover heat energy. Thermoelectric designs in the automotive industry are analysed as well as microthermophotovoltaic (μTPV) and rectenna devices. Various different antenna designs are also discussed for the rectenna devices and the Carnot efficiency, which would limit the returns from such devices, is discussed.

3.2 Thermoelectric Devices

A large amount of research has focussed on the use of thermoelectric devices, with exhaust pipe energy recovery systems currently being investigated using this technology. Thermoelectric effects involve the coupling between electrical and thermal voltages induced by an electric field and a temperature gradient, as seen in Figure 3.1 [11].

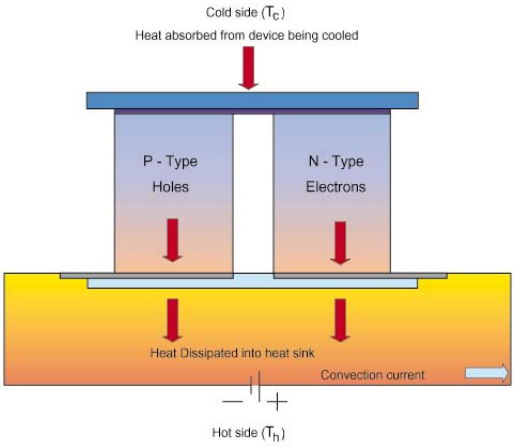

Figure 3.1 *– Diagram of thermoelectric effect (©InfoVision Technologies Inc.)*

As can be seen from Equation 3.1 [4], the maximum possible efficiency of thermoelectric devices relies heavily on a large temperature gradient.

$$\eta_{max} = \frac{T_{hot} - T_{cold}}{T_{hot}} \frac{\sqrt{1+ZT}-1}{\sqrt{1+ZT}+\frac{T_{cold}}{T_{hot}}} \tag{3.1}$$

Where:

$$ZT = (S_b^2 T)/\rho\lambda_{th} \tag{3.2}$$

S_b = Seebeck coefficient [VK^{-1}]

ρ = electrical resistivity [$\Omega\,\mathrm{m}$]

λ_{th} = thermal conductivity [$\mathrm{Wm}^{-1}\mathrm{K}^{-1}$]

ZT = thermoelectric figure of merit (typically $ZT < 3$)

The thermoelectric effect works well in outer space due the use of a nuclear fission reaction providing a hot surface and a contrasting surrounding temperature of near absolute zero, and so is used to power deep space probes.

Thermoelectric devices have a long life span, having been tested over time periods of 30 years. They can also be made to be highly reliable through networks of systems for added redundancies. The designed product has no noise, vibration or moving parts. Commercially, as with all of the methods suggested, the 'green image' can be used as a marketing tool in the automotive industry.

By contrast, although these devices work well in space, it is impossible to match

these results on Earth as there is much less of a temperature difference. In order to increase their effectiveness in the automotive industry, existing prototype vehicles have their own cooling system, which increases the design complexity and integration level within the car. The device itself must also form an in-line section of the exhaust pipe. This in turn further increases the complexity of the design and means that installing such a device into a car would be a labour intensive procedure. The hot contact on existing prototypes is also placed inside the exhaust pipe, exposing it to the corrosive gases present, so it must be designed to be resistant to chemical attacks. The disposal of thermoelectric materials at the end of the product's life could also be difficult.

One of the major materials used in the design of prototypes is tellurium, with each vehicle requiring 0.5 kg of tellurium for a thermoelectric module. Even if the global annual production of tellurium (approx. 1×10^5 kg pa [12]) was used for thermoelectric devices, only 0.25 % of new vehicle production in 2011 [13] would be accounted for [4].

This system is also relatively heavy (57 to 110 kg [14]), resulting in increased fuel consumption, which will partially offset the recovered energy.

3.3 Microthermophotovoltaics

Micro-Thermophotovoltaics (or μTPV) are an alternative form of energy recovery and consist of the following:

- A filter, which restricts the ranges of wavelength which are incident on the photovoltaic, is required if a blackbody emitter is used
- Photovoltaic cells

In the chosen application, the heat source will be the exhaust pipe. The emitter is required to provide the infrared radiation, which is then converted by the photovoltaic cells into a useful voltage.

The most significant work within this field has been the works of Yang et al. [15,16], which concentrate on using a μTPV on micro-heaters to act as an alternative

to batteries. The main issue with this work was heat dissipation, with the design having large fin arrays to prevent high temperatures damaging the photovoltaics. Figure 3.2 [17] shows a cross section of a hydrogen fuel cell surrounded by μTPV arrays.

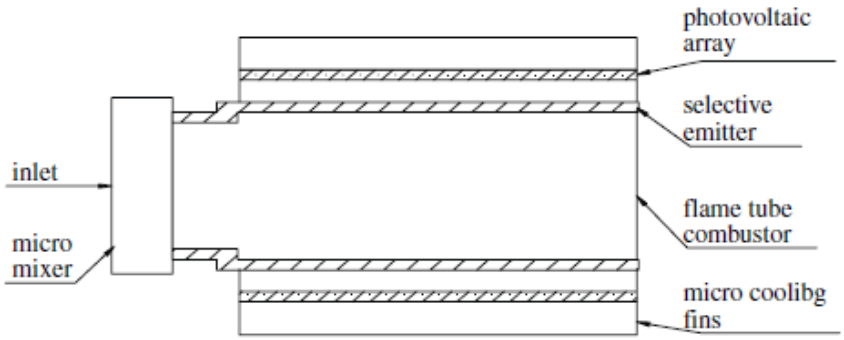

Figure 3.2 *– Yang's design of a microthermophotovoltaic system (©IEEE)*

Yang et al. have used both a silicon carbide (SiC) emitter, which is a blackbody emitter, and selective emitters, with further discussions on various different selective emitters. The desired wavelength range for this work is lower than our target wavelength, with the chosen selective emitter having an optimal range of 1 to 2 μm. Perhaps the selective emitter could be adapted to operate at different wavelengths, as the effect of varying the doped level of the emitter could potentially alter the optimal range of emission [15].

The photovoltaic cells used by Yang et al. were GaSb cells, which will absorb energy from photons in the range 350 to 1750 nm, which is again too low for the desired application. GaInAsSb cells were also tested, and were found to have a higher wavelength limit of 2400 nm [15], which is within the required wavelength range. Therefore, if this could be extended using a different configuration of heterostructures, a photovoltaic could be found which is within the correct range. Any such photovoltaic cell would be fabricated on a rigid substrate and therefore would have to been designed as a thin film in order to be wrapped around the exhaust pipe but it could also be used in a rigid form to prove the operating success of the design initially, until an organic equivalent or a thin film had be designed and tested.

Further research has taken place involving InAsSb PV cells [18], which have the spectral response shown in Figure 3.3 [18]. Although the responsivity decreases with temperature, it has been shown that photovoltaic cells exist that will operate at the desired wavelengths. Furthermore, the temperature of the cells could be reduced by the air flow around the exhaust pipe, and by a physical gap between the emitter and photovoltaic.

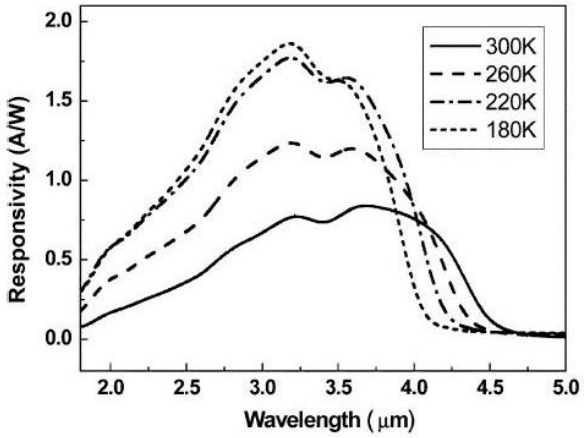

Figure 3.3 *– Spectral response of an InAsSb PV cell at different temperatures (©IEEE)*

There are numerous advantages to μTPV. Firstly, there are no moving parts with micro-thermophotovoltaic devices, eliminating any possibility of failure due to mechanical wear. The output from each element is a voltage, which can then be connected with the others in the correct series and parallel arrangement to provide the correct voltage and current for the purpose. The μTPV can also be manufactured as a flexible wrap, which will allow large areas to be created and installed onto the car exhaust more easily, compared to the thermoelectric device. The design of the thermophotovoltaic also results in lower costs than the thermoelectric design and it has the potential to involve higher efficiencies.

μTPV also have some disadvantages. As mentioned, greater than band gap radiation heats up the photovoltaic which could damage it, and therefore a selective emitter or a filter must be used. Furthermore, high energy photons will have excess energy, which will also generate heat, meaning the filter will also have to be able to act as a band pass device. The addition of such a filter adds an additional level of

complexity in terms of manufacture to the product.

For the desired purposes, the μTPV will have to operate at wavelengths, which are larger than used previously [19], the increase in wavelength reducing the energy per photon available. Ideally, a hotter temperature would have made this device more appealing, whereas the wavelength range available has no proven hardware yet.

Any improvements in this field will be incremental as, although μTPV is not as widely researched as thermoelectric, it is still a field of great interest. The efficiencies involved with current micro-thermophotovoltaics are up to 27.3 % [20] when converting energy from a hydrogen source by altering the hydrogen/air ratio of the heat source to 0.8.

3.4 Rectenna Devices

An alternative technology to consider is the antenna coupled rectifying diode device or rectenna. Rectennas are considered an alternative to μTPV, based on designing an antenna, which resonates at the desired frequency of the IR radiation. This resonance causes an AC signal at the same frequency as the radiation, which can then be converted into a DC signal, as can be seen from the two diagrams in Figure 3.4. Figure 3.4 (left) shows the antenna and diode configuration and Figure 3.4 (right) shows the equivalent circuit diagram. The main component in this device is the diode, the antenna collects the radiation but the diode must be fast enough to rectify it.

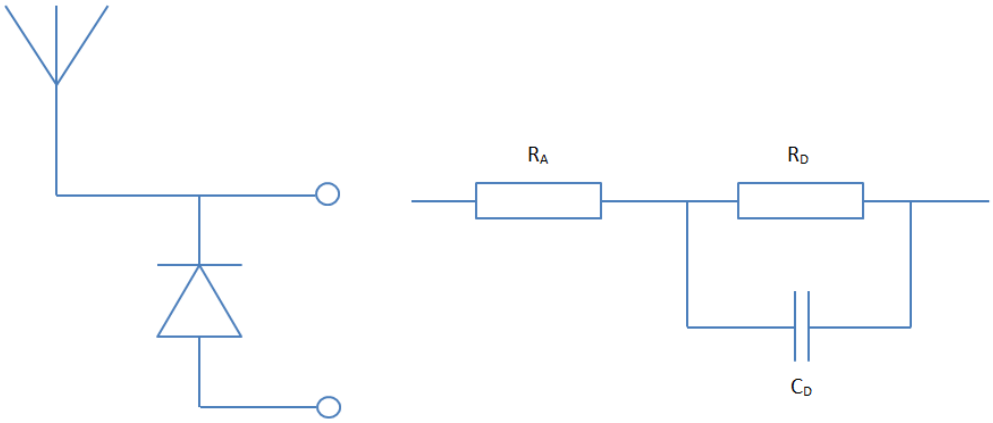

Figure 3.4 *– (left) antenna and diode configuration and (right) the equivalent circuit*

The infrared we will be wishing to utilise is in the range 4.8 to 6.8 µm. As calculated from $c = f\lambda$, 4.8 µm ≡ 62.5 THz and 6.8 µm ≡ 44.1 THz.

Therefore, we require a diode, which has a switching frequency of up to approximately 70 THz. However, if we could design a diode which could switch at a lower switching frequency it could be used at the higher wavelength infrared, which equates to lower temperatures and therefore lower energies. This lower temperature could prove to be convenient if the temperature profile of the exhaust pipe shows cooler regions than expected. An initial device with slower switching speeds could be design for the coolest part of the exhaust, with the design being expanded to the hotter regions as diode speeds are increased.

3.4.1 Antennas

Antenna shape and type affect the radiation patterns, which are a performance factor of the antenna. The ability of the antenna to respond to the radiation also depends on the polarisation of the radiation as well as the angle of incidence [21]. However, at high frequencies, the scaling of the antenna with the wavelength of the incident radiation is not linear as conduction is not ohmic, as the majority of the conduction occurs on the surface of the antenna (known as the skin effect, with surface losses becoming important). This must be considered when designing the array [22].

The impedance of IR antenna materials is much higher than those at microwave frequencies due to the skin effect. This high surface impedance causes losses that can slow antenna currents so the antenna does not radiate efficiently. Furthermore, this impedance must be matched between the antenna and the diode in order to prevent losses [22].

Previously, Bailey et al. have described pairs of antennas connected to a diode in a half wave rectification arrangement. In this configuration, the elements needed to be several wavelengths long to permit fabrication [23]. An alternative approach was undertaken by Marks, who used arrays of crossed dipole antennas with full wave rectification. In this way, the output from several dipoles fed into a transmission line and then their combined power would be directed to the rectifier [24]. This, however, requires the oscillations from each dipole to be in phase. Marks later patented the design for antenna-like cylinders, each with a diode for rectification [25]. This would only equate to half wave rectification, which in turn is wasting half of the energy available. However, if full wave rectification is used it would mean four diodes would be needed per antenna. Furthermore, for the dipoles used in this patent, they had to be placed perpendicular to each other in order to facilitate optimal absorption.

Antenna Design Options

Dipole antennas are the most common choice for rectenna devices due to their simplicity and ease of fabrication [26]. However, alternative options exist.

A folded dipole antenna is very similar to a standard dipole antenna but the ends are folded and connected together, as seen in Figure 3.5. Because the dipole is folded, the currents can reinforce each other rather than cancelling out. The impedance of the folded antenna depends on the impedance of a standard dipole of length L. The folded dipole is resonant at odd integer multiples of a half-wavelength and the input impedance is higher than that for a half dipole [25].

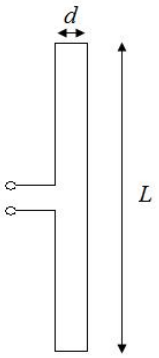

Figure 3.5 *– Diagram of a folded dipole antenna, showing critical dimensions d and L*

Spiral antennas, seen in Figure 3.6 can be made to have frequency independent impedance when the shape is only specified by angles. Curvature of the spiral causes attenuation of the antenna current [27]. In order to improve the efficiency of the spiral, a square spiral could be used to optimise the area covered by the antenna.

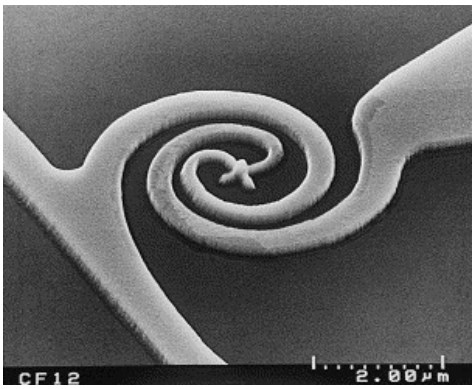

Figure 3.6 *– SEM image of a spiral antenna used in a rectenna device*

Bow tie antennas are also a potential option, as seen in Figure 3.7 [27]. They are geometrically simple to fabricate and their size does not affect their functionality, as the gain of a bow tie antenna is not improved by increasing its length. However, it has been found that spiral antennas yielded a higher gain than the best bow tie antennas tested [27]. Therefore the decision between these two options is a compromise between fabrication difficulty versus antenna capabilities.

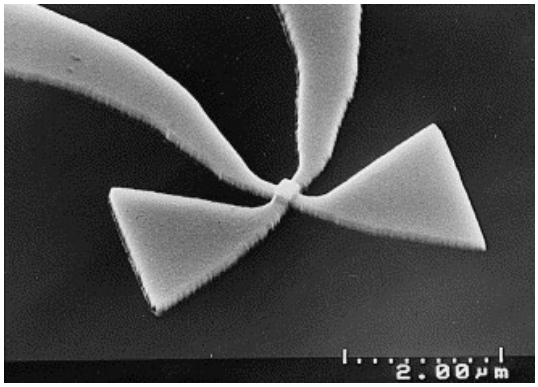

Figure 3.7 *– SEM image of a bowtie antenna used in a rectenna device*

Square spiral antennas, as seen in Figure 3.8 could be fabricated as an alternative option to standard spiral antennas, which would then allow optimisation of antenna area coverage. With square spiral antennas, as long as the permittivity of the substrate is known, the minimum feature size can be determined for a chosen frequency [28]. For example, for a GaAs substrate at 70 THz, the minimum feature size required is 136 nm.

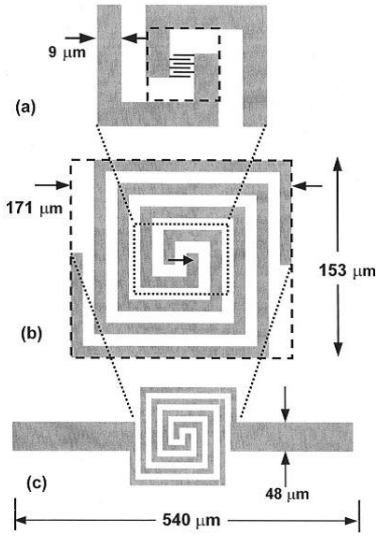

Figure 3.8 *– Example Square Spiral, showing minimum (a) and maximum (b) perimeters in dotted lines*

3.4.2 Advantages of Rectenna Arrays

The micro-antennas rely on resonance in order to function, operating based on their physical geometry. Each individual device will have a minuscule surface area, resulting in an enormous number of these devices across the surface area of the

exhaust. Therefore an array of devices is a real possibility, with the size of the antennas perhaps varying according to the temperature profile of exhaust pipes, thus maximising efficiency across the varying temperatures.

3.4.3 Disadvantages of Rectenna Arrays

These devices are limited by the working dimension of the manufacture process. The size of each antenna is determined by the wavelength, which can result in feature dimensions sub-100 nm, which would be challenging with standard lithographic techniques. The high switching frequency of the diodes is also a concern, as their size must be minimised to increase the maximum operating frequency.

Array connections are a concern as if this is a series array and one device fails, which in such high numbers is likely, the entire array would fail. A contingency plan must be in place to overcome this, say multiple series arrays connected in parallel for example. These devices are also not as simple to integrate as μTPV due to the rectification step, which may result in up to 4 diodes per antenna.

3.4.4 Figures of Merit

In order to be able to compare devices and improve them, universal figures of merit must be used and are therefore discussed [29], [30]. Voltage responsivity relates output voltage to input power of the incident radiation. Voltage responsivity is defined as:

$$\beta_v = \frac{V_o}{P_i} \tag{3.3}$$

where,

β_v = voltage responsivity [$\mathrm{V\,W^{-1}}$]

V_o = voltage output [V]

P_i = incident power [W]

Voltage responsivity is a common figure of merit but it is difficult to use to compare different devices, as it does not allow for device area and it is also a function

of wavelength and therefore only devices of equal area can be compared, when measurements are taken at the same frequency.

The signal to noise ratio is an important figure of merit. It is a measure of the ratio between the detected signal and the noise level. Only signals which are greater than the noise level can be detected and so this gives a measurement of how sensitive a device is to low level signals. Given this ratio, comparison between devices can only occur when they have both been subject to the same input power.

The noise equivalent power is another figure of merit which can be used to help compare different devices by providing a measure of the power incident on a detector which results in a signal to noise ratio of 1. The noise equivalent power is given by Equation 3.4. Some people define NEP as the minimum detectable power per square root of bandwidth. When defined this way, NEP has the units of $\mathrm{W/Hz^{\frac{1}{2}}}$. The term is a misnomer, because the units of power are watts. Therefore, for continuity of units in defined equations, hereafter NEP will be defined in this thesis as having the units of watts.

$$NEP = \frac{V_n}{\beta_v} \tag{3.4}$$

where,

NEP = noise equivalent power (NEP) [W]

V_n = noise voltage across diode [$\mathrm{V\,Hz^{-1}}$] [31]

This is still dependent on the area and bandwidth of the device and therefore these factors must be included when comparing devices. One way to correct this issue is to normalise the noise equivalent power to a $1\,\mathrm{cm^2}$ area with a $1\,\mathrm{Hz}$ bandwidth, which is known as the normalised detectivity, described by Equation 3.5.

$$D^* = \frac{(A_{\mathrm{ant}}\Delta f)^{0.5}}{NEP} \tag{3.5}$$

where,

D^* = detectivity [$\mathrm{mHz^{\frac{1}{2}}W^{-1}}$]

A_{ant} = antenna capture area [$\mathrm{m^2}$]

Δf = bandwidth [Hz]

An adaptation to this was proposed in [32], which includes the various efficiencies associated with 'rectenna' devices and can be seen in Equation 3.6.

$$D^* = \frac{(A_{\text{ant}}\Delta f)^{0.5}}{NEP}\eta_a\eta_s\eta_c\eta_j \tag{3.6}$$

where,

η_a = the efficiency of coupling radiation to antennas

η_s = the efficiency of propagating the energy to the diode

η_c = the efficiency of coupling antenna modes to diode modes

η_j = the efficiency the tunnelling junction

η_a is a measure of the efficiency of the antennas in collecting the incident radiation, which will be affected by the nature of the radiation and could be either coherent or incoherent. A coherent radiation source must be both in phase and at only one wavelength in order to be considered truly coherent. Unfortunately, no natural radiation source is coherent, with the main coherent sources being lasers. Single wavelength, in phase sources would be relatively straightforward to optimise a detection device around and none of the radiation would be lost due to interference between out of phase components.

Incoherent sources, by contrast, will have an associated bandwidth and the radiation will therefore not be in phase. For this radiation, broadband antennas would have to be used and their frequency range for collection taken into account when designing rectenna devices and arrays. Antennas such as bow-tie (flared dipole) antennas and spiral antennas have been shown to operate as broadband antennas in rectenna devices [27]. However, coherent radiation sources, i.e. lasers, would be a more suitable choice with regards to device proof of concept tests as these would enable the fabrication design complexity to be reduced significantly.

η_s is the efficiency associated with the radiation travelling from the antenna to the diode, which is why the distance between the two must be minimised. η_c is the efficiency of coupling the antenna energy at the junction and is affected by both the geometry of the junction as well as the materials used in the device fabrication.

Finally, η_j is the junction efficiency, which is determined by how fast the energy is tunnelled through the junction compared to how quickly it is dissipated. All of these efficiencies must be considered.

3.4.5 Carnot Efficiency

Of the efficiencies within the device, which were discussed in Section 3.4.4 (η_a, η_s, η_c and η_j), the junction efficiency (η_j) is bounded by the Carnot efficiency. Carnot efficiency sets a fundamental limit to the conversion of heat from a thermal source to useable power (work). Therefore this fundamental limitation must be determined for a rectenna device.

Figure 3.9 represents a rectenna device at the temperature of a cold reservoir (T_C) receiving power in the form of radiation (P_{IN}) from a hot source (T_H), and reflecting some back (P_{OUT}). Assuming that the system is reversible, the work output from the rectenna (W) can be returned to the hot source using a heat pump. However, the limitations of this thermodynamic system are the two efficiencies (η_A and η_C), which are the rectenna and Carnot efficiencies respectively.

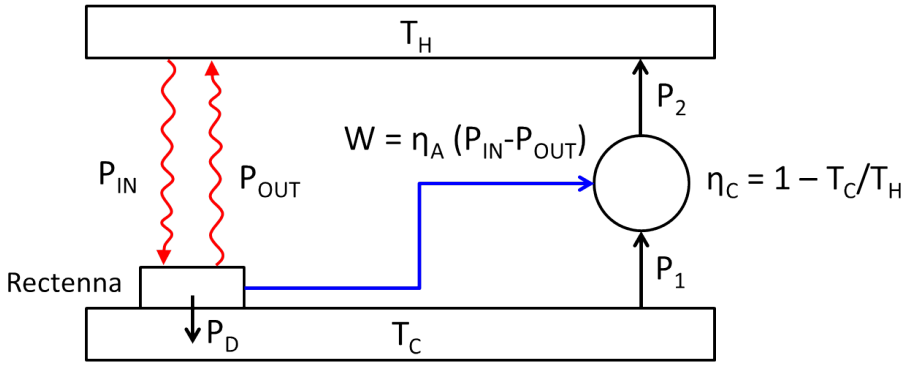

Figure 3.9 – *Carnot efficiency diagram, courtesy of Dr Claudio Balocco*

Equation 3.7 shows the equation for the system seen in Figure 3.9. As can be seen, the efficiency of the rectenna device is equal to the Carnot efficiency of the system.

$$P_{IN} - P_{OUT} = P_2 = \frac{W}{\eta_C} = \frac{\eta_A}{\eta_C}(P_{IN} - P_{OUT}) \implies \eta_A = \eta_C \tag{3.7}$$

As seen in Figure 3.9, the Carnot efficiency is determined by the temperature difference between the hot and cold reservoirs, and is described by Equation 3.8.

$$\eta_C = 1 - \frac{T_C}{T_H} \tag{3.8}$$

For example, if a hot source was at a temperature of 300 °C, or 573 K, then assuming a cold reservoir at room temperature, the Carnot efficiency, and therefore maximum diode junction efficiency, would be 49 %. However, the Carnot efficiency can be increased to approaching unity [33] by minimising the bandwidth of the incident radiation, as can be seen in Figure 3.10.

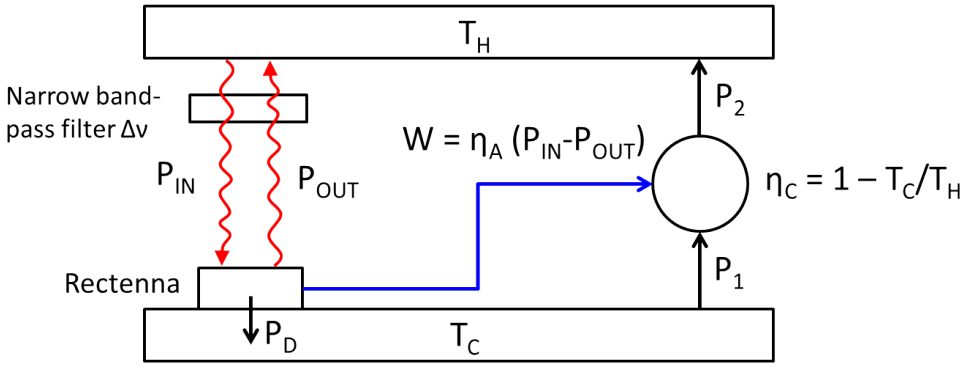

Figure 3.10 – *Narrow bandwidth Carnot efficiency diagram, courtesy of Dr Claudio Balocco*

Here, a narrow band-pass filter (bandwidth $\Delta\nu$) is added between the radiation source and the rectenna, ($P_{IN} - P_{OUT} \propto \Delta\nu$). As $\Delta\nu \to 0$ (coherent radiation), in order for ($P_{IN} - P_{OUT}$) to be finite, $T_H \to \infty$ and therefore $\eta_C \to 1$. Therefore, the Carnot efficiency of a rectenna device is a function of the source temperature and bandwidth [34]. However, in reality a unity Carnot efficiency cannot be achieved due to the requirement for an infinitely hot radiation source.

However, a compromise must be reached when filtering the radiation, between improving the Carnot efficiency of the system by narrowing the bandwidth and losing a significant proportion of the radiation. If, for example, the Carnot efficiency of the system is approaching unity but only 1 % of the radiation reaches the device then the optimisation of the Carnot efficiency becomes irrelevant. This must be considered when designing the device.

An adaptation on the Carnot efficiency is the Curzon-Ahlborn efficiency, which provides the Carnot limited efficiency available from a device at maximum power rather than zero power, and is given by Equation 3.9

$$\eta_{CA} = 1 - \sqrt{\frac{T_C}{T_H}} \tag{3.9}$$

This can be used to provide an estimate of the amount of power available from a single diode. From the calculations in Chapter 2, assuming an exhaust temperature of 250 °C, and an associated power of 9.2 kW available across 2.4 m^2 of exhaust pipe (as described in Table 2.4), as well as a single device area of 1 μm^2, the total power available to the diode is 3.8 nW, and furthermore, with a Curzon-Ahlborn efficiency of 0.24, there would be 0.9 nW of power available from each device, if it is cooled to room temperature. This estimation only includes the Curzon-Ahlborn efficiency, and does not include the other efficiencies previously discussed as they would be heavily dependent on antenna design.

3.5 Methods of Energy Recovery Conclusions

Numerous technologies, both in the automotive industry and elsewhere, exist but they have their disadvantages. Rectenna devices look like a promising alternative, using MST technology over a large area. The different antenna designs can have a huge impact on device efficiency but are not a focus for this project as their fabrication is comparatively straightforward. The main challenge is to create a diode suitable for such an application, which will be discussed in Chapter 4.

The devices are fundamentally limited by Carnot efficiency, but the efficiency can be maximised by narrowing the bandwidth of the radiation being selected, thus implying that either narrowband radiation recovery or radiation detection may be a better application than broadband infrared recovery.

Chapter 4

Diodes

4.1 Introduction

This chapter discusses the conduction mechanisms found in many types of diodes and also discusses which existing technologies could be useful. The aim is to determine which conduction mechanisms would be useful and therefore should be designed into fabricated diodes. Each of the conduction mechanisms varies in suitability for this application and so the aim is to design and produce diode structures which will take these mechanisms into account.

A common diode is the PN junction diode, which relies on the formation of a PN junction in a material, which causes conduction in one direction but not the other, with drift and diffusion currents acting as the dominant mechanisms for conduction [35]. This process, however, is inherently slow as it is a process which relies on minority carriers which, once transferred across the junction, must recombine with majority carriers before the device can be considered stable enough to be switched again. Therefore more suitable alternative mechanisms and existing diodes will be discussed. Furthermore, a fast, low voltage mechanism is desirable and therefore both self-switching diodes and metal-oxide-metal (MOM) diodes are discussed as potential design options, with structure, size and manufacturing considerations for the MOM diode discussed. MOM diodes will form the basis of the rest of the thesis.

4.2 Conduction Mechanisms

Due to the need for a fast rectifying device, the relevant, high speed conduction mechanisms, which could take place in a high speed device, are discussed. Schottky conduction, which relies on thermionic emission of carriers over a barrier, is discussed as in higher voltage regimes this could be the dominant effect. Various forms of high speed electron tunnelling are also discussed as these would be the desired forms of conduction. These include direct electron tunnelling, Fowler-Nordheim tunnelling, as well as trap assisted tunnelling, which includes variable range hopping, two-step tunnelling, multistep tunnelling, inelastic tunnelling and Poole-Frenkel conduction. These mechanisms would be more likely to occur in a lower voltage regime, where there is insufficient energy for carriers to overcome the barrier but instead travel through it in some form.

4.2.1 Schottky Effect

The Schottky effect is caused due to the fact that above 0 K there will be a number of electrons with energy higher than the barrier height at a metal-semiconductor or metal-insulator interface. These electrons have a high probability of overcoming the barrier and therefore the number of electrons able to do this is determined by the barrier height and the temperature.

A Schottky barrier is formed when a metal and semiconductor are brought into contact and a junction is formed between them. This can happen in a p-type semiconductor ($\phi_s > \phi_m$) or in an n-type ($\phi_m > \phi_s$) where ϕ_m and ϕ_s are the metal and semiconductor work function respectively. The Fermi levels equalise and align, and the other bands (semiconductor conduction and valence bands) bend accordingly. To do this, electrons are transferred from semiconductor to metal, creating a depletion region in the near surface of the semiconductor and an excess of negative charge on the metal side, as seen is Figure 4.1 (adapted from [35] for an n-type semiconductor).

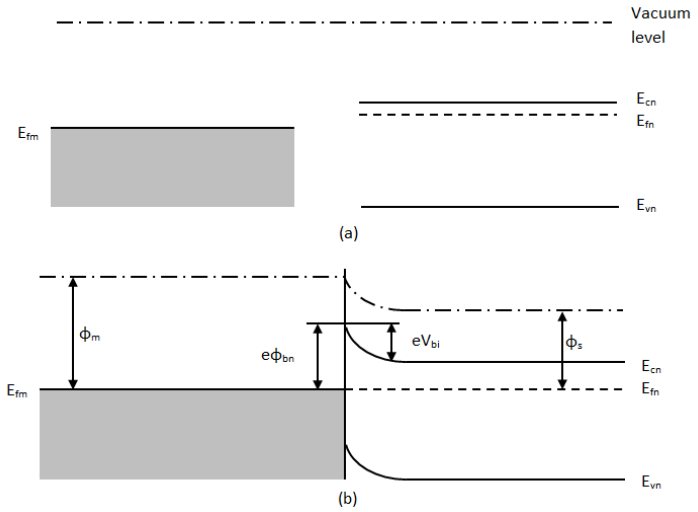

Figure 4.1 *– Formation of a Schottky barrier - (a) a metal (left) and a semiconductor (right) prior to junction formation, (b) a Schottky barrier*

The Schottky effect occurs when the electrons on the semiconductor side of the junction have sufficient energy to reach the conduction band at the interface. Assuming a triangular barrier at the interface, the resulting current is due to the electrons that are above the potential barrier, which can be expressed in Equation 4.1 [35–37]. The junction is dominated by thermionic emission of majority carriers over a potential barrier.

$$J = J_S \left\{ exp\left(\frac{eV}{nkT}\right) - 1 \right\} \tag{4.1}$$

where

$$J_S = A^* T^2 exp\left\{ -\frac{\left(e\phi_{bn} - e\left(\frac{eV}{4\pi d\varepsilon_0\varepsilon_r}\right)^{\frac{1}{2}}\right)}{kT} \right\} \tag{4.2}$$

where

n = ideality factor

A^* = effective Richardson constant [$A\,m^{-2}\,K^{-2}$]

d = oxide thickness [m]

e = electron charge = 1.6×10^{-19} C

ε_0 = permittivity of free space [F/m]

ε_r = relative permittivity

V = applied voltage [V]

ϕ_{bn} = barrier height [V]

In order to gain an understanding of Schottky conduction, the effects of applied bias have been investigated. With a Schottky barrier, there are two drift currents, one from metal to semiconductor and one semiconductor to metal. With no applied bias these are equal and therefore cancel, resulting in no net current flow. With a positive applied bias, V_{bi} becomes V_{bi}-V, raising the conduction band of the semiconductor, while keeping the barrier height constant (i.e. the 'bend' in the semiconductor conduction band reduces), which causes the semiconductor to metal electron transport to dominate, as seen in Figure 4.2.

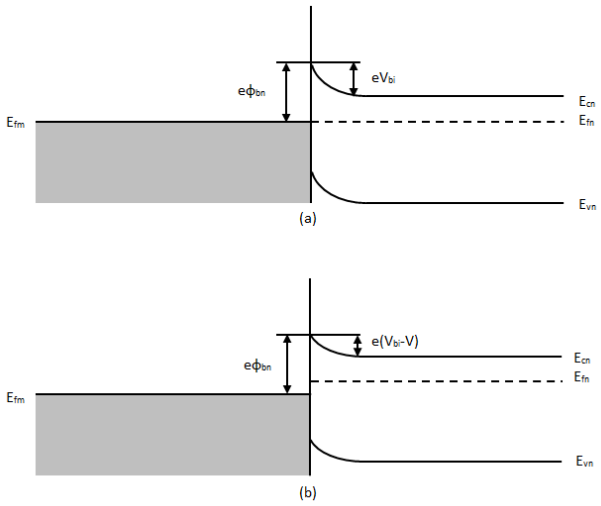

Figure 4.2 *– The effect of positive bias on a Schottky barrier - (a) shows no bias, (b) shows positive bias*

By contrast, when a negative bias is applied, V_{bi} becomes V_{bi}+V, lowering the semiconductor conduction band and reducing the semiconductor to metal electron flow below that of the opposing drift causing the latter to dominate, resulting in a lower net current flow in the opposite direction, as seen in Figure 4.3.

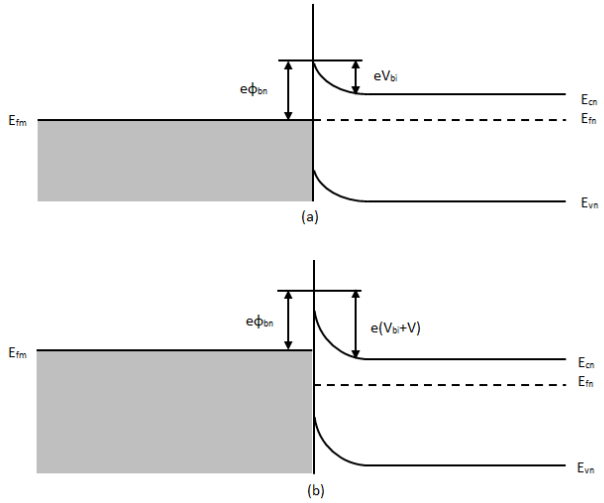

Figure 4.3 – *The effect of negative bias on a Schottky barrier - (a) shows no bias, (b) shows negative bias*

The most common application of the Schottky effect is on a semiconductor-metal interface. However, it is also possible for this effect to occur at an insulator-metal interface, as there is still a barrier for the carriers to overcome. Equation 4.1 can be separated into two sections; a voltage dependence (the exponential in Equation 4.1 and a square root voltage dependence (J_s, as defined in Equation 4.2). The square root voltage dependence in Equation 4.2 is normally so small in Schottky diodes that it is usually omitted to leave a constant term for J_s. However, the square root voltage term is due to barrier height difference at the interface and therefore is significant for a metal-insulator interface. By contrast, the voltage dependence is omitted as it is not applicable for a non-semiconductor interface, resulting in the Schottky effect for a metal-insulator interface simplifying to Equation 4.3:

$$J = A^*T^2 exp\left\{\frac{e\left(\beta V^{\frac{1}{2}} - \phi_{bn}\right)}{kT}\right\} \tag{4.3}$$

where

$$\beta = \left(\frac{e}{4\pi d\varepsilon_0\varepsilon_r}\right)^{\frac{1}{2}}$$

In order to analyse any experimental data to determine whether Schottky conduction is the correct mechanism, it is favourable to plot the data in the form of a straight

line with known gradient and intercept. Therefore Equation 4.3 must be rearranged for both temperature and voltage dependence. As seen in Equation 4.4, the natural logarithm must be taken.

$$ln\frac{J}{T^2} = lnA^* + \frac{e\beta V^{\frac{1}{2}}}{kT} - \frac{e\phi_{bn}}{kT} \tag{4.4}$$

This equation can then be rearranged into two different forms, as seen in Table 4.3 in Section 4.8, which can be used to compared theoretical trends with experimental results, which will be discussed further in Chapter 6 and Chapter 7.

4.2.2 Electron Tunnelling

One of the fastest and therefore most relevant mechanisms is electron tunnelling. However, electron tunnelling relies on quantum mechanisms rather than classical mechanics and therefore the differences between these two forms of mechanisms must be investigated [38]. Consider the barrier potential seen in Figure 4.4.

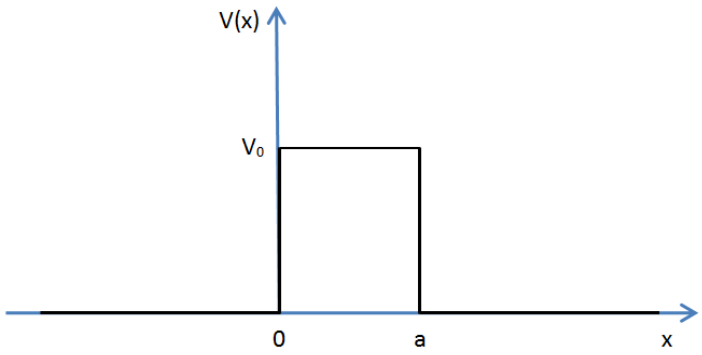

Figure 4.4 – *Potential barrier*

In classical mechanics, a particle of energy E at $x < 0$ would have a probability of being reflected equal to 1 if $E < V_0$ and a probability of being transmitted to $x > a$ of 1 if $E > V_0$. By contrast, quantum mechanics would suggest that if E is larger than V_0 but only slightly so then there would be some reflection, and similarly if E is slightly smaller than V_0 there is also a probability than transmission through the barrier will occur. By tunnelling through the barrier despite insufficient energy to overcome it, the particle behaves like a wave. The probability density function

for a typical barrier can be seen in Figure 4.5, with a standing wave at $x < 0$, which is offset due to a small reflected wave with an amplitude less than the incident wave. In the region $x > a$ the wave is a travelling wave and so the probability density is constant but finite. In the region $0 < x < a$ the wave function is an exponentially decaying standing wave, the probability of which confirms this. From here it is apparent that the thickness of the barrier is vital in order to ensure that the decay through the barrier does not decrease to zero before the end of the barrier. The barrier must be thin enough that the barrier ends before the exponential decay reduces the probability to zero.

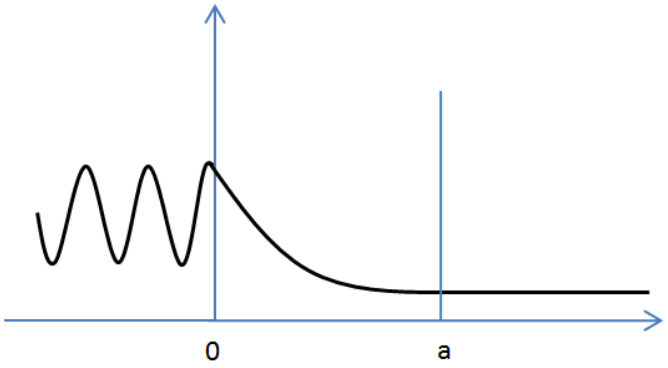

Figure 4.5 – *Probability density function for a typical barrier*

This contrast between classical and quantum mechanics can be used to further investigate electron tunnelling. A square potential well, seen in Figure 4.6, can be used to bind a particle within it.

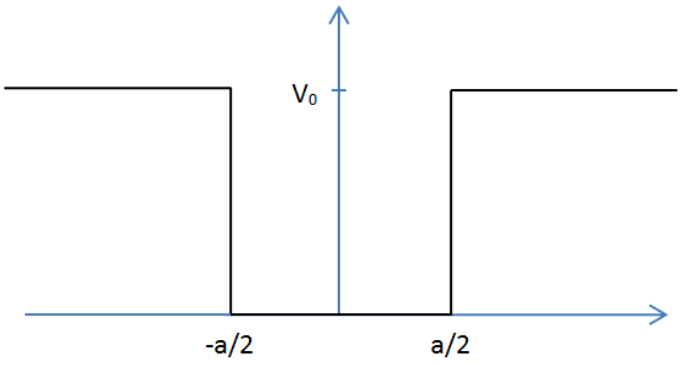

Figure 4.6 – *Potential well*

In classic mechanics it the particle energy $E < V_0$ then the particle will be bound within $\frac{-a}{2} < x < \frac{a}{2}$. Furthermore, the particle will bounce back and forth within

the well and any energy value within the well is possible. By contrast quantum mechanics says only discrete energy values are possible.

$$\psi(x) = Ae^{ik_I x} + Be^{-ik_I x} \tag{4.5}$$

where,

$k_I = \dfrac{\sqrt{2m_e E}}{\hbar}$

m_e = electron mass [kg]

E = energy [J]

x = position in well

The first term in Equation 4.5 describes wave travelling in one direction in the well, and the second term describes the opposite direction. It is assumed that a particle bouncing inside a well consists of an equal mixture of waves in both directions and so by applying $A = B$ and $-A = B$ for standing wave conditions, Equation 4.5 can be rearranged into the form of Equation 4.6.

$$\psi(x) = A' sink_I x + B' cosk_I x \tag{4.6}$$

where,

$B' = 2B$

$A' = 2iA$

Now outside the well region can be considered. For $x < -a/2$, Equation 4.7 is true.

$$\psi(x) = Ce^{k_{II} x} + De^{-k_{II} x} \tag{4.7}$$

For $x > a/2$, Equation 4.8 is true.

$$\psi(x) = Fe^{k_{II} x} + Ge^{-k_{II} x} \tag{4.8}$$

where,

$$k_{II} = \frac{\sqrt{2m_e(V_0 - E)}}{\hbar}$$

There are now 6 arbitrary constants to find: A', B', C, D, F, and G. D=0 and F=0 as if not $\psi(x) \to \infty$ as $x \to \pm\infty$. The other four can be found by the assumption that $\psi(x)$ and $d\psi(x)/dx$ must be continuous at the wall boundary for a continuous waveform to occur. This combined with an additional E constant which is used to define the energy magnitude of the particle defines the waveforms. Each waveform is a standing wave within the well and an exponentially decaying wave in the wall region, as seen in Figure 4.7.

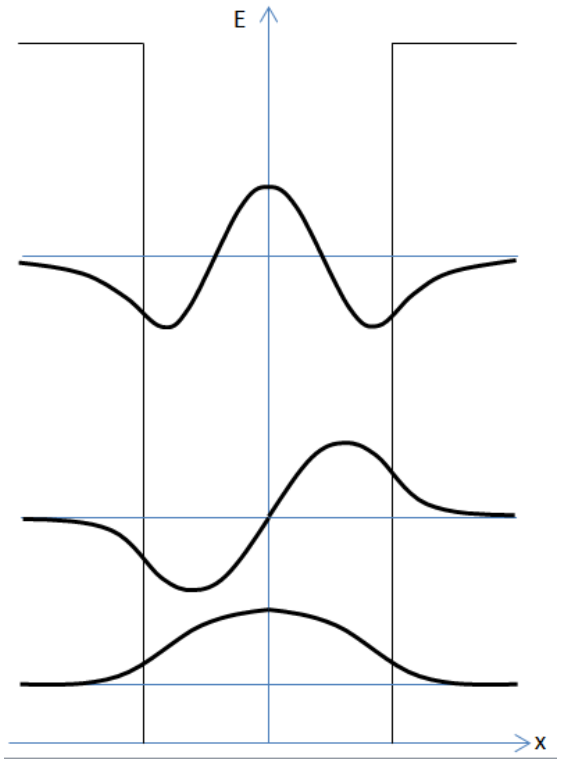

Figure 4.7 – *Three standing waves in a finite potential well*

The decay through the barrier is exponential, and therefore the barrier must be sufficiently thin that the probability of electron occurrence does not decrease to zero. This makes tunnelling mechanisms desirable as the ability to tunnel through a thin barrier is faster and also can take place in a much lower voltage regime. However, there are many forms of electron tunnelling which must be considered. The two main forms of trap free tunnelling are direct electron tunnelling and Fowler-Nordheim

tunnelling, as seen in Figure 4.8, which shows both Fowler-Nordheim tunnelling (a) and Direct Electron Tunnelling (b), both of which will be discussed in more detail.

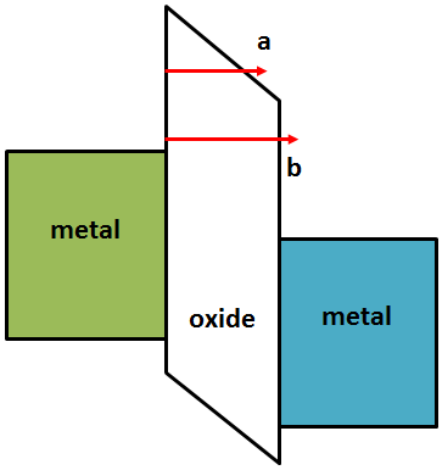

Figure 4.8 – *Electron tunnelling - (a) Fowler-Nordheim, (b) Direct electron tunnelling*

Direct Electron Tunnelling

Direct electron tunnelling theory is the most direct form of tunnelling conduction and is based upon the probability of an electron tunnelling through a central barrier and existing on the other side under applied bias. In order for this to occur, the barrier thickness should be 5 nm or thinner [36]. The tunnelling current is given by Equation 4.9 [39].

$$J = \frac{em^*V^2}{8\pi h\phi_{bn}m_{ox}d^2\left[1-\left(1-\frac{V}{\phi_{bn}}\right)^{1/2}\right]^2} exp\left\{-\frac{4d\,(2m_{ox})^{\frac{1}{2}}}{3e\hbar V}\left[(e\phi_{bn})^{\frac{3}{2}}-(e\phi_{bn}-eV)^{\frac{3}{2}}\right]\right\} \tag{4.9}$$

where,

m^* = free electron mass [kg]

m_{ox} = effective electron mass in the oxide [kg]

h = Planck's constant [Js]

$\hbar$ = reduced Planck's constant [Js]

ϕ_{bn} = barrier height [V]

d = oxide thickness [m]

V= applied voltage [V]

Here the electrons successfully tunnel directly from the conduction band on one side of a barrier to the conduction band of the metal on the other side, through the full thickness of the barrier, without any intermediate steps. Therefore, this would be the most suitable mechanism as it is the quickest and most direct mechanism of those discussed.

Fowler-Nordheim Conduction

In contrast to direct electron tunnelling, Fowler-Nordheim tunnelling is a form of tunnelling which involves very high electric fields (in excess of $6\,\mathrm{MV\,cm^{-1}}$ [36]) and generally thicker oxides. Furthermore, the main difference between direct electron tunnelling and Fowler-Nordheim tunnelling is determined by the shape of the oxide barrier, as seen in Figure 4.8. If the barrier is triangular then Fowler-Nordheim tunnelling occurs, as the electrons will tunnel successfully to the oxide conduction band, then continue to travel to the other side of the oxide barrier via the conduction band. By contrast if the barrier is trapezoidal then direct electron tunnelling will occur [40]. The current density of Fowler-Nordheim conduction is given by Equation 4.10.

$$J = \frac{em_m V^2}{8\pi h \phi_{bn} m_{ox} d^2} exp\left\{ -\frac{4d\,(2m_{ox})^{\frac{1}{2}}}{3e\hbar V}\,(e\phi_{bn})^{\frac{3}{2}} \right\} \tag{4.10}$$

where

m_m = effective electron mass in metal [kg]

As with previous mechanisms, a summary of the straight line derivation can be found in Table 4.3 in Section 4.8. This mechanism is more likely to occur in a fabricated device if the barrier is too thick for direct electron tunnelling to occur. It is, however, another trap free mechanism. Conduction through oxides which have defects, or traps, must also be considered.

4.2.3 Trap-Assisted Tunnelling

For oxides thicker than those through which direct electron tunnelling can occur, alternative, indirect forms of conduction exist in trap assisted tunnelling. Rather than tunnelling through the oxide in its entirety, if the layer has defects then there is the possibility of trap-assisted tunnelling to occur. This involves electron tunnelling to intermediate steps within the oxide sequentially in order to travel through it. This allows tunnelling to occur through a thicker oxide but it also has the potential to slow the conduction, depending on how many trap steps exist. The current density through a barrier is described in Equation 4.11 [41].

$$J = e \int_0^d \frac{N_T(x)}{\tau_c(x) + \tau_e(x)}\, dx \tag{4.11}$$

where

N_T = Trap concentration [m^{-3}]

τ_c = Trap capture time [s]

τ_e = Trap emission time [s]

As can be seen, the current density depends on the density of traps within the oxide and the amount of time taken to enter and leave each trap, integrated over the oxide thickness.

Several forms of trap assisted tunnelling exist. Figure 4.9 shows the various forms of such tunnelling (adapted from [42]). With regards to elastic tunnelling, conduction can occur when carriers travel to another trap of the same energy (multi-step tunnelling or hopping), tunnelling through the barrier (two step tunnelling), or excitation to the conduction band of the insulator (Poole-Frenkel Conduction).

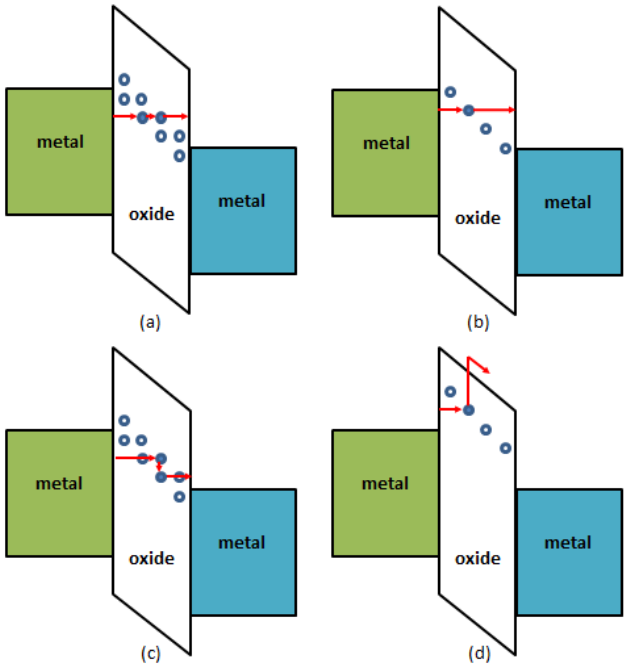

Figure 4.9 – *Trap assisted tunnelling summary (a) multi-step tunnelling, (b) two-step tunnelling, (c) inelastic tunnelling and (d) Poole-Frenkel Conduction*

Variable Range Hopping Conduction

Elastic Multi-step tunnelling, or hopping conduction, is a process by which tunnelling occurs between traps of the same energy sequentially until the barrier has been traversed successfully. Equation 4.12 shows the hopping conduction dependence as seen in [36].

$$J = \frac{e^2 n^* \alpha^2 V}{kTd\tau_0} exp\left\{-\frac{4\pi m^* e\phi_m \alpha}{h}\right\} \tag{4.12}$$

where

n^* = electron density at the trap sites [m^{-3}]

α = distance between the trap sites [m]

τ_0 = time constant [s]

ϕ_m = barrier height between two sites [V]

Inelastic trap assisted tunnelling also occurs, whereby the carrier loses energy as it moves through the barrier, and therefore each transport between traps involves movement to lower energy states.

Poole-Frenkel Conduction

Poole-Frenkel conduction (otherwise known as field-assisted thermal ionisation) is a bulk-limited process in which the conduction is driven by charge traps present within the material. The Poole-Frenkel current is described by Equation 4.13 [36, 43, 44].

$$J = \frac{eN_c\mu_e V}{d} exp\left\{\frac{e\left(\beta_{PF}V^{\frac{1}{2}} - \phi_{bn}\right)}{kT}\right\} \tag{4.13}$$

where,

$$\beta_{PF} = \left(\frac{e}{\pi d\varepsilon_0\varepsilon_r}\right)^{\frac{1}{2}} \tag{4.14}$$

N_c = density of states in the oxide layer conduction band [m^{-3}]

As can be seen the β constant in the Poole-Frenkel conduction varies by a factor of 2 compared to the same constant in the Schottky emission. This is due to the constant being different depending on conduction type and hence the difference between the two types of emission [45].

The equation can be rearranged for analysis, with the results seen in Table 4.3 in Section 4.8.

4.2.4 Combined Mechanisms

With a number of real world devices, a single conduction mechanism does not fully describe the nature of the conduction taking place. Often a combination of mechanisms is responsible. This can be caused by a single dominant mechanism, with others altering the trends slightly, or by different mechanisms dominating in different voltage or temperature regimes. One of the more common effects is the dominance of electron tunnelling at low temperatures, with thermionic emission beginning to dominate at higher temperatures. It is likely that in an amorphous film, a complex combination of mechanisms will be responsible for the overall method of conduction and that this effect has the potential to vary with temperature, frequency and applied voltage levels.

With the most likely conduction mechanisms discussed, the main high frequency

diodes must also be discussed to determine their suitability as high frequency rectifiers.

4.3 IMPATT Diodes

The first diode to be discussed is the IMPATT diode. Originally suggested by Read [46], the Impact Avalanche Transit-Time (IMPATT) diode involves a n^+-p-i-p^+ silicon structure and consists of two main regions: firstly the n^+-p region which acts as an avalanche multiplication region, and the p-i-p^+ region which can be considered to be intrinsic, through which holes drift while moving to the p^+ contact. n-i-n^+ regions can be used too with the added advantage that the electrons have a superior mobility compared to holes [47]. The IMPATT diode is operated under reverse bias, causing avalanche multiplication at the n^+-p interface, which is the point of maximum electric field [46, 47]. Figure 4.10 shows the production of an IMPATT diode pulse using a DC offset with AC input oscillation.

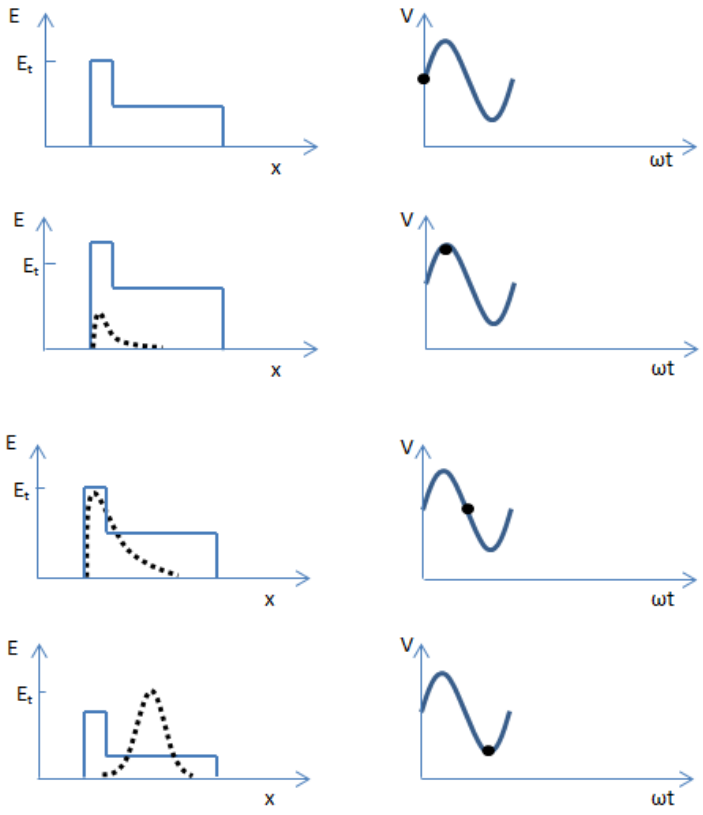

Figure 4.10 – *The production of a pulse using an IMPATT diode*

In order to produce an ouput, the input signal must overcome a threshold electric field, prior to which no output it produced (Figure 4.10(b)). Whenever the input exceeds the threshold electric field, E_t, (Figure 4.10(c)), holes are produced and because of the DC offset the holes continually drift through the intrinsic region to the p^+, resulting in time-based hole pulses being produced (Figure 4.10(d)), the duration of which can be controlled by the input voltage relative to the threshold electric field of the avalanche region. Due to the requirement of a threshold voltage in order to operate, this device would not be suitable for small signal rectification.

4.4 Gunn Diodes

Gunn diodes are based on GaAs, where the valence band maximum and conduction band minimum align, as seen in Figure 4.11 (left) (adapted from [47]).

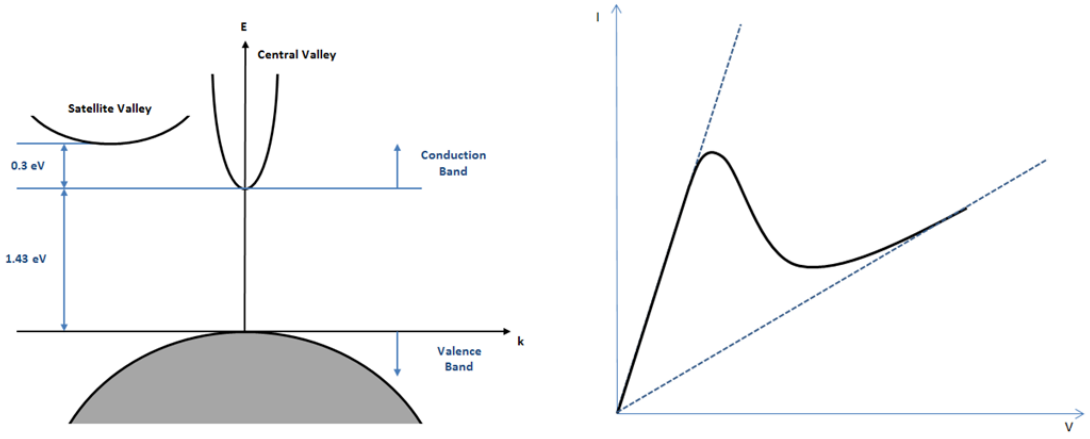

Figure 4.11 *– Simplified band diagram in k space for GaAs showing the two valleys in the conduction band (left) and Gunn diode I-V (right)*

Here, an increase in applied voltage results in an increase in velocity as electrons are promoted to and begin to increasingly populate the conduction band in the central valley. Further increases in voltage provides electrons with further energy and collisions in the central valley can cause electrons to enter one of the satellite valleys, which have lower mobilities than the central valley. As more and more electrons enter the satellite valley, the velocity of the overall conduction reduces (seen in Figure 4.11 (right)) [47], resulting in a reduction in current until, with yet

more applied voltage, all of the electrons enter the satellite valley and the velocity can then begin to increase with only the mobility of the satellite valley to affect this. It is the region where the current decreases with increasing voltage, known as negative differential resistance, which makes this diode useful.

This effect only relies on the bulk properties of the semiconductor and therefore the effect is known as bulk negative differential conductivity (BNDC) [47].

4.5 Esaki Diodes

An Esaki diode is a tunnelling diode made from semiconductor materials. As a result of the tunnelling mechanism it is very fast and is therefore discussed in more detail. The tunnel diode is a basic PN junction, but each side of the junction is very heavily doped, which results in a very narrow depletion region, the band diagram of which can be seen in Figure 4.12.

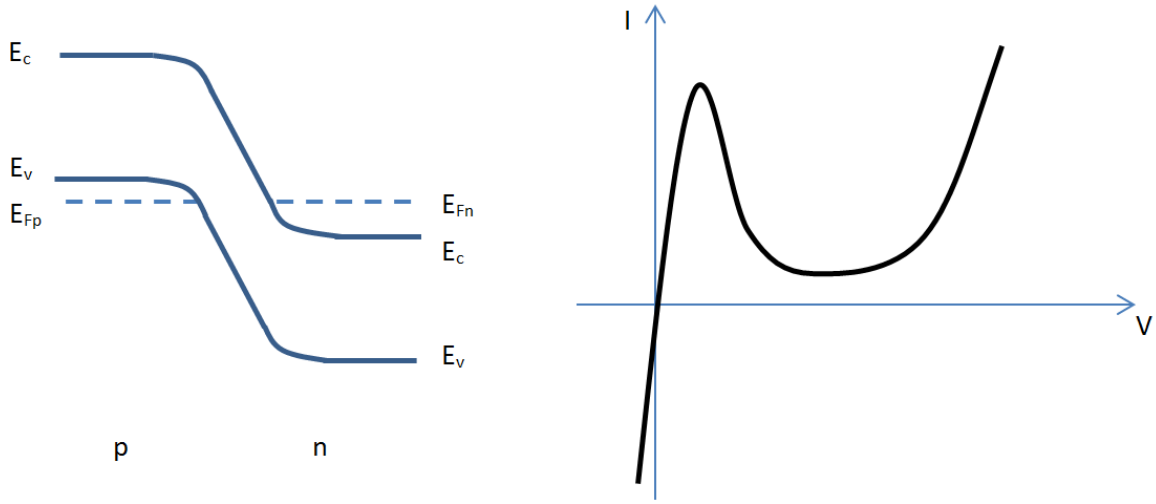

Figure 4.12 – *Esaki diode I-V characteristics (left) and Esaki band diagram at zero volts (right)*

This extreme doping causes the Fermi level to be between the valence band of the p-type side and the conduction band of the n-type side. Electron tunnelling is based upon the principle that nothing can be described with absolute precision - everything must be described by probabilities. Therefore, the application of bias raises the potential of the electrons, resulting in an increased probability of electrons existing

in the p-type material, resulting in a high current. As V is increased further, there are fewer unoccupied states on the p-type side, resulting in a decrease in current. The above effect results in an I-V characteristic shown in Figure 4.12 [47]. As can be seen, in the positive voltage region, the current initially rises rapidly to a point V_p, where the current then begins to decrease, causing a 'negative resistance' region. Further increase in applied voltage results in the presence of a diffusion current, and the I-V characteristics begin to appear similar to that of a standard PN junction.

4.6 Self-Switching Diodes (SSDs)

Another device of note is the self-switching diode (SSD). This diode is created using a single step process, by producing insulating trenches on a semiconductor [48]. The threshold voltage of an SSD can be tuned from zero upwards. A zero threshold would allow the detection of extremely weak signals, which would be appropriate in an energy recovery application. Furthermore, the simple architecture allows a very low parasitic capacitance, which is the primary speed limitation. With this minimised, very high switching speeds can be achieved.

The device is manufactured with two insulating grooves thus ensuring that the electrons have to pass that narrow channel between the two grooves in order to conduct a current between the left and right terminals. When a negative voltage is applied, negative charges near the trenches deplete the channel, restricting current flow. By contrast, when a positive voltage is applied, the positive charges near the trenches attract electrons to the channel, thus allowing current to flow [49]. Figure 4.13 shows a cross section of such a device [50].

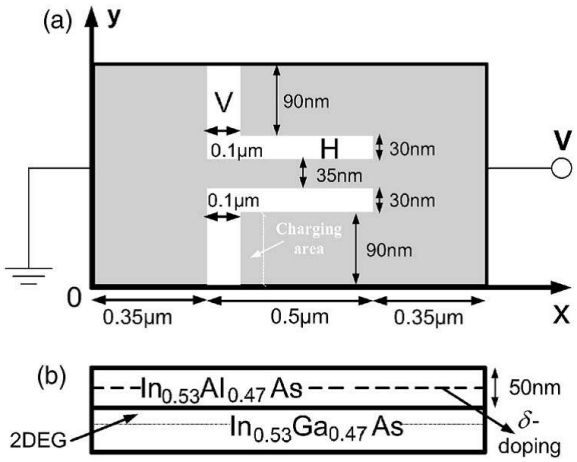

Figure 4.13 *– Top view (a) and cross section (b) of an example SSD (©AIP)*

A further advantage of these devices is that, unlike a number of other systems which require cryogenic cooling to operate in the terahertz frequency range, these devices can be operated at room temperature.

Simulations have shown that the rectified current and cut-off frequency of these devices can be improved by adjusting the shape and the dielectric material which is used to fill the insulating trenches [50]. Furthermore, the rectified current has been shown to change sign at frequencies higher than the cut-off, which could be an issue as, if the diode is not sufficiently highly rated for the resonant frequency of the antennas, it would act to provide a negative voltage rather than a positive one. Preventative measures could be taken to ensure that no harm is done, however, with signal diodes protecting equipment accordingly.

Experimentation has shown that the non-linearity of the device is sensitive to the dielectric constant of the material in the x direction trenches, but not to that in the y direction trenches (as seen in Figure 4.13). Furthermore, it was found that the frequency dependence of the output was dependent on the dielectric constant of the y axis trenches but not the x axis ones. Results by Xu *et al.* [50] determined that, in order to optimise this finding, the vertical trenches should contain a material with a low dielectric constant material, or be as wide as possible to reduce parasitic capacitances, which must be taken into account at high frequencies.

These devices have also been tested in arrays and have successfully rectified AC input signals, achieving a 16 mV output for a -10 dBm input [51]. They have also

been proven to function at 1.5 to 2.5 THz [52, 53].

4.7 MOM Diodes

Tunnelling is a desirable mechanism due to its speed. An alternative to the Esaki diode is the MOM diode. This structure involves a base metal, an insulator (usually in the form of an oxide) and finally a top metal. In order to make successful metal-oxide-metal (MOM) diodes for rectifying applications, the following must be considered:

- Maximise the work function difference between the metals for asymmetry in I-V characteristics [26],
- Produce a uniform oxide layer that is sufficiently thin (a few nm) for electron tunnelling to occur [32],
- Reduce diode size to sub-micron dimensions to increase the cut-off frequency, as seen in Equations 4.15 and 4.16.

$$f_c = \frac{1}{2\pi R_A C_D} \tag{4.15}$$

where

$$C_D = \frac{\varepsilon_0 \varepsilon_r A}{d} \tag{4.16}$$

and

f_c = Cut off frequency [Hz]
R_A = Antenna resistance [Ω]
C_D = Diode Capacitance [F]
ε_r = Relative permittivity
A = cross-sectional area of diode [m^2]
d = oxide thickness [m]

Metal-oxide-metal diodes used in the infrared range initially consisted of a thin metallic wire with an etched tip in weak contact with an oxidised surface [54] and

were known as point contact, or whisker, diodes. The structure of a point contact diode can be seen in Figure 4.14, with the blue base metal, green oxide and red point contact. Tungsten was commonly used for the point contact as it can be sharpened readily to provide the desired small area.

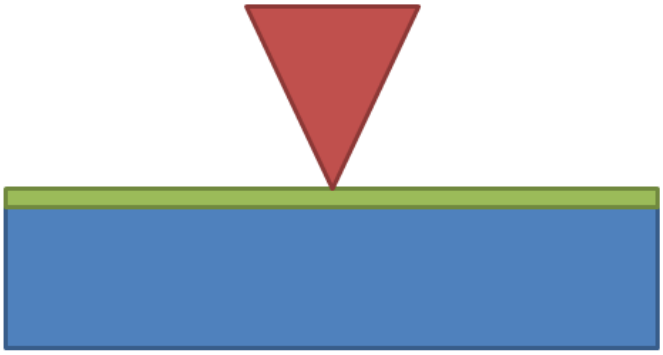

Figure 4.14 *– Schematic of a point contact diode*

The use of MOM diodes in the infrared is limited due to problems caused by the point-contact, which has a low mechanical stability and the sensitivity relies heavily on the contact area and oxide thickness [27]. As can be seen from Figure 4.14, although the tip of the contact could be thinned to make extremely low area devices at the point of contact with the substrate, the device would be very susceptible to damage due to the point contact, which is in weak contact with the surface. The aim is to replicate the good electrical results of the point contact diode but with a more stable structure.

A mechanical improvement to the point contact is the planar thin-film diode, which consists of two overlapping metal strips, separated by a thin oxide layer, as seen in Figure 4.15 [55]. These planar structures originally had a contact area approximately 100 times larger than point contacts, but the aim now is to minimise this area to reduce the capacitance from Equation 4.16.

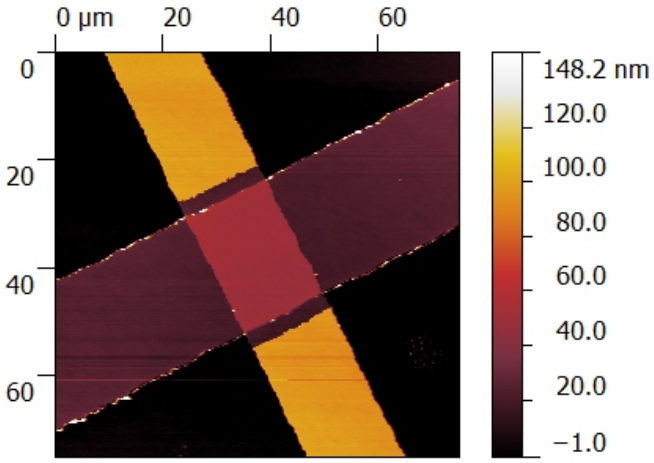

Figure 4.15 *– Planar MOM diode crossover*

One known material configuration is Ni-NiO-Ni for the structure [27], which should result in non-linear but symmetrical I-V characteristics. However, as discussed, asymmetry caused by differing metals is desirable for rectification [26]. With regards to varying the material choices, numerous material combinations have been used to maximise the work function difference, including W-Ni, Ti-Pt, Pt-W, Ni-Cr/Au and Al-Pt, which can be seen in Table 4.1. A common theme here is to choose one metal which oxidises readily and one which is inert and will not, with platinum and gold being commonplace in previously published works.

If the two metals are dissimilar then an intrinsic field exists within the insulator which results in asymmetry. However, this might not be the only reason for asymmetric conduction. For diodes which are fabricated using a base metal which oxidises readily, as the oxide is grown on the base metal surface the interface between the bottom metal/oxide layer and the top oxide/metal will be significantly different and so the surface states at the interface will be different which could contribute. This is less of a concern for diodes, which are fabricated with atomic layer deposition, for example. Furthermore, it is suggested that the dielectric constant of the oxide could vary throughout the oxide thickness, which affects the height and width of the barrier, thus again potentially affecting the asymmetry [39]. The diodes in Table 4.1 which are Ni-NiO-Ni diodes [27,56] still show AC rectification capabilities and therefore the metal variation cannot be the only reason for asymmetry.

In order to compare the diodes quantitatively, figures of merit are used. An often quoted figure of merit is the curvature coefficient (CC) [26, 57–59] (also referred to as the sensitivity [32, 56, 60] or the intrinsic current responsivity [61] which will be discussed in further detail in Section 5.4.1), sometimes multiplied by -1), which can be calculated as seen in Equation 4.17. The curvature coefficient is a measure of how non-linear a waveform is at a given point on an I-V curve.

$$CC = \left(\frac{\frac{d^2I}{dV^2}}{\frac{dI}{dV}} \right) \Bigg|_{V=V_b} = N_v R_v \tag{4.17}$$

where N_v is the non-linearity of the device, defined by Equation 4.18,

$$N_v = \frac{d^2I}{dV^2} \Bigg|_{V=V_b} \tag{4.18}$$

and the resistance at a given voltage V_b is given by Equation 4.19,

$$R_v = \left(\frac{dI}{dV} \right)^{-1} \Bigg|_{V=V_b} \tag{4.19}$$

This curvature coefficient can be calculated at any voltage required but is most useful at zero bias (CC_{ZB}) for recovery devices, which would not be biased when in operation. The resistance at zero volts cannot be directly extracted from experimental I-V results and therefore a polynomial fit is applied to the raw results and the zero bias resistance calculated thereafter. This is discussed in further detail in Section 5.4.1. As can be seen from Table 4.1, typical curvature coefficient values are all lower than $2\,\mathrm{V}^{-1}$.

Many of the diodes in Table 4.1 are small in area, with common dimensions being 50 to 100 nm in order that the diode can switch fast enough for the rectification of radiation [26, 62, 63]. This scale of diode can be produced via numerous techniques, however the most common is via e-beam writing which is a very slow, serial process. An ideal aim is to find a faster, more parallel process which would allow large areas of device to be produced quickly, such as contact or transfer printing. More techniques include angled evaporation, which allows diode devices to be produced in one process by angling a metal evaporation and then introducing oxygen to oxidise this metal. A further change of angle of the substrate in situ occurs before evaporation of the top

contact metal [58], resulting in a very small diode region using a one step process.

As can also be seen from Table 4.1, the diodes which have been AC tested all have very high operating frequencies, often at 28 THz, which is due to the fact that they are commonly being tested with CO_2 lasers. These existing diodes prove that the diodes can function at a sufficiently high frequency to detect infrared radiation. The diodes have also been tested in a much higher frequency range by [64], achieving an operating range of 120 to 180 THz for Pt-W diodes and 60 THz for Ti-Pt diodes.

Furthermore, various conduction mechanisms have been presented in other works for these devices, namely direct electron tunnelling, Schottky emission, Fowler-Nordheim tunnelling and Poole-Frenkel conduction [65, 66]. As previously discussed, direct electron tunnelling is desirable for this application. As discussed in Section 4.2.2, electrons in metals can travel through a high barrier. The probability of electrons passing through a potential barrier falls exponentially with its thickness. Therefore the oxide layer thickness should be minimised.

Fowler-Nordheim conduction is also an important mechanism to consider due to the tunnelling potential and inherent speed. In [67] the diodes are aluminium based and both direct electron tunnelling and Fowler-Nordheim tunnelling conduction occur. Fowler-Nordheim conduction has also been shown to occur in 3 to 6 nm thin film oxides [68] as well as a 4.5 nm oxide [40], which is within the expected thickness range, thus proving the relevance of Fowler-Nordheim as a potential mechanism. Variations on the Fowler-Nordheim theory have also been applied to flash memory, thus confirming the potential for a combination of mechanisms and variations from the standard approach [63].

Schottky barriers have also been formed in MOM diodes [69], and furthermore the mechanism can be investigated by analysing the first derivative of the I-V curve and determining the difference between the trough of this curve and the origin [70]. The distance of the minimum from the origin can determine whether a trap-based mechanism dominates. Schottky barriers have been very successful in other works, such as the $Ti/TiO_2/Pt$ diodes produced with a 19 nm oxide layer, and subsequent current ratios of $10^9 : 1$ [71].

As seen in Equation 4.15, in order to maximise cut off frequency, the capacitance of the device must be minimised. One means to achieve this is to minimise the relative permittivity of the oxide layer. As most MOM devices are fabricated using very thin oxides, the permittivity values vary from the expected bulk material properties [72]. Bessergenev *et al.* found the relative permittivities of various titanium oxides had values in the range 2.25 to 200 [73], while Zhou *et al.* found TiO_x to vary in the range 31.8 to 52.7 [74]. This is important for cut off frequency calculations, as both the area and relative permittivity determine the capacitance of the diodes, as seen in Equation 4.16. Using a unique oxidation method could result in an oxide which is unique to the process and equipment used, whereas a process such as ALD would ensure greater repeatability.

One alternative method that has been discovered, which improves the diode asymmetry, is to use a double insulator, i.e. an MIIM device with one low barrier insulator and one high barrier insulator, which have been shown to have superior I-V characteristics to single layer oxides [75, 76]. However, this double insulator will be thicker than an equivalent single insulator layer and will therefore reduce the current flow and may even prevent electron tunnelling completely.

Table 4.1 *– MOM diode summary*

Group	Metal Pair	Work Function Difference $[eV]$	Diode Area $[\mu m^2]$	Fabrication Process	Operating Frequency [THz]	CC_{ZB} $[V^{-1}]$
Fumeaux *et al.* (1998) [27]	Ni-Ni	0.00	0.0121	E-beam lithography	28	-
Abdel-Rahman *et al.* (2004) [56]	Ni-Ni	0.00	0.075	E-beam lithography	28	1.7(max)
Denisov *et al.* (2007) [64]	Pt-W	1.10	0.031	Point contact	120 to 180	-
Denisov *et al.* (2007) [64]	Ti-Pt	1.32	0.031	Point contact	60	-
Krishnan *et al.* (2008) [77]	Ni-Cr/Au	0.65	1.000	E-beam lithography	-	-
Tiwari *et al.* (2009) [78]	Al-Pt	1.37	0.004	E-beam lithography	28	-1.5
Huang *et al.* (2010) [69]	Ti-Pt	1.32	10000	Photolithography	-	-
Bean *et al.* (2011) [58]	Al-Pt	1.37	0.0056	Angled evaporation	-	1.7
Bareiß *et al.* (2011) [67, 79]	Al-Pt	1.37	0.010	E-beam lithography Transfer printing	-	-
Bareiß *et al.* (2012) [62]	Ti-Pt	1.32	0.005	Transfer printing	-	-
Kinzel *et al.* (2013) [80]	Al-Pt	1.37	0.008	E-beam lithography	28 (simulated)	1.2×10^{-3}

4.7.1 Oxide Layer Production

The area of primary importance in the fabrication focusses on the MOM diode oxide, ensuring that it is sufficiently thin and uniform such that a fast, preferably tunnelling, mechanism occurs in each device repeatability. There are two main ways to produce this layer: growth and deposition. In the case of refractory metals, an oxide can be grown on the base metal layer or, alternatively, regardless of metal choice, an oxide layer can be deposited via e-beam evaporation, atomic layer deposition or sputtering for example. The different techniques must be considered and the most appropriate one chosen for this application. There are methods available for comparing the quality of oxide layers produced, as well as the conduction mechanism analysis. For example, monitoring $\frac{dI}{dV}$, which is the conductance of the diode, and the point at which the minimum of this graph occurs relative to the origin provides a measure of the number of defects in the oxide structure which can then be altered as appropriate via the oxidation method [70].

Deposition is a very attractive option with regards to producing an oxide film on a surface, as it means that the deposited layer does not have to be related to the material underneath, thus providing significant flexibility in production. However, due to the nature of some deposition techniques, the layer can often be non-continuous and rough. This is dependent on the desired thickness. Consider a layer where the oxide forms small islands of materials which eventually coalesce; if the thickness is greater than that required for coalescence then the process is not significant. However, for layers which are sufficiently thin, it is unlikely that a uniform layer could be produced in this manner. For example, a 8 nm thick TiO_2 oxide layer has been deposited via e-beam evaporation which has good asymmetrical I-V characteristics [69]. Conversely, a NiO film deposited by DC reactive magnetron sputtering in oxygen and argon produced a polycrystalline structure oxide of thickness 3 to 5 nm which would be sufficiently thin for our intended application, although no roughness or defect data was presented [81].

One possible technique to produce very thin layers is Atomic Layer Deposition (ALD), which allows uniform deposition of a wide range of materials and chosen dielectric constants down to thicknesses less than 5 nm in a repeatable way. Pt-TiO_2-

Ti diodes have been produced in this manner, with a 19 nm thick oxide, resulting in a current ratio of 1 billion when tested at 250 °C [71]. This example has a much thicker oxide that required here, however, ALD can be used to produce oxides which are less than 5 nm thick and uniform, which would be ideal.

Oxide growth can take place on a refractory metal, which when exposed to particular conditions will grow a native oxide on its surface. This can be a convenient method of obtaining an oxide but it also has drawbacks. The oxide grown in this manner is entirely dependent on the metal it is grown on. Some metals, such as aluminium or titanium, will immediately form a thin (a few nanometres) native oxide when in the presence of air, whereas others, such as nickel, will form a native oxide but more slowly. Furthermore, the boundary between a metal and its native oxide will be less abrupt than the boundary caused when an oxide is deposited on a material, which may be an important consideration with regards to physical and electrical analysis.

The two most common methods of oxide growth are exposure of the metal to elevated temperature environments, i.e. furnace oxidation, and also plasma oxidation. Both of these processes accelerate the desire of the metal to form an oxide, by providing elevated oxygen and energy conditions to encourage this to occur. Also, it is important to note that plasma oxidation can vary the produced oxide thickness as a function not of time but rather the plasma power [82] and the gas concentration of the plasma can also alter the electrical characteristics of MOM diodes [83]. By combining the oxygen with an inert gas, such as argon, the effect of the plasma on the metal can be reduced in intensity.

Comparisons between native growth and plasma growth have also taken place [84], with the plasma oxidised diodes having a higher current density than their furnace oxidised counterparts. Investigation has also taken place into the effects of substrate and oxidation temperature on the furnace oxidation of titanium [85], where TiO, anatase and rutile forms of titanium oxide can be produced by varying the oxidation temperature, thus allowing more control over the structure and crystallinity of the fabricated oxide layer.

As well as successfully altering the deposition or growth of an oxide layer, it is

possible to alter an existing layer to have more desirable features. The main method for this is annealing. Annealing can be used to remove defects in oxide layers [86], to alter the stoichiometry [87], or to alter the roughness [69] to name a few of the effects. The electrical performance of a MOM diode can be altered as a function of annealing temperature in various metals including nickel [88] and zinc [89]. Argon sputtering can be used to alter an existing oxide via the stoichiometry, as seen in [87], where TiO_2 was converted to Ti_2O_3 and TiO.

Furthermore, annealing can also be used to alter the devices and their associated conduction mechanisms [69]. In [90], Fowler-Nordheim conduction in GaN diodes was converted to Poole-Frenkel conduction via exposure to hydrogen, due to hydrogen's ability to alter the charge at the MIS interface thus changing the barrier height.

Annealing can take place using two main methods, thermal annealing which takes place during the fabrication process, and electrical annealing which takes place during the testing phase. Huang *et al.* [69] noted bubbling and an increase in roughness caused by electrical annealing.

4.7.2 Manufacturing Considerations

The oxide layer production is of primary importance. However, there are two other main difficulties involved in the manufacture of these diodes namely the level of technology to ensure that the device cross sectional area is minimised as well as the precautions required due to the fact that the devices are highly sensitive to electrostatic discharges. Furthermore, these diodes have been proven to work at room temperature, whereas for our purposes they will have to operate at much higher temperatures: the possibility of this and the side effects of such a high temperature on the diode must be investigated further.

E-beam writing is a serial process whereby a beam of electrons is used typically to expose photoresist, which can then be subsequently processed as appropriate. This can result in features which are sufficiently small for this application, with features typically 10 nm wide but they can be as small as 2 nm [91]. Unfortunately, it is a very slow process and therefore large areas of small features would take a significant

period of time. As a result, for large scale processing, an alternative method must be found.

Nano-Imprint Lithography is a sub-micron copying process which uses transparent PDMS stamps, which have been produced from e-beam written master stamps. Once the NIL stamp has been made it allows repetitive production of features over a large area. The NIL process can be seen in Figure 4.16. The substrate (grey) is first coated with photoresist (yellow), the NIL stamp (seen in white) is then brought into controlled contact with the photoresist and substrate, forcing it to conform to the stamp shape. The entire system is then exposed to UV light (blue), which will cure the photoresist so that when the stamp is removed, the photoresist is the inverted shape of the stamp. Dry processes such as reactive ion etching (RIE) can then be used to thin the photoresist so that it only remains on certain regions of the substrate and subsequent metallisation can then take place.

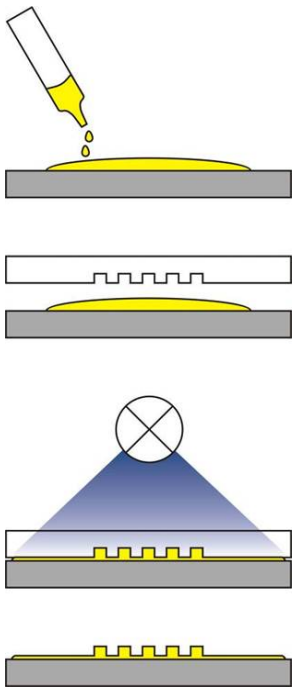

Figure 4.16 – *The nano-imprint lithography process (courtesy of Dr Mark Rosamond)*

As stated the main issue with this process is the production of the initial stamp as it still requires a slow process. However, one time consuming process producing a hard stamp is worthwhile if a number of soft stamps can be produced easily and then

each of those can be used numerous times, thus reducing the effect of the delay per device batch. Other variations of NIL are possible, such as hot embossing. However, as the above UV-based NIL process is the one available this would be the process of interest.

Roll-to-roll (R2R) processing is an alternative large scale processing technique which would allow high volume production of a rectenna array on a flexible substrate, as conceptualised in Figure 4.17, which shows a flexible wrap produced via a combination of NIL and R2R.

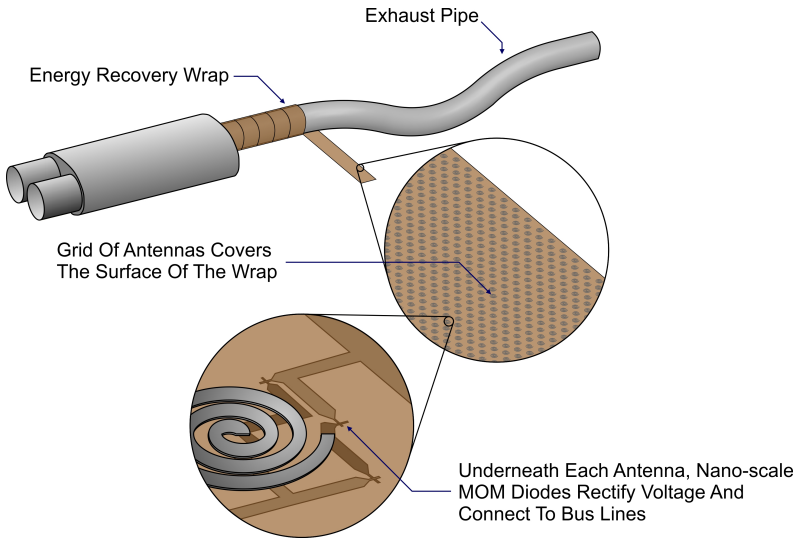

Figure 4.17 – *Conceptualisation of exhaust pipe wrap (courtesy of Dr Fred Hamlin)*

The aim would be to produce a narrow 'tape' of rectenna devices via multiple passes in a roll-to-roll device to produce the multiple layers needed for a rectenna device, the production speed for which is described in Table 4.2.

Table 4.2 – *Production Speed Summary*

Technology	Write Speed	Time/Device (s)	Time/Wrap (s)
E-beam writing	4" diameter wafer in 15 min [92]	1.1×10^{-7}	93500
NIL and R2R	$3\,\mathrm{m\,min^{-1}}$ [93]	4.0×10^{-10}	340

Table 4.2 assumes a total device area of 1 µm^2, feature size 100 nm, an exhaust length of 4.5 m, with a diameter of 6 cm, and therefore a cross-sectional area of 0.85 m^2 which equates to approximately 8.5×10^{11} devices and a wrap width of 5 cm.

For e-beam writing, a 4 inch diameter wafer has a radius of 0.0508 m, and therefore an area of 8.1×10^{-3} m^2. This equates to 8.1×10^9 devices per wafer. Given a rate of 1 wafer every 15 minutes, it would take 1.11×10^{-7} s per device production time. If this is then expanded to produce the total number of devices for a wrap, which is 8.5×10^{11}, it would take 93 500 s to produce one wrap's worth of devices. The same calculations can be used to produce the values seen in Table 4.2 for NIL and R2R.

As can be seen R2R and NIL offer approximately a 2.5 order of magnitude increase in potential production speed, compared to e-beam writing each device. Similar transfer printing techniques have already been used to produce MOM diodes using stamps [62, 67, 79].

4.8 Summary of Conduction Mechanisms

Figure 4.18 shows the energy band structure of a Ti/TiO_x/Pt diode, showing both the unbiased (a) and biased (b) forms. In the formation of this junction, the Fermi levels of the metals align, causing the trapezoidal oxide energy band, due to the work function difference between the two metals (5.65 eV for platinum, and 4.33 eV for titanium [94]). A voltage, V, applied to the titanium, causes a difference in Fermi levels between the two metals. The difference in field is equal to $\frac{V}{d}$ in addition to the existing electric field in the barrier. This can then result in various conduction mechanisms through the barrier, as summarised in Figure 4.19.

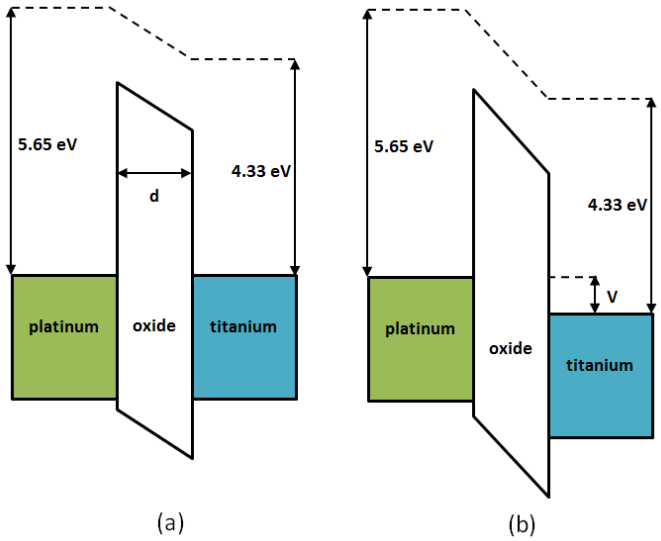

Figure 4.18 – *A $Ti/TiO_x/Pt$ junction - (a) unbiased, (b) biased*

Figure 4.19 shows a pictorial summary of the conduction mechanisms discussed [95], with Table 4.3 detailing the equations for each mechanism with information on the best plots used in order to obtain a straight line with gradient and intercept also specified. As can be seen from Figure 4.19, Schottky conduction involves acquiring enough energy to overcome the oxide barrier (a), Poole-Frenkel conduction involves electron movement between traps in the oxide (b), Fowler-Nordheim conduction involves electron tunnelling to the conduction band of the central oxide layer followed by conduction band transport to the other side (c), trap assisted tunnelling involves transport through the barrier via traps within the oxide (d), whereas direct electron tunnelling involves electron transport from one conduction band to the other directly through the barrier (e) [29].

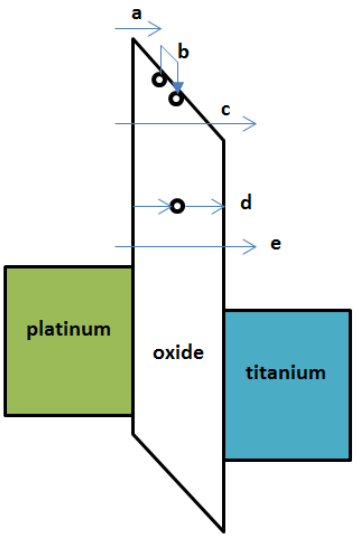

Figure 4.19 – *Conduction mechanisms comparison - (a) Schottky conduction, (b) Poole-Frenkel conduction, (c) Fowler-Nordheim tunnelling, (d) trap-assisted tunnelling, (e) direct electron tunnelling*

Table 4.3 – *Conduction mechanism summary table*

Mechanism	Equation	Graph to Plot	Gradient	Intercept
Schottky Emission (voltage dependence)	$J = A^*T^2 exp\left\{\frac{e\left(\beta V^{\frac{1}{2}} - \phi_{bn}\right)}{kT}\right\}$	$ln\ \frac{J}{T^2}$ versus $V^{\frac{1}{2}}$	$\frac{e\beta}{kT}$	$ln\ A^* - \frac{e\phi_{bn}}{kT}$
Schottky Emission (temp. dependence)	where $\beta = \left(\frac{e}{4\pi d\varepsilon_0\varepsilon_r}\right)^{\frac{1}{2}}$	$ln\ \frac{J}{T^2}$ versus $\frac{1}{kT}$	$e\left(\beta V^{\frac{1}{2}} - \phi_{bn}\right)$	$ln\ A^*$
Poole-Frenkel Conduction (voltage dependence)	$J = \frac{eN_c\mu_e V}{d} exp\left\{\frac{e\left(\beta_{PF} V^{\frac{1}{2}} - \phi_{bn}\right)}{kT}\right\}$	$ln\ \frac{J}{V}$ versus $V^{\frac{1}{2}}$	$\frac{e\beta_{PF}}{kT}$	$-\frac{e\phi_{bn}}{kT} + ln\ \left(\frac{eN_c\mu_e}{d}\right)$
Poole Frenkel Conduction (temp. dependence)	where $\beta_{PF} = \left(\frac{e}{\pi d\varepsilon_0\varepsilon_r}\right)^{\frac{1}{2}}$	$ln\ J$ versus $\frac{1}{kT}$	$e\left(\beta V^{\frac{1}{2}} - \phi_{bn}\right)$	$ln\ V$
Fowler-Nordheim tunnelling (voltage dependence)	$J = \frac{em_m V^2}{8\pi h\phi_{bn} m_{ox} d^2} exp\left\{-\frac{4d(2m_{ox})^{\frac{1}{2}}}{3e\hbar V}\left(e\phi_{bn}\right)^{\frac{3}{2}}\right\}$	$ln\ \frac{J}{V^2}$ versus $\frac{1}{V}$	$-\frac{4d(2m_{ox})^{\frac{1}{2}}}{3e\hbar}\left(e\phi_{bn}\right)^{\frac{3}{2}}$	$ln\ \frac{e^2 m_m}{8\pi he\phi_{bn} m_{ox} d^2}$
Direct Electron Tunnelling (voltage dependence)	$J = \frac{em^* V^2}{8\pi h\phi_{bn} m_{ox} d^2\left[1-\left(1-\frac{V}{\phi_{bn}}\right)^{1/2}\right]^2}$ $exp\left\{-\frac{4d(2m_{ox})^{\frac{1}{2}}}{3e\hbar V}\left[\left(e\phi_{bn}\right)^{\frac{3}{2}} - \left(e\phi_{bn} - eV\right)^{\frac{3}{2}}\right]\right\}$	$ln\frac{J}{V^2}$ versus $\frac{1}{V}$		
Trap Assisted Tunnelling (voltage dependence)	$J = e\int_0^d \frac{N_T(x)}{\tau_c(x)+\tau_e(x)}\,dx$			
Hopping Conduction (voltage dependence)	$J = \frac{e^2 n^* \alpha^2 V}{kTd\tau_0} exp\left\{-\frac{4\pi m^* \phi_m \alpha}{h}\right\}$			

4.9 Summary of Existing Diodes

Table 4.4 summarises each of the existing diodes discussed in this chapter. As can be seen, of these diodes Schottky, self-switching diodes, and MOM diodes have been shown to work in excess of 1 THz.

Table 4.4 – *Diode summary*

Diode Type	Advantages	Disadvantages	Operating Frequency
Schottky	Established Device	Semiconductor based and too slow	2 THz [96]
IMPATT	High frequency	Generates signals rather than sensing them	80 to 110 GHz [97]
Gunn	High frequency	Needs biasing	164 GHz [98]
Self-Switching	High frequency and very small	Must be on high mobility substrate (not flexible)	2.5 THz [53]
Point Contact MOM	High frequency tunnelling diode	Too Fragile	30 to 130 THz [99]
Planar MOM	High frequency tunnelling diode	Must be small to be fast	28 to 180 THz [27, 56, 64]

Of these diodes, Schottky diodes are not suitable as they are not sufficiently fast and they require a bias in order for significant conduction to occur as the electrons must overcome the central barrier. Self-switching diodes operate at a similar speed but they must be on high mobility semiconductor substrates (such as GaAs), which are not flexible. Furthermore, the feature sizes associated with these devices is significantly smaller than the fabrication limits of most fabrication plants. Therefore, MOM diodes are the most suitable. However, there is now a compromise between size and structural stability. It is easy to create a point contact which has a small area but this is not very stable. By contrast, planar devices are much more

stable but more consideration must take place when fabricating the overlap region to minimise area.

4.10 Diode Theory Conclusions

There are many different diodes, which are used in high frequency applications, including Schottky Diodes, IMPATT, Gunn, self-switching diodes, point contact MOM diodes and planar MOM diodes. All of which have been discussed and compared here, including their suitability for high speed energy recovery purposes. Of these, planar metal-oxide-metal diodes were chosen as a suitable diode structure, due to a combination of their ability to rectify high speed signals (they have been shown to work at frequencies up to 180 THz), as well as their mechanical stability compared to the point contact MOM diode. The main challenge with this diode is to produce a thin uniform oxide layer through which direct electron tunnelling can occur. Furthermore, the manufacturing process must be able to fabricate devices, which are sufficiently small to work at the required frequencies, and sufficiently fast so that large numbers of devices can be fabricated in as small a time as possible to accommodate the large number of devices needed for large area coverage. Currently, roll to roll processing could be a suitable option for large scale processing of these devices into large area arrays.

With the chosen device decided upon, the individual devices must be fabricated and tested using the figures of merit discussed, the processes for which are discussed in Chapter 5.

Chapter 5

Fabrication and Analysis Techniques

5.1 Introduction

In order to perform a full characterisation of the diodes produced, various analysis techniques are needed to quantify each diode for comparison and improvement. This chapter discusses selected techniques in more detail, which will be referred to in subsequent chapters. The I-V analysis, which used a 9th order polynomial to help determine common figures of merit, is discussed. The HP4145B and accompanying C program as well as the SMU and VNA Matlab programs are described. Analysis of the cryostat, ToFSIMS, TEM and EBIC data is explained with typical examples to help explain the analysis process.

The desired structure of the diode can be seen in Figure 5.1. It involves despositing a patterned base layer of metal on a substrate, followed by an oxide which can either be desposited or grown on the metal, followed by a final patterned metal layer being added to complete the structure.

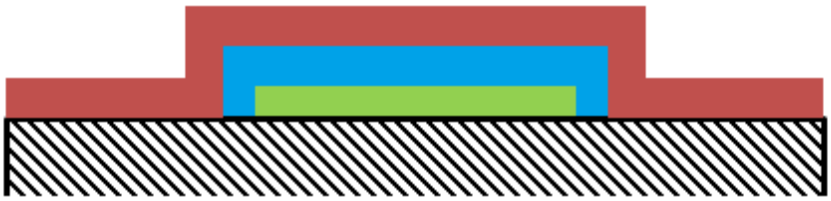

Figure 5.1 *– MOM diode structure - base metal (green), oxide layer (blue) and top metal layer (red)*

The main fabrication issues with this structure are the thin oxide layer and the small patterned features. The fabrication and analysis techniques focus on trying to ensure that these issues are analysed and addressed.

5.2 Fabrication

Specific information regarding the fabrication process route is discussed in the appropriate chapter for each process run, however, general discussion of the main equipment used in the various processes is described here.

5.2.1 Photolithography

The main photolithographic process used in this project is a bi-layer lift-off technique as it is a metal independent process, meaning that the same process can be used regardless of which metal is required, which is beneficial when metal choice may vary between fabrication steps or between batches of samples. The bi-layer process involves spinning and baking SF9 (typical thickness 0.5 µm [100]) and then Microposit SPR 350 1.2 (typical thickness 1.2 µm [101]), with the aim to achieve a T-step profile after development has occurred, as seen in Figure 5.2. This is so that, when metal is deposited from above, a discontinuous film is deposited, such that when the photoresist, and hence excess metal, is removed, the remaining metal has a clean profile.

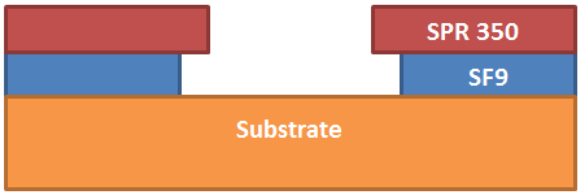

Figure 5.2 *– Photoresist T-profile - substrate (orange), SF9 (blue) and SPR 350 (red)*

Both photoresist chemicals were deposited on the substrate surface via spinning using Laurell spinners. This ensures a repeatable thickness of photoresist is applied on each run, and that the thickness of the photoresist is known, as a result of supplied thickness vs spin speed graphs [100, 101]. After each spinning process the substrates were baked using hot plates.

In order to pattern the substrates, dark field masks were used. Due to the positive nature of the SPR350, any regions, which were transparent would be developed away after exposure to UV light and therefore these transparent regions relate to where metal would be deposited. In this manner several metal layers can be deposited to form multi-layer structures. An EVG 620 mask aligner was used to expose the substrates to UV light, changing the photoresist, which has been exposed such that it is developed away in the subsequent development process. It is worth noting that the SF9 is not used as a photoreactive chemical in this process, but rather because of its superior development rate in MF-319 compared to the SPR 350, which results in the desired T-profile previously discussed.

5.2.2 Metallisation

Once the substrates had been patterned via photolithography, they had to be coated with metal. This took place via electron beam (or e-beam) deposition. This involves high energy electrons being directed towards a crucible of metal to heat it up until it melts and evaporates. The resulting vapour is then deposited on the substrates which are placed upside down at the top of the chamber. This process is very directional, which is favourable for lift-off processes as it means a discontinuous film at the photoresist-clear region interface. Sputtering is a common metal deposition

technique but it is much less directional than e-beam evaporation due to the larger number of collisions between particles within the chamber caused by the higher pressures during a sputtering process, compared to the high vacuum conditions of e-beam evaporation. All metals were therefore deposited using e-beam evaporation. Unfortunately, the compromise with this choice included less uniformity and less control over adhesion due to stress, which is a particular issue with the deposition of platinum.

The platinum in particular was very challenging to deposit using e-beam deposition due to its high melting point. The power involved in evaporating platinum is approximately double that of titanium, at which point thermal stress effects had to be considered. In order to reduce the stress in the deposited film, the chamber had to be allowed to heat up so that the substrates became hot prior to the deposition beginning. This had adverse effects on the deposited platinum profile, with the edges of the metal often being very rough and which often turn up slightly, as can be seen in Figure 5.3, which shows the side profile of a MOM diode, with titanium and titanium oxide visible from the left and platinum overlapping it from the right, with the left edge of the platinum curling up. Furthermore, in order to reduce the film stress, the samples were left to cool slowly at low pressure prior to being removed from the e-beam equipment.

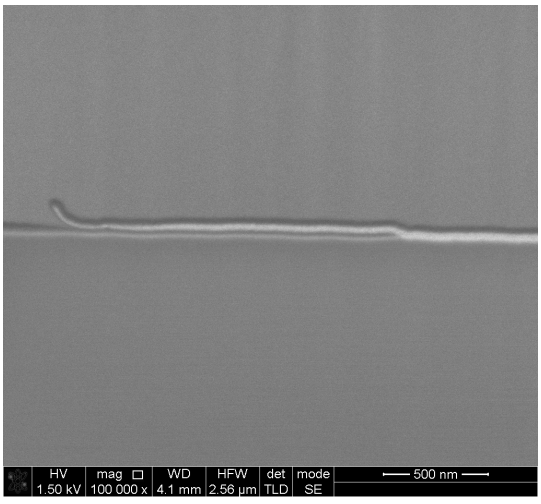

Figure 5.3 *– FIB image of cross section of diode structure - central region shows the diode crossover with titanium (from left), titanium oxide (between layers) and platinum (from right). The platinum can be seen curving up at the edge due to the lift-off process*

5.3 Phase Shift Lithography

In order to maximise the cut-off frequency of the diodes, their cross-sectional area must be minimised. E-beam lithography is slow and expensive; NIL is good but still needs an expensive master. A novel technique is needed and phase shift lithography offers some potential advantages. Standard phase shift masks are expensive but Rogers et al. [102] came up with a technique which uses PDMS as phase shift masks. This technique has not been used a great deal in applications, but could be an ideal cost effective technique. The process development is discussed here, including the underexposure photoresist characteristic inversion used to provide lift-off capabilities using positive photoresist.

5.3.1 E-Beam Writing and Nanoimprint Lithography

Nano-imprint lithography (or NIL) is a sub-micron copying process, which uses PDMS stamps and UV curing of the photoresist to transfer the patterns onto the substrate. The quality of the nano-imprint master stamp is key to good feature definition. In-house stamp fabrication is preferred due to the lower cost and greater flexibility to change designs. However, a standard method of sub-micron feature production is through the use of e-beam writing, whereby every feature is created using a focussed beam of electrons. Depending on the feature density, this could take a significant amount of time and thus be expensive. As a result, a novel technique is required to produce sub-micron features over larger areas, and, therefore, phase shift lithography was investigated.

5.3.2 Phase Shift Lithography Diodes

Work by Rogers et al. [102] describes the production of feature sizes in the region of 90 nm using an elastomeric phase mask and incoherent, polychromatic ultraviolet light. Phase masks add a phase element to masks which would usually just provide binary amplitude information. By altering the phase shift of the light to an odd multiple of π, the result is an intensity of zero at every edge, where the two phases of light interfere destructively, as seen in Figure 5.4 [103]. The profile of a phase shift

mask can be seen, with the theoretical intensity profile below (a) and the resultant photoresist patterns which result from such a phase mask; positive photoresist (b) and negative photoresist (c).

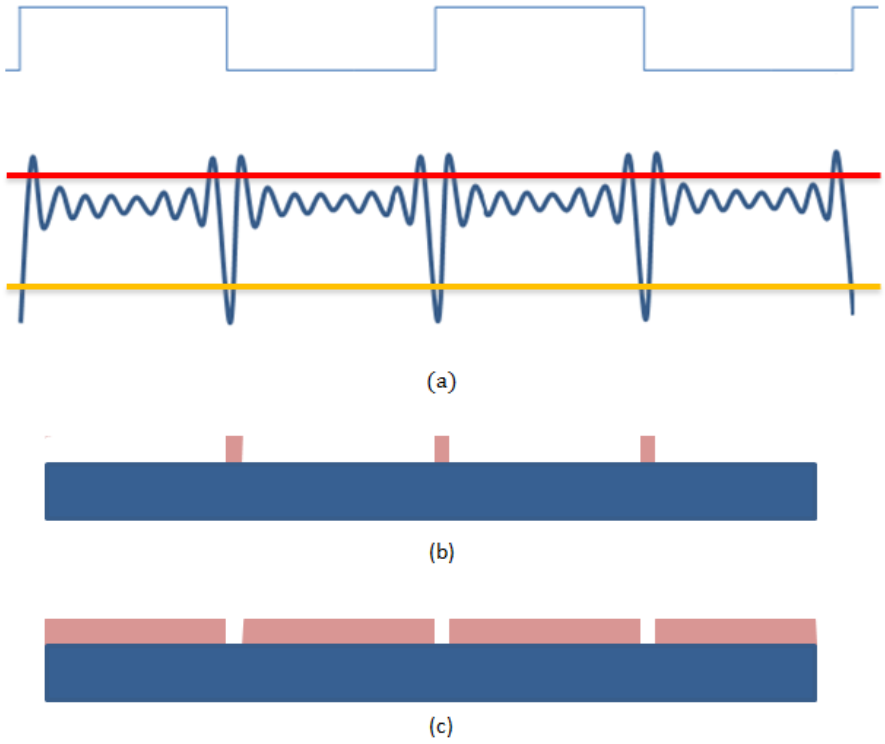

Figure 5.4 *– PSL process - (a) the profile of a phase shift mask, with the theoretical intensity profile below, the resultant photoresist patterns from said mask for (b) positive photoresist and (c) negative photoresist*

When using positive photoresist in the standard way it would be exposed, and the intensity of light incident on the substrate would be equivalent to the orange line seen in Figure 5.4. However, in the intensity profile either side of the phase shifted void regions, there are two intensity peaks (intersecting the red line). By underexposing the photoresist, these lines can be used to provide an inversion of the resultant photoresist pattern after development. As a result, positive photoresist can be used in an inversion technique to provide a suitable polarity profile for subsequent lift-off techniques, resulting in a process which is not dependent on metal choice. The red and orange horizontal lines in Figure 5.4 refer to the boundary at which the photoresist has received sufficient light to be removed during development. With regards to the positive photoresist, intensities below the line result in insufficient

light intensity to remove the resist. Moreover, the further below the line the less likely the photoresist will be partially developed, resulting in a photoresist profile which would mirror the intensity profile.

From the theoretical phase intensity profile in Figure 5.4, it could be expected that when using positive photoresist in the low intensity inversion regime, two lines would be present for each phase transition. However, this is not the case; as can be seen in Figure 5.5, there is an inherent asymmetry in the magnitude of the intensity for each of the high and low regions on the stamp.

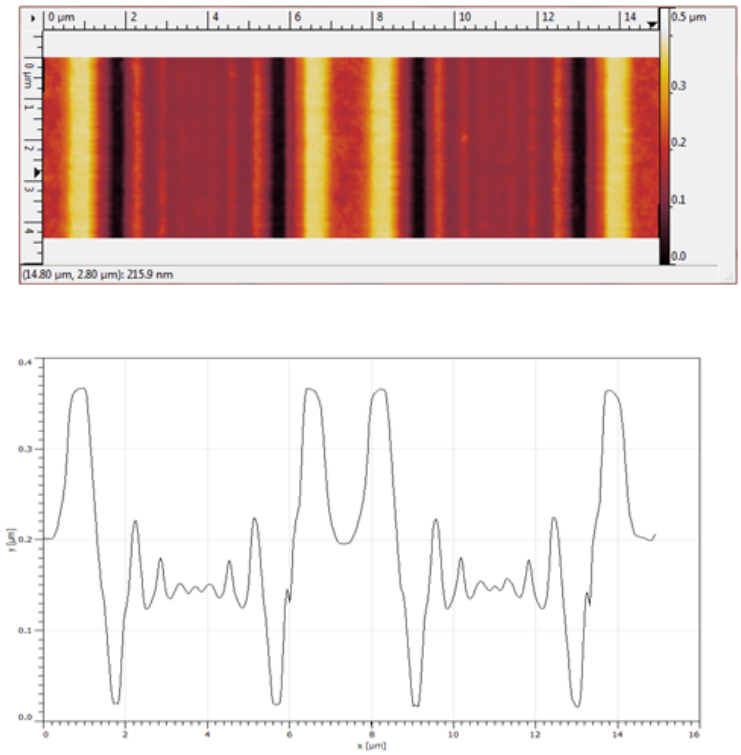

Figure 5.5 *– PSL AFM profile in SPR-350 dilute photoresist - (top) AFM image (bottom) a line profile from said AFM image*

Figure 5.5 shows an AFM image and line profile for this image of positive photoresist being used in the low intensity regime. There are two potential reasons for this asymmetry: the distance between consecutive features, in that if they are too close together then the same distance would result in the intensity being affected in the way shown. Alternatively, the profile could be due to the effect of the PDMS not being entirely transparent to the UV light used, resulting in thicker PDMS regions being exposed to less light that the thin regions, and asymmetry occurring

as a result.

5.3.3 Diode Fabrication

Creating a Master Stamp

In order to produce a phase stamp, an N-type ⟨100⟩ silicon of 10 to 30 Ω cm resistivity was chosen as the substrate material (2" diameter wafers) and was oxidised in a 1100 °C oxygen rich furnace for 100 minutes to provide an insulating 45 nm film, which was confirmed using ellipsometry. Using standard lithographic techniques, a pattern was then transferred onto the substrate in SPR-350 photoresist using an EVG 620 mask aligner. An Oxford Instruments combined plasma etch/reactive ion etch (PE/RIE) system was then used to etch this pattern into the silicon dioxide layer, thus providing a three dimensional 'stamp'. PDMS (Sylgard 184, 6:1 ratio) was then cast onto the patterned SiO_2 substrate and cured for 2 days at ambient temperature (to prevent wrinkling) to form an elastomeric stamp which is transparent to near-UV. The depth of the features (also known as surface relief) was calculated for the average wavelength of the UV light used for exposure (330 to 460 nm).

Creating Sub-Micron Features in Photoresist

Microposit SPR-350 photoresist, diluted to a 50 % concentration with EC solvent, was spun on a glass substrate (approximately 400 nm thick) and the PDMS mask brought into conformal contact with the surface. Exposure to a low dose of 0.8 s of UV light using the EVG 620 mask aligner, followed by a 45 s post exposure bake and 20 to 25 s development results in narrow 'trough' regions in the photoresist at every point where a height transition has occurred in the PDMS stamp.

In order to ensure that all of the photoresist was fully removed in the trench regions, the PE/RIE system was used to etch away any unwanted photoresist (100 % O_2 50 mT, 70 W for 10 s, RIE mode), the results of which can be seen in Figure 5.6.

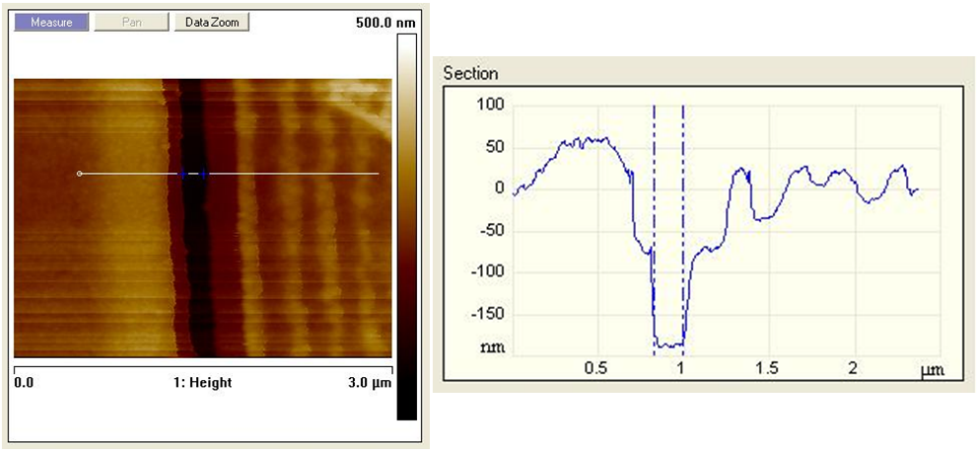

Figure 5.6 – *AFM of phase shift line in photoresist after a plasma etch*

Application of Phase Shift Lithography to the Diode Production Process

The bi-layer lift-off process described in Section 6.2.1 was used to deposit 25 nm titanium and 50 nm gold contact pads. The resulting pattern includes all contact pads and a common connection for final testing, as seen in Figure 5.7 (a) and (b).

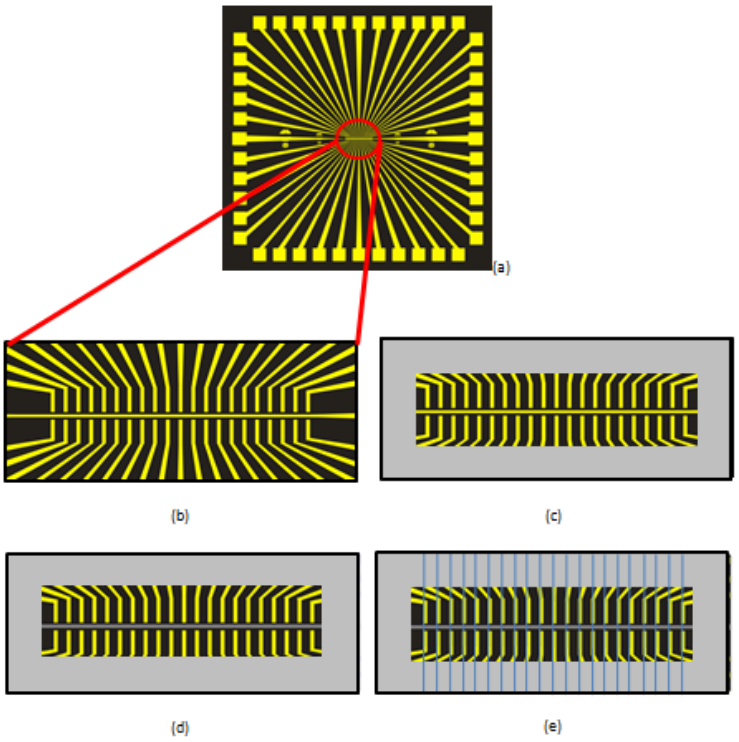

Figure 5.7 – *Phase shift lithography process - (a) the layout of a single diode connection module, (b) a close-up of the connection pads, (c) the connection pads left exposed after a chromium deposition, (d) the common connection after the gold has been removed, and (e) the phase shifted lines on top of the connectors*

The lift-off process was repeated twice; first with a design which allows all but the contact pad region to be coated with a thin layer of chromium (c), and secondly with a wide crossover mask design, which leaves only the common connection exposed. An etchant (4:1:8 KI:I_2:H_2O) was used to remove the uncovered gold and to undercut the photoresist, leaving a region of titanium exposed on the common connection (d). The samples were then placed in an ultrasonic bath in water for 10 seconds to help remove any remaining gold etchant solution. The exposed titanium was then oxidised using one of the methods described in Chapters 6 and 7. The phase shifting process described in Section 5.3.3 was then used to provide sub-micron vertical troughs in photoresist and 30 nm of platinum was then evaporated, resulting in a small Ti/TiO_x/Pt region being produced. Finally, the chromium was removed, which also removed unwanted platinum, completing the diode fabrication process.

Some initial diodes were produced with the phase shifted lines being used as the bottom titanium diode connection. In this process, the titanium/gold contact pads were produced first, without a common connection. Phase shifted lines were then produced on top of these contact, and finally a common platinum connection was added, crossing the phase shifted lines.

5.4 Electrical Analysis

5.4.1 I-V Analysis

A Cascade RF/DC manual probe station with two triaxial probes was used in the measurement of the I-V characteristics of each diode. The probes were connected to an HP4145B parameter analyser, which was controlled remotely using a custom program written in C, which allows the data to be retrieved and stored separately. The diodes were tested over different voltage ranges up to ± 0.5 V, and at different resolutions down to 1 mV, with the results being dependent on both of these parameters. Later diodes were instead tested using an Agilent B2902A Source and Measurement unit, which was controlled via a custom Matlab program.

In order to successfully analyse the I-V data, a polynomial fit was made to each diode result, which could then be manipulated to provide quantitative results. The

fit made to the plot, to obtain the results in subsequent figures, has used a 9th order polynomial. Others have restricted their analysis to a 5th order fit [26], which in our experience does not follow the data as clearly, particularly in the crucial area around 0 V. The resistance is obtained from $(dI/dV)^{-1}$ of the diode characteristic, and the often quoted figure of merit for these diodes, the curvature coefficient (CC), is calculated by multiplying the second derivative (d^2I/dV^2) by the resistance.

Table 5.1 shows the result, from the same diode I-V data, of using different order polynomials to determine the curvature coefficient at 0 V (CC_{ZB}). With regards to the accuracy of the polynomial fit, the resolution of the data was also very important.

Table 5.1 *– Zero bias curvature coefficients for different order polynomial analysis*

Polynomial Order	Curvature Coefficient at 0 V (V^{-1})
5	20.5
7	9.5
9	5.5

Therefore, given the large voltage range over which the devices were tested (±0.3 V for some diodes), the more complicated I-V waveform recorded as a result (more opportunity for turning points over a larger range), as well as the improved adj. R^2 value, a 9th order polynomial was used to analyse the results. A 9th order polynomial fit was the highest fit available using OriginLabs software, compared to the 5th order maximum in Microsoft Excel. As can be seen from Table 5.1 lower order polynomial fits tend to give more impressive curvature coefficients, with more conservative results being obtained using a higher order polynomial. One argument for alternative analysis would be to measure the I-V characteristics over a lower voltage range and subsequently use a lower order polynomial fit, or test a range of polynomial fits and determine the most suitable fit based on the adj. R^2 value.

As a result of this, it is common in a lower voltage regime to use a Taylor series

expansion to approximate the I-V characteristic, as seen in Equation 5.1

$$I = \frac{dI}{dV}V + \frac{1}{2!}\frac{d^2I}{dV^2}V^2 + \frac{1}{3!}\frac{d^3I}{dV^3}V^3 + \frac{1}{4!}\frac{d^4I}{dV^4}V^4 + ... \tag{5.1}$$

Only the terms up to and including the second derivative need to be considered, as only even terms contribute to the rectification of a signal, and the factorial dividers in the equations make tertiary terms unimportant. Assume that the voltage will be an AC signal, and therefore can take the form $V = V_0 cos\omega t$. Applying this and taking an average of the resulting equation gives Equation 5.2.

$$< I(t) >= \frac{dI}{dV}.V_0 < cos\omega t > + \frac{1}{2!}.\frac{d^2I}{dV^2}.V_0^2 < cos^2\omega t > \tag{5.2}$$

where,

V_0 = Amplitude of AC voltage across rectenna

The $cos\omega t$ term averages to zero and the $cos^2\omega t$ averages to 0.5. Therefore, Equation 5.3 is valid.

$$< I(t) >= \frac{1}{4}V_0^2.\frac{d^2I}{dV^2} = \frac{1}{2}V_{0(rms)}^2.\frac{d^2I}{dV^2} \tag{5.3}$$

where,

$V_{0(rms)} = \frac{1}{\sqrt{2}}.V_0$

This can be expanded so that it includes the power into the diode, as seen in Equation 5.4.

$$< I(t) >= \frac{1}{2}V_{0(rms)}^2.\frac{dI}{dV}.\frac{dV}{dI}.\frac{d^2I}{dV^2} = P_L.CC \tag{5.4}$$

where,

P_L= Power in at the diode [W]

The curvature coefficient is also described as the intrinsic responsivity [61]. The zero bias curvature coefficient is a figure of merit calculated for each device from the DC I-V characteristics to give a measure of the non-linearity of the device at

zero volts. By contrast, the intrinsic responsivity is a device parameter defined as the amount of current output from the diode alone, for a given AC power input. Furthermore, this should also not be confused with the current responsivity results discussed in this thesis as the intrinsic responsivity does not evaluate the entire system associated with each diode, but merely the diode itself.

Another important factor involved with the analysis of these diodes is that they are not 50 Ω devices, and therefore would not be impedance matched to an antenna. With impedance matched devices, the voltage would be split equally between the antenna and diode in a potential divider configuration ($V_{0(rms)} = 2.V_L$). As a result, Equation 5.5 would be true, assuming a 50 Ω impedance antenna.

$$P_L = \frac{V_L^2}{R_A} \Rightarrow V_L = \sqrt{R_A.P_L} \tag{5.5}$$

However, with diodes, which have a much higher resistance than the 50 Ω antenna (for example), it can be assumed that the voltage across the diode is approximately equal to the voltage across the whole device, i.e. twice the voltage of the impedance matched equivalent ($V_{0(rms)} \approx V_L$).

The rectified voltage can be defined as the average current (Equation 5.3) multiplied by the resistance, $\frac{dV}{dI}$, as seen in Equation 5.6.

$$V_{DC} = \frac{1}{2} V_{0(rms)}^2 .CC \tag{5.6}$$

Therefore, for an impedance matched system, using Equation 5.5 the relationship between the AC voltage and input power can be found, as seen in Equation 5.7.

$$V_{0(rms)}^2 = 2^2 \left(\sqrt{R_A.P_L}\right)^2 = 4.R_A.P_L \tag{5.7}$$

Therefore, the rectified voltage can be related to the curvature coefficient (CC) and power (P_L) for an impedance matched system, as seen in Equation 5.8.

$$V_{DC} = \frac{1}{2} V_{0(rms)}^2 \frac{\frac{d^2I}{dV^2}}{\frac{dI}{dV}} = 2.R_A.P_L.CC \tag{5.8}$$

These equations will be used later to analyse and compare experimental results.

However, in order to obtain the raw I-V results, two different pieces of equipment were used and are discussed.

Interfacing with HP4145B - C Programming

The aims of this interface program were to alter the measurement parameters and to retrieve the data from the parameter analyser in order to provide analysis using the fitting technique described in Section 5.4.1. This was achieved by replicating each of the menu screens on the parameter analyser, and communicating with it via a GPIB to USB cable and a combination of sent data strings and queries. Parameters could be set and data retrieved using this C program, allowing quantitative analysis to take place.

In order to interpret the data the C program was used to output the data to a text file, which could then be imported into an Origin template which was designed to accept the voltage and current data, and apply a 9th order polynomial fit to it. This fitted data was then differentiated twice and the resulting information used to provide the zero bias curvature coefficient, zero bias resistance, peak curvature, and current ratio, as well as graphs of each of these as a function of voltage. These parameters were then used to compare the diodes.

Interfacing with Agilent B2902A SMU

Due to the voltage resolution limitations of the HP4145B, the measurement equipment was upgraded to include an Agilent B2902A Source and Measurement Unit (SMU), which has an improved voltage resolution of 1 µV and a current resolution of 100 fA (specified). It was later discovered the resolution of the measured current was larger than this, due to the cables used in the test configuration.

In order to improved the diode testing rate, a Matlab program was devised in collaboration with a project student to not only control the SMU but also to perform the analysis in real-time and save the resulting data in an Excel file. Rather than having to input data into an Origin template, the data was analysed and the current ratio shown to the user prior to saving the data, thus giving instant feedback as to whether or not the I-V data should be saved, which significantly reduced the amount

of time taken to test and analyse the diodes.

5.4.2 AC Analysis

AC analysis of the diodes took place using both an HP 4192A LF Impedance Analyser (5 to 13 $\times$ 10^6 Hz) and an Agilent 8753C Vector Network Analyser. The impedance analyser was controlled using a Labview-based program and tested diodes from 0.5 to 5 MHz. While initial testing took place in this manner, higher frequency results were needed to further investigate the diode functionality, and so a VNA was used that can test from 300 kHz to 3 GHz. However, in order that high frequency testing could take place, the diodes had to be designed within coplanar waveguide structures, which would allow the propagation of the high frequency signals without significant losses. Figure 5.8 shows the diodes incorporated into the waveguide structure. The titanium/gold contacts are visible in yellow with the platinum contact in the centre (light grey). The diode structures can be seen as the small crossover lines, (titanium in dark grey) in between the three contact probes.

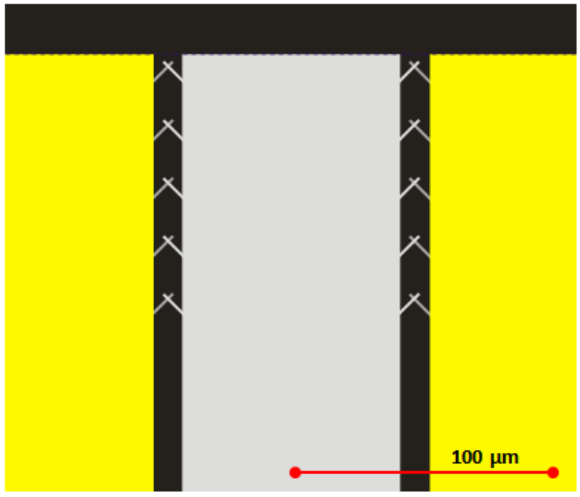

Figure 5.8 *– Mask layout close-up of VNA diode, showing the three point probe contacts, with the diode crossovers between the contacts. This example shows two columns of 5 diode crossovers.*

The diodes were either singular or in multiples and the gap between the three contact pads was varied with 10 µm, 12 µm and 14 µm gaps tested. There are also two different layout options, the first (known as layout 1) has the three contacts with

the diodes between them, as shown in Figure 5.8. The alternative layout involved connecting the two outer connections, as seen in Figure 5.9 (known as layout 2).

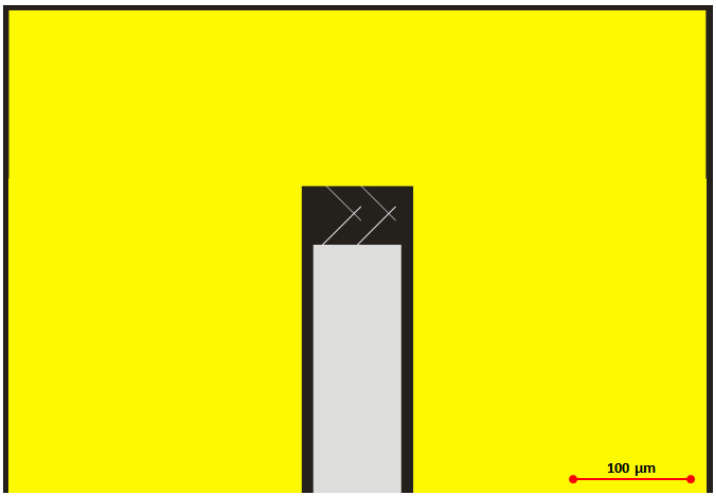

Figure 5.9 *– Mask layout close-up of VNA diode - alternative layout where two of the three contacts are shorted out. This example shows two diode crossovers.*

All VNA diodes were first visually inspected for any mask or fabrication based errors, including mask short or open circuit errors and gold etch failures. They were then DC tested as described in Section 5.4.1. Diodes which were also AC tested were connected to the VNA via a 150 µm GSG probe, the bias connect of which is connected to the SMU and again controlled via a Matlab program (Figure 5.10). Diodes were tested in the range ±0.2 V with 1001 data points being taken. Furthermore for each diode, the zero bias curvature, peak curvature, zero bias resistance, forward to reverse current ratio and peak current density were calculated and used in combination to determine the diode functionality. The adj R^2 value was calculated for each polynomial fit to ensure that the analysis used was an accurate representation of the actual raw data.

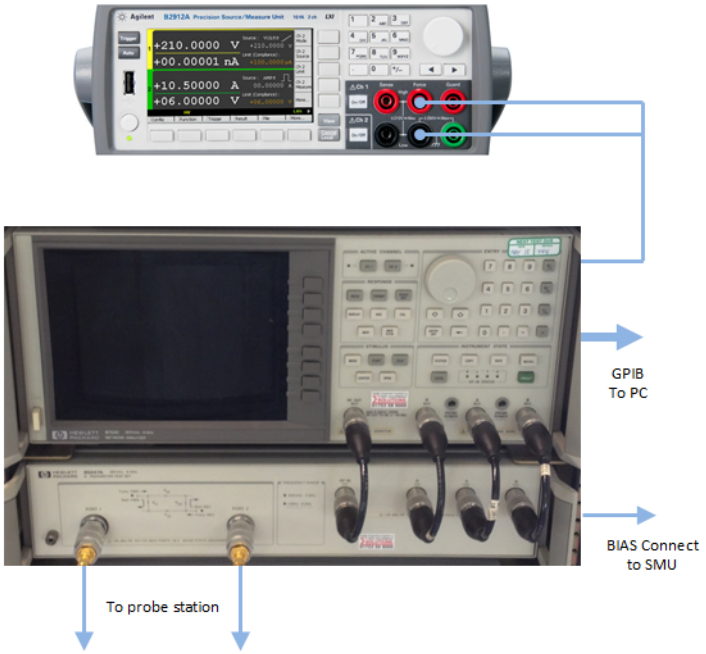

Figure 5.10 – *Agilent 9753C VNA and Agilent B2902A SMU connections*

A Matlab program was used to interface with the Vector Network Analyser (VNA), which was created to control the VNA menu and the desired parameters and subsequently output the results of various tests to an Excel file. Data recovered included the DC output voltage and current for power sweeps from −5 to 0 dB and at frequencies from 300 kHz to 3 GHz. Results of these experiments can be found in Chapter 7. The data recovered was used to calculate the voltage and current responsivities by calculating the millivolt input power from the VNA and measuring the voltage and current output. Responsivity is a measure of the amount of output current (in amps) or voltage (in volts), per watt of power in and is a common figure of merit. Each responsivity can be found as a gradient on a voltage or current versus input power graph.

Additionally, the cut-off frequency and capacitance of each device was recorded. The cut-off frequency was taken as the half output point of each device.

5.4.3 Cryostat

In order to understand the nature of the diode conduction, temperature varied I-V measurements were taken using an Oxford Instruments OptistatDN cryostat, which

was connected to an Oxford Instruments ITC5035 Temperature Controller and a Keithley 2635A source meter, and controlled via Labview-based software. Liquid nitrogen was used to cool the sample down to 77 K and then I-V measurements were taken at 10 K intervals in the range 80 to 350 K, with a 20 minute delay between the controller achieving the desired temperature and the reading being taken in order to reduce any temperature lagging effects. Throughout this process the sample was in a helium environment at atmospheric pressure.

The setup of the Cryostat can be seen in Figure 5.11 (adapted from [104]). As can be seen, through the use of valves both the sample and outer chambers can be pumped out or filled with helium as appropriate. The liquid nitrogen is poured into the inlet until the chamber is filled (which can be seen at the outlet), and the nitrogen needle valve is first opened to allow the chamber to cool very quickly. It is then closed so that it is only open by a quarter turn in order to minimise the liquid nitrogen evaporation.

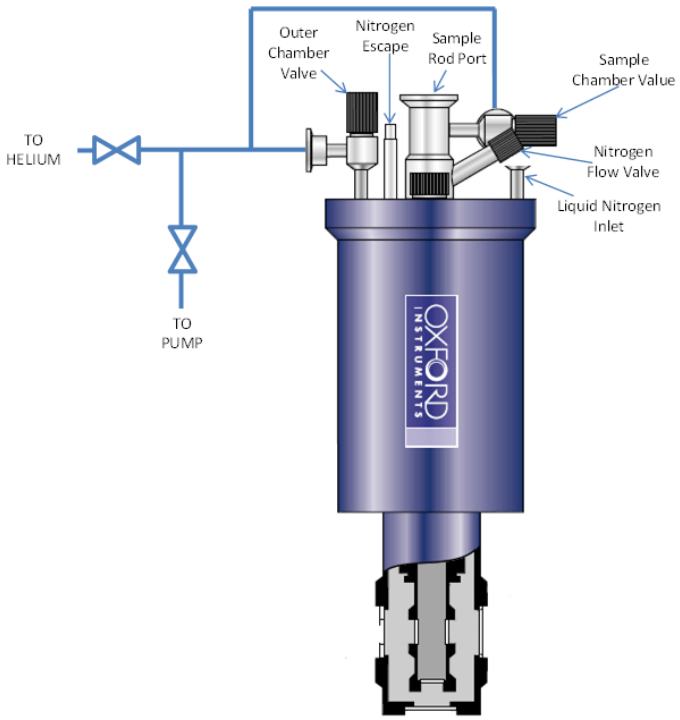

Figure 5.11 – *Cryostat configuration (©Oxford Instruments) - including connections to pump and helium cylinder*

5.4.4 Atomic Force Microscopy

All AFM analysis was performed using a Veeco Dimension 3100 AFM. Atomic Force Microscopy was used for numerous tasks, including measurements in the x and y planes, for diode crossover areas for example, for z height measurements to give film thicknesses, for roughness calculations, for wafer uniformity experiments as well as failure analysis.

5.4.5 SEM

A Hitachi S-2400 Scanning Electron Microscope has been used to provide topographical images of various samples. Scanning Electron Microscopy (or SEM) produces a topography of a sample by scanning it with a focussed beam of electrons. In secondary electron emission, as the electron beam traces over the sample, secondary electrons are dislodged from the surface of the sample, are attracted to the secondary electron detector and the amount of electrons detected determines the screen brightness for that pixel. Secondary electron emission is favourable to primary electron emission as it requires much lower energies, therefore the beam of electrons which must be detected can be deflected so that the detector can be placed at a chosen location within the chamber. This means that there is more flexibility with regards to electron detection and the size and contrast related topography of the samples can be more varied than if the detector was placed to detect direct electron deflections, as is the case with primary electron emission.

The sample is scanning and the resulting image is composed on a pixel-by-pixel basis, until an entire image is created. As the samples are being bombarded by electrons, they should ideally be conducting and therefore it is commonplace to sputter coat the samples in gold prior to analysis to optimise conductivity and prevent localised charging. Again, secondary emission, being at lower energies also helps to eliminate this.

5.4.6 ToFSIMS

Time of Flight Mass Spectrometry (ToFSIMS) is a method of determining the stoichiometry of a sample by sputtering a sample surface and detecting the ions which are removed from the it. *"All singly charged ions dropping through a potential difference V will acquire the same translational energy eV. Therefore, those of the largest mass will have the lowest velocities and the longest time of flight over a given distance"* [105]. Given this, individual ions can be attributed to different detection times and thus an image of the stoichiometry of a sample as it is corroded can be determined. In collaboration with David Scurr of Nottingham University, Time of Flight Mass Spectrometry (ToFSIMS) was used to provide further information regarding the thickness and stoichiometry of the oxide layer in the MOM diodes.

A negative ion scan at 3 kV was used to perform sample tests and the results from these can be found in Chapter 6 and in Chapter 7.

5.4.7 Focussed Ion Beam (FIB) and Transmission Electron Microscopy (TEM)

In order for TEM analysis to take place, cross section samples must be removed from the devices and thinned using a FIB. Small sections of samples were cut using a FIB and then attached to a rod using deposited platinum as a bond, which allows this small sample to be removed from the substrate, as seen in Figure 5.12.

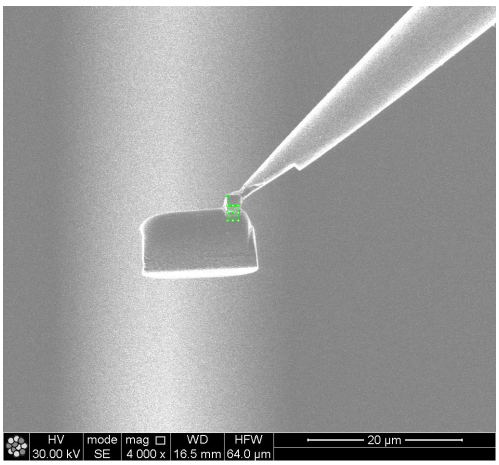

Figure 5.12 *– FIB sample bonded to rod using platinum*

The sample on the rod is then moved towards a copper jig, which it can be attached to, as seen in Figure 5.13.

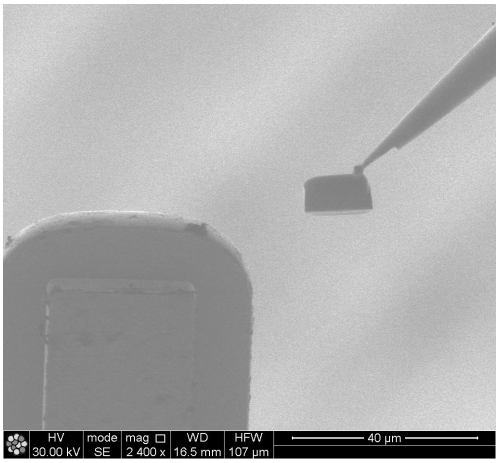

Figure 5.13 *– FIB sample being moved towards copper jig*

The sample is then attached to the jig using the same platinum deposition technique used to attach it to the rod previously. Once securely attached, the connection to the rod can be severed and the process of thinning the sample can take place, as seen in Figure 5.14. The horizontal lines on the sample denote different materials on the sample cross section.

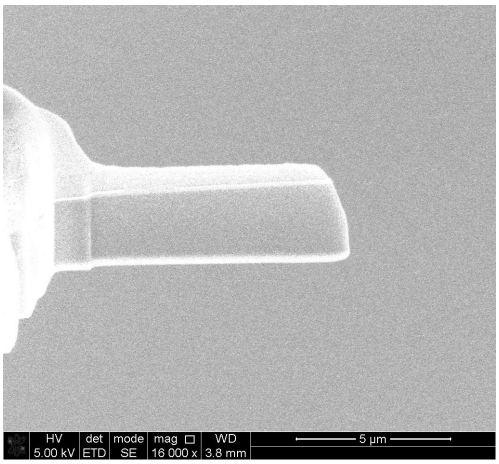

Figure 5.14 *– FIB sample attached to copper jig ready to be thinned*

Once thinning is complete this process is repeated for subsequent samples on the same jig in preparation from TEM analysis. This method of TEM sample preparation allows very precise control of sample thickness thus ensuring very reliable samples for subsequent analysis as the thickness of each sample can be duplicated.

Transmission Electron Microscopy (or TEM) involves transmitting electrons through an extremely thin sample. Depending on what material they are passing through and that material's ability to absorb electrons, the contrast will vary on the resulting image. Due to the fact that electrons are used, the resolution of a TEM is significantly better than other analysis techniques, with the structure of atomic clusters being visible and single nanometres clearly defined. Scanning TEM uses this standard TEM principle but scans the detection point over the sample in a raster, creating a high resolution image of a sample. As a result, this technique is used to help confirm the oxide thicknesses.

5.5 Conclusion

Various fabrication processes have been discussed which were used in this project including the bi-layer lift off technique which is used as the basis for most processes. Phase shift lithography is also discussed, which was used to produce sub-micron features. The various analysis techniques for both electrical and physical analysis were also discussed, including the I-V curve polynomial fitting analysis and the various scanning electron techniques, which, when combined together, were used to determine the suitability of the various oxides for the insulating layer in the MOM diode structure. The application of these processes is discussed throughout the thesis.

Chapter 6

Production of Diodes with Thermally Grown Oxide

6.1 Introduction

This chapter details the device fabrication process of furnace oxidised diodes with dimensions down to 10 x 10 μm and the fundamental findings from the analysis of these diodes, including their I-V characteristics, curvature coefficients and current ratios. Both physical and electrical analysis is included: cryostat testing and conduction mechanism analysis, AC testing, DC testing as well as TEM, AFM, RBS and ToFSIMs. The failure mechanisms are also discussed.

As discussed in Chapter 4 (Equation 4.15) the capacitance of the diodes must be minimised. As can be seen from Equation 4.16, in order to do this the relative permittivity and the surface area must be minimised, and/or the oxide thickness maximised (which is counter-productive to having a thin oxide for tunnelling). For initial diode production, standard lithographic techniques were used which limited the minimum feature size to 10 μm in each dimension. Further fabrication details are given in Section 6.2.

6.2 Fabrication

As has been discussed in Chapter 4, in order to maximise the asymmetry of the diode, metals with different work function differences can be used. The titanium-platinum combination was chosen due not just to the work function difference but also the ability of the titanium to oxidise readily, and the inert nature of the platinum.

6.2.1 Lift-off Process for Micron-Scaled Devices

The fabrication process is shown in Figure 6.1. N-type $\langle 100 \rangle$ silicon of 10 to 30 Ω cm resistivity was chosen as the initial substrate material (2" diameter wafers) and was oxidised to provide an insulating 1000 Å film. A bi-layer lift-off process was used to produce a base layer pattern on the substrate. PMGI SF9 was spun onto the substrate at 500 rpm for 10 s then 6000 rpm for 50 s using a Laurell spinner, resulting in a layer approximately 500 nm thick [100]. This was then baked at 200 °C for 5 minutes. Microposit SPR-350 photoresist was then spun on top of this at 700 rpm for 10 s then 3700 rpm for 50 s using a Laurell spinner, and baked at 110 °C for 3 minutes. A dark field chromium mask was then used in an EVG 620 mask aligner to expose regions of the substrate to UV light for 4 s. The substrate was then developed for 2 minutes using MF-319 developer, ensuring undercutting of the SPR-350 by the SF9. 25 nm of titanium and 100 nm of gold were then deposited in the same e-beam evaporation process (Figure 6.1a). In this device the gold acts only as a contact pad. The excess metal was removed by stripping the photoresist below the metal, using Microposit 1165 stripper.

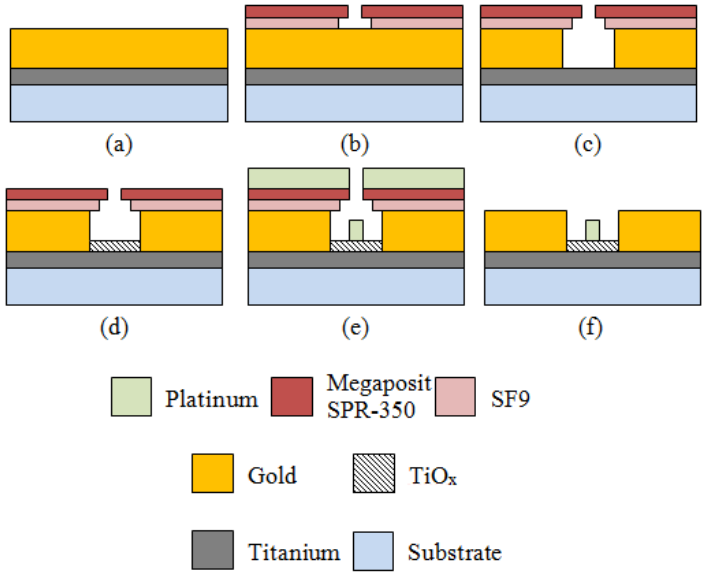

Figure 6.1 *– Lift-off fabrication process - (a) substrate with titanium-gold coating, (b) bi-layer lift-off pattern in photoresist, (c) gold etched away in pattern of photoresist, (d) oxidation of exposed titanium, (e) platinum deposition, and (f) removal of excess platinum and photoresist*

The lift-off process was repeated, as in (b), and then an etchant (4:1:8 KI:I_2:H_2O) was used to remove the uncovered gold and to undercut the photoresist, leaving a small region of titanium exposed (c). The samples were then placed in an ultrasonic bath in water for 10 s to help remove any remaining gold etch. Oxidation then took place, by placing the sample in a temperature controlled humid environment at 100 °C for 4 hours (d). The wafer was then immediately placed in an e-beam evaporator and 40 nm of platinum was evaporated, resulting in a small Ti/TiO_x/Pt region being produced (e). Finally, the photoresist was removed as above, which also removed unwanted platinum, completing the diode fabrication process (f).

6.3 Results

6.3.1 Physical Analysis

As well as electrical results, physical analysis of the diode structure was needed in order to confirm hypotheses from electrical results (i.e. I-V non-linearity and conduction mechanism findings). The following techniques were therefore used to

help elucidate the true diode structure.

AFM analysis was used to confirm the structure of the diodes, including the thickness of each metallisation layer. A typical AFM image can be seen in Figure 6.2. The top to bottom metal track is Ti/Au, while the track from left to right is Pt. The region of exposed titanium oxide is clearly visible either side of the crossover, with the crossover region itself denoting the diode.

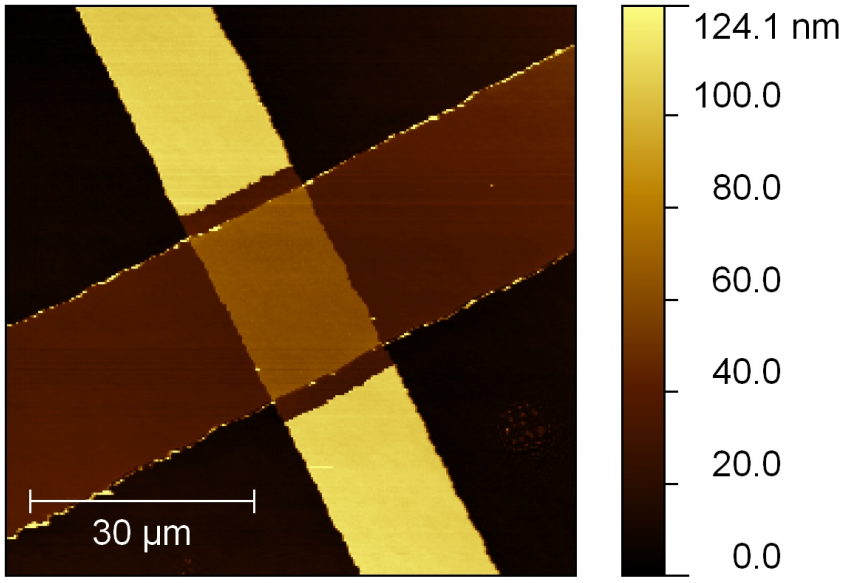

Figure 6.2 – *AFM image of a $Ti/TiO_x/Pt$ Diode*

The thickness of each of the layers was chosen specifically as a compromise between series resistance and adhesion of the platinum layer. Adhesion trials showed that large area platinum regions with a thickness in excess of 50 nm did not have sufficient adhesion to the substrate to remain attached. This is due to the stress within the film. Evaporated films increase in stress after deposition as they cool, and with platinum being a particularly high power and therefore high temperature evaporation process, the stress is significant. Unfortunately, a seed layer cannot be used in this application as the platinum must be the material to contact the oxide. Given this maximum thickness, the other thicknesses were determined. 40 nm of platinum was chosen, which then confirmed that the combined thickness of the titanium and the grown oxide must be less than this, to ensure that no step height discontinuities occur at the diode overlap interface. Therefore 25 nm of titanium was

chosen as a suitable thickness. AFM analysis confirmed a tooling factor of as low as 0.8 on the electron beam evaporator, resulting in a platinum thickness down to 32 to 38 nm and a titanium thickness of 20 to 23 nm, leaving a 9 to 18 nm difference to accommodate for the oxide layer and the step height of the titanium at the crossover region, seen in Figure 6.3.

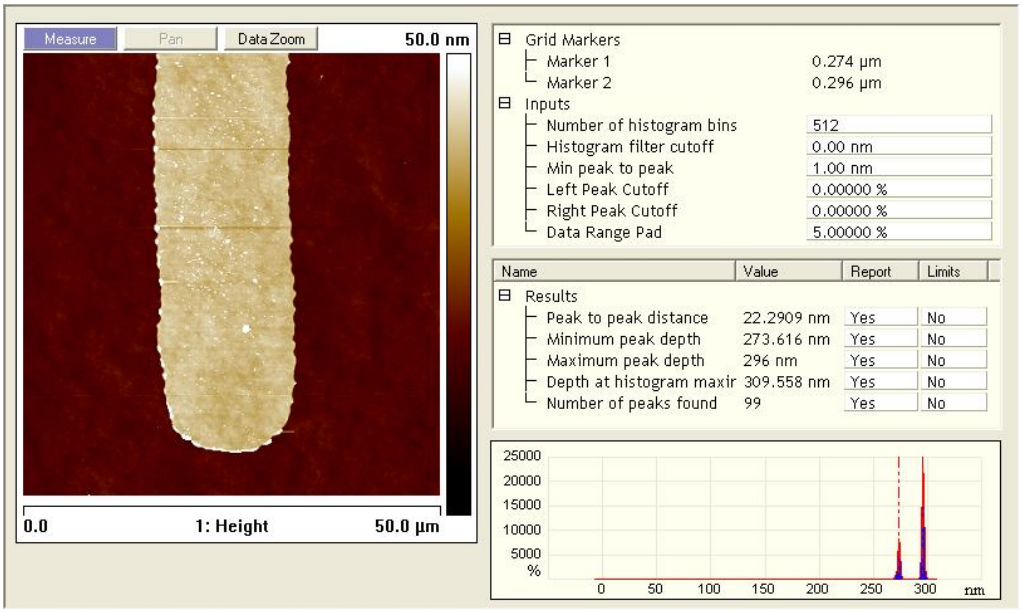

Figure 6.3 – *Typical AFM profile of a titanium deposition*

The variability of layer thickness was also investigated via step height testing at different regions on the wafers. Variations in thickness are caused by the angle of evaporation in the electron beam evaporator. This was minimised by ensuring that the samples were, wherever possible, immediately above the crucible source thus ensuring a perpendicular deposition and a more uniform thickness.

In order to gain an appreciation of the oxide thickness and composition, TEM analysis was used to view a cross section of the diode structure. In preparation for this, a sample of a diode was extracted and thinned using Focussed Ion Beam (FIB) technology, which is discussed in Chapter 5. Figure 6.4 shows a FIB image of one of the diode cross-sections, where the horizontal line is titanium/gold, and the vertical line is platinum, with the central crossover denoting the diode itself.

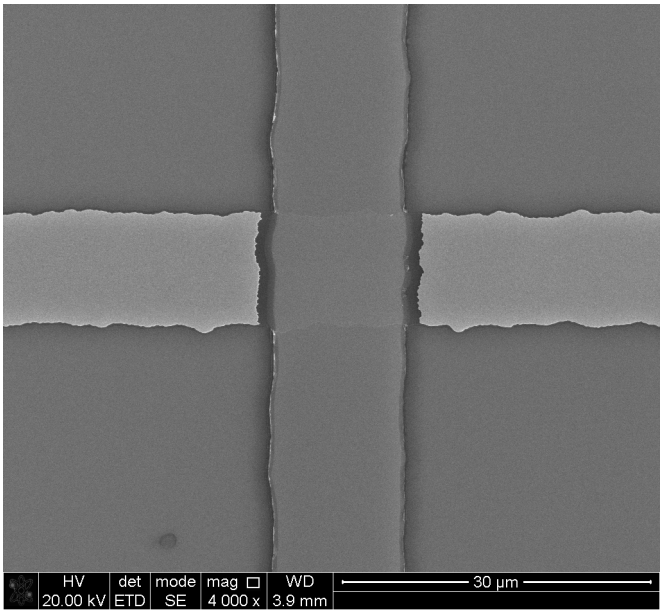

Figure 6.4 *– FIB image of diode crossover - horizontal line is the titanium-gold line, with the central gold region having been etched away. The vertical line is the top platinum layer, with the crossover region denoting the diode*

Transmission Electron Microscopy (TEM) analysis of sample diodes was used to determine the nature of the native titanium oxide grown via wet furnace oxidation. Figure 6.5 shows a dark field image of two diode cross sections, where both the collimated structure of the titanium metal, and the titanium oxide above it, can be seen clearly. Titanium preferentially forms in a collimated structure when evaporated. The 2 hour oxide is, on average, 6 nm thick, whereas a 4 hour oxide is thicker at 7.6 nm, on average.

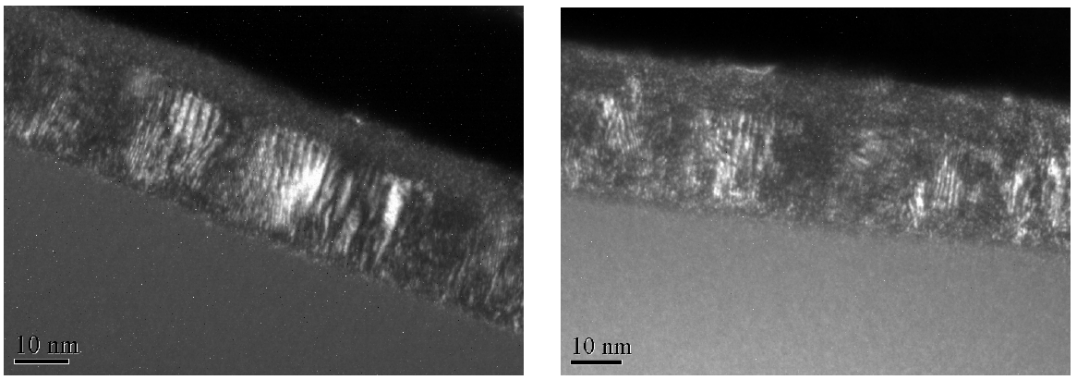

Figure 6.5 *– Dark field TEM image of (bottom to top) SiO_2, Ti, TiO_x, and Pt (appears black here) (2 hour oxide on left, 4 hour oxide on right)*

Figure 6.6 shows two high resolution (HREM) images of the titanium layers and

their native oxides. Again, the collimated structure of the titanium can be seen, in contrast to the native oxide. The variations in oxide thickness can also be seen, particularly in the 4 hour oxide layer, which may help explain our observations of variable electrical performance of subsequent diodes. In contrast, the thinner oxide layer produces more uniform electrical results.

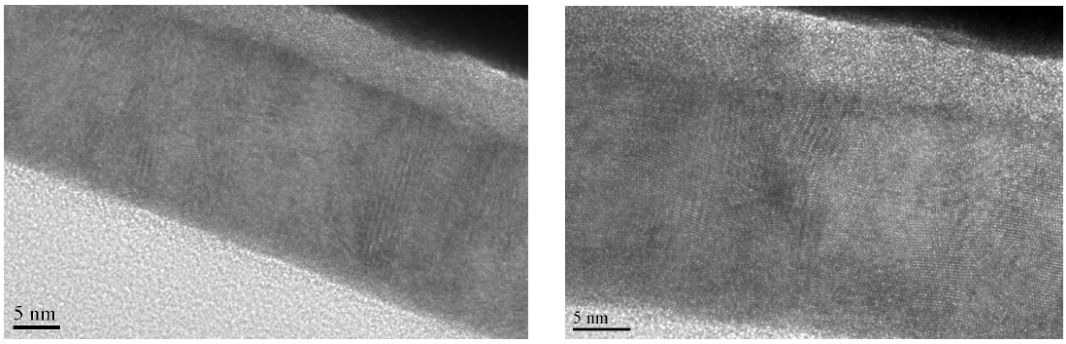

Figure 6.6 *– HREM image of the titanium and titanium oxide layers of a MOM diode (2 hour oxide on left, 4 hour oxide on right)*

Rutherford Back Scattering (RBS) analysis, which is a technique used to determine the nature of a sample by monitoring the backscattered beam of high energy ions which have been incident on the surface, has also been performed on a range of samples. Figure 6.7 shows a typical raw data plot. From this, curve fitting software is used to acquire the material thicknesses. As measured immediately after deposition, results suggest a 2 to 3 nm thick oxide grows on a titanium layer without any oxidation processing. From there, the results are more ambiguous: despite trying a range of oxide preparation times, we were unable to detect any conclusive increase in the oxide thickness.

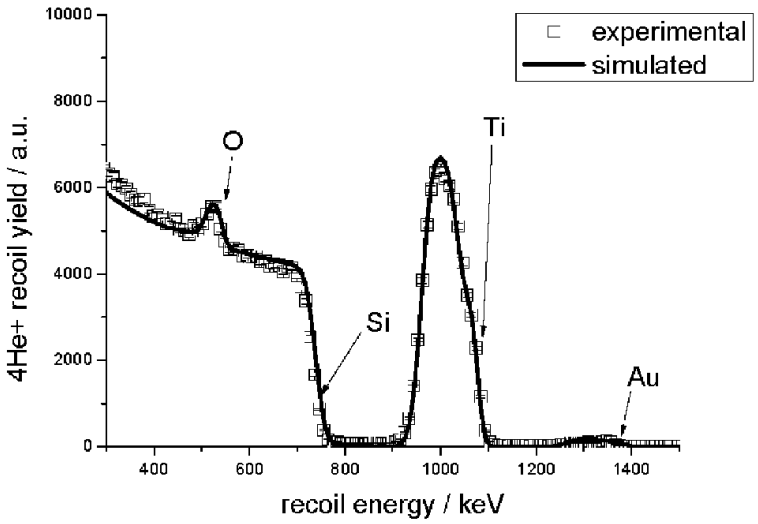

Figure 6.7 *– RBS analysis of oxidised Ti on silicon*

These results are at odds with the electrical results, and typical TEM images, which are influenced by oxide preparation time. The RBS results were attributed to working at the limits of the sensitivity of the equipment. Therefore, other surface analysis techniques, including ToFSIMs (Time of Flight Secondary Ion Mass Spectrometry) were used to elucidate both the thickness and the stoichiometry of the oxide under different preparation conditions as an alternative to this technique.

Figure 6.8 shows the results from a 3 kV negative ion scan of a 4 hour furnace diode sample and the resultant titanium oxide-based ions which were identified.

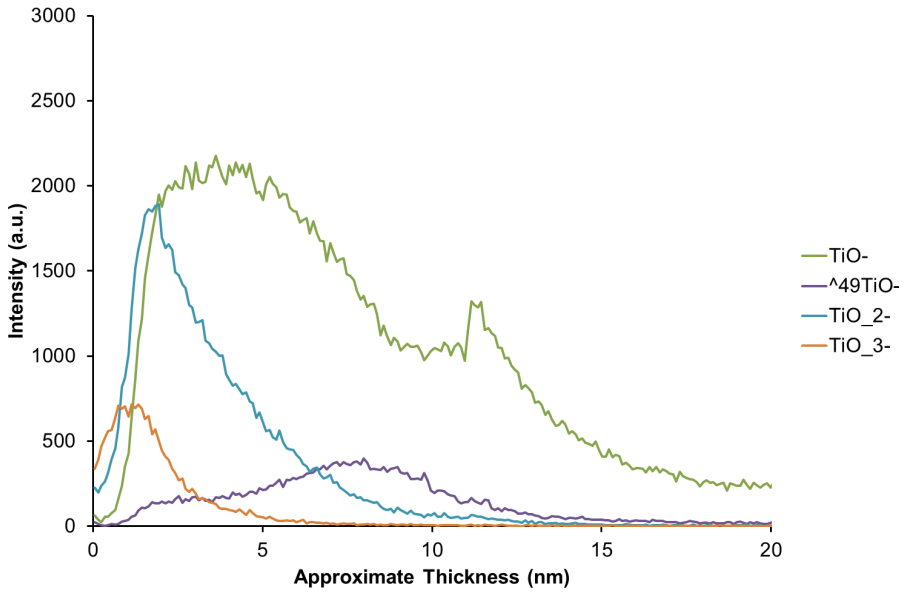

Figure 6.8 *– ToFSIMS analysis of oxide content for 4 hour furnace diode - the graph shows progression down through the sample (left being the top of the sample)*

A range of oxides combine to form the overall oxide layer, with TiO, which is sub-stoichiometric, dominating, thus implying that the oxide is oxygen deficient. With regards to the thickness of the layer, a standard measurement method was determined to ensure consistency between samples. The thickness of the sample was determined as the intensity of the sample midway between the peak point and the settling intensity (Ti region), and from this the corresponding thickness points were used to determine oxide thickness. Here the oxide thickness is 6.9 nm, which is comparable with the 7.6 nm determined by TEM, especially given the observed variation in thickness of this oxide layer.

6.3.2 DC Analysis

The diodes were tested as discussed in Section 5.4.1. A typical I-V plot with 201 data points is shown in Figure 6.9, where the non-linear and asymmetric diode characteristics can be seen clearly.

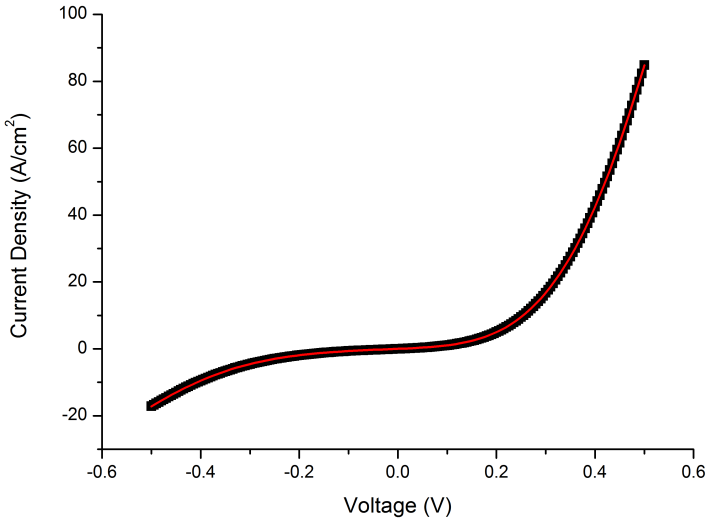

Figure 6.9 – *J-V characteristic of a typical 4 hour furnace $Ti/TiO_2/Pt$ Diode, with the polynomial fit overlaid in red*

As can be seen, the forward to reverse current ratio is also significant at approximately 4.5 at a voltage of ±0.3 V. This is vital as it indicates the likelihood of there being a net current when an AC signal is being rectified. The same data on a logarithmic scale can be seen in Figure 6.10.

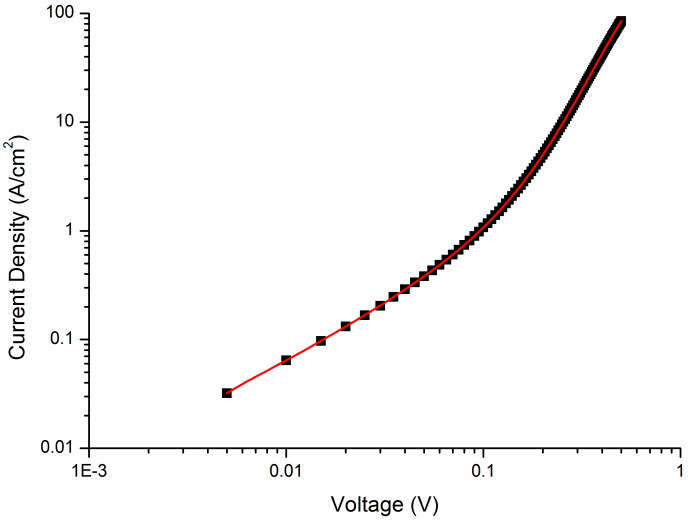

Figure 6.10 – *J-V characteristic of a typical 4 hour furnace $Ti/TiO_2/Pt$ Diode, with the polynomial fit overlaid in red (log scale)*

Figure 6.11 shows the typical variation in resistance with voltage. As can be

seen, the peak resistance occurs at approximately −25 mV, which according to [70] can be used to determine the nature of conduction of the diode and the impact of oxide impurities.

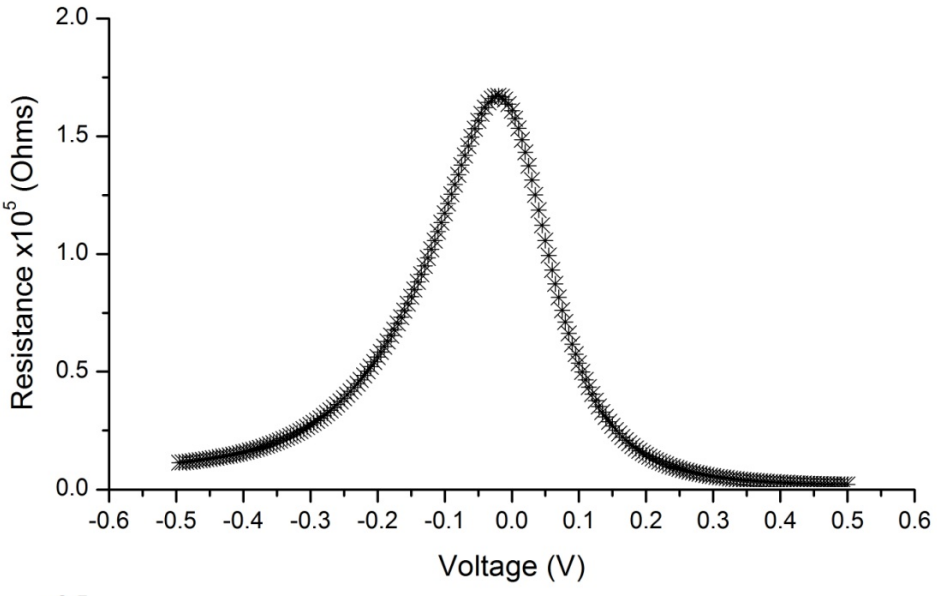

Figure 6.11 – *Resistance of a 4 hour furnace diode*

A quoted figure of merit for these devices, curvature coefficient (CC), is plotted against voltage in Figure 6.12. As is commonplace, the highest value of curvature (typically 15 to 20 V^{-1}) is away from the ideal value of zero bias. Nevertheless, the typical value of CC obtained from these $Ti/TiO_x/Pt$ diodes (5.5 V^{-1} at zero bias) is very competitive when compared with results published from other metallisation systems, e.g. [26]. The curvature coefficient is calculated using a polynomial best fit curve and so is stated to only 2 significant figures.

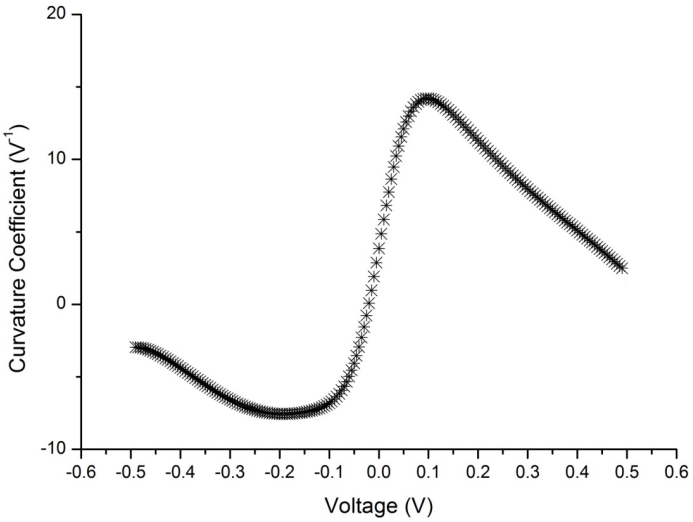

Figure 6.12 – *Curvature coefficient of a 4 hour furnace diode*

Figure 6.13 shows a typical plot of process uniformity with values of CC across a wafer, showing a good (78%) device yield from the fabrication. The numbers around the edges represent the track width in microns, e.g. where 10 and 15 intersect is a diode of dimensions 10 x 15 μm.

	10	12	14	16	18	20	22	24	
	8	1	8	1	8	1	8	1	
15	X	X	5.5	1.1	4.3	2.8	4.5	5.4	15
15	0.7	X	0.9	1.2	2.3	4.7	3.7	5.6	15
15	5.5	X	1.1	2.3	3.9	4.7	3.4	3.9	15
15	4.4	1.3	1.3	2.3	X	X	X	2.0	15
15	3.2	1.4	2.2	4.1	1.3	1.1	X	X	15
15	5.9	1.0	2.3	1.4	X	0.9	0.9	0.5	15
15	4.6	1.6	1.5	X	X	X	2.0	3.7	15
15	4.5	1.2	2.2	X	1.5	1.2	1.1	3.7	15
	1	8	1	8	1	8	1	8	
	10	12	14	16	18	20	22	24	

Figure 6.13 – *Distribution of zero bias curvature coefficient across a wafer - the dimensions of the diodes (10, 12, 14,...24) are displayed around the outside, with their number references (1 and 8) displayed at the end of each column. X symbols show failed diodes, either as a result of fabrication defects or or electrical results*

Figure 6.14 plots CC against resistivity, and shows clearly the general trend between these parameters, with a good correlation between the two. It is worth noting the mathematical relationship between these two parameters, however. As discussed in Chapter 5, the resistance is calculated from the 9th order polynomial fit to the I-V curve as dV/dI. The curvature coefficient is defined as $(d^2I/dV^2)/(dI/dV)$ and is therefore proportional to resistance, and results in Figure 6.14 will be dominated by this trend. However, the correlation to this trend gives a measure of repeatability between diodes, as well as being a basis for comparison with results from other research institutions e.g. [26].

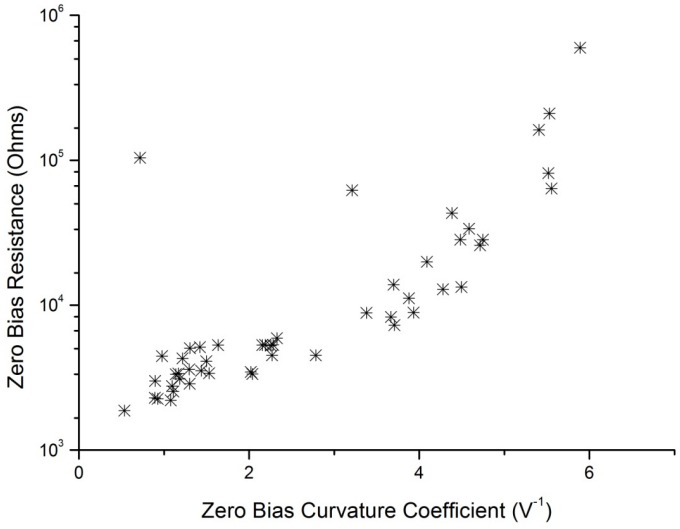

Figure 6.14 *– Zero bias resistance vs curvature coefficient*

The Effect of Oxide Thickness on Diode Performance

Diodes which have been produced with a 4 hour oxidation process have much higher curvature coefficients and larger resistances than the 2 hour oxidation diodes, but their values are less uniform. Figure 6.15 shows a comparison between the peak curvature coefficient of the 2 hour diodes and the zero bias curvature coefficient of the 4 hour diodes. As plotted by wafer position, the 4 hour diodes are much more useful at zero bias, whereas the thinner oxides appear to require biasing in order to show rectification qualities. These results are perhaps at first surprising, given the slight difference in oxide thickness between the two oxidation regimes, but they are

consistent.

The more uniform electrical results for a thinner oxide could be a result of a more uniform oxide, but we are at present unable to confirm this. The yield is also lower for these devices, which may simply be due to the increased difficulty in distinguishing operational diodes. Given the values of the measured oxide thickness, it is clear that the transport mechanism may be more complicated than first thought: an oxide thickness $< 5\,\text{nm}$ is considered to be the limit for tunnelling MOM diodes. There must therefore be a compromise which provides an oxide that is of the required thickness and uniformity, which allows favourable curvature values in the diodes, and also which enables us to determine the current carrying mechanism(s).

	10	10	12	12	14	14	16	16	
	8	9	8	9	8	9	8	9	
10	0.4	0.2	0.2	0.2	0.5	0.2	0.3	0.2	10
10	0.5	0.7	0.2	-	-	-	-	-	10
10	0.2	0.4	0.2	-	0.4	-	0.3	0.6	10
10	0.3	0.3	-	0.3	0.7	-	0.4	0.5	10
10	0.4	0.6	-	-	0.6	-	0.4	-	10
10	0.6	0.6	0.3	0.2	0.2	-	-	0.1	10
10	0.6	-	-	0.4	0.2	0.6	0.3	0.6	10
10	0.2	0.4	0.2	-	0.3	0.2	0.9	0.6	10
	1	16	1	16	1	16	1	16	
	10	10	12	12	14	14	16	16	

	10	10	12	12	14	14	16	16	
	8	9	8	9	8	9	8	9	
10	-	3.6	3.1	2.3	3.3	3.5	3.1	4.0	10
10	1.5	2.6	2.0	2.4	3.9	5.8	2.5	1.8	10
10	1.9	3.4	2.2	1.8	3.4	3.7	4.3	0.5	10
10	3.7	3.2	3.8	5.0	5.0	3.5	-	1.1	10
10	2.3	3.3	4.2	4.4	3.7	2.7	4.3	6.8	10
10	5.4	0.3	3.3	3.3	3.5	2.6	2.0	1.7	10
10	3.0	3.1	3.0	3.4	3.7	1.5	3.2	2.4	10
10	0.8	1.7	3.9	3.8	3.2	3.9	1.2	1.7	10
	1	16	1	16	1	16	1	16	
	10	10	12	12	14	14	16	16	

Figure 6.15 – *Peak curvature of a 2 hour oxide diode (left), and zero bias curvature of 4 hour oxide (right)*

6.3.3 Cryostat Testing and Conduction Mechanisms

In order to gain a better understanding of the diode conduction mechanisms, typical diodes were I-V tested at different temperatures in the range 80 to 350 K. This took place using a Oxford Instruments OptistatDN cryostat chamber, Oxford Instruments ITC 5035 temperature controller and a 2635A Keithley source and measurement unit which was controlled using an existing Labview interface program. The I-V characteristics for the diode used in this analysis can be seen in Figure 6.16.

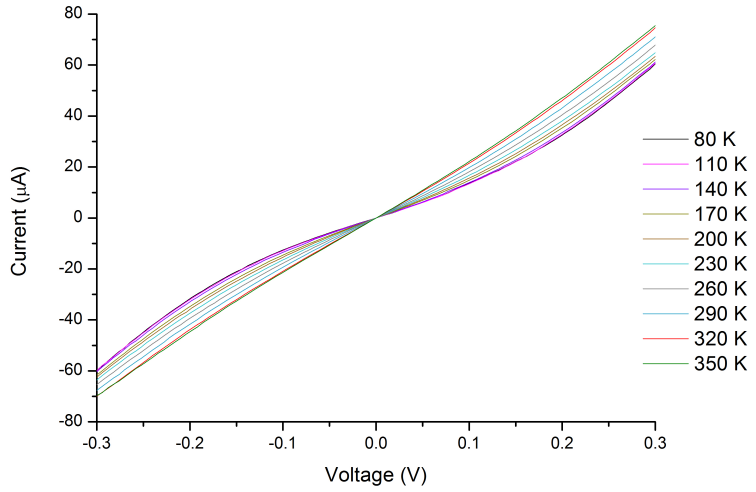

Figure 6.16 *– I-V characteristics of a typical 4 hour furnace diode for a selection of temperatures (some intermediate temperatures removed for additional clarity)*

Some of the temperatures tested have been removed from the graph to improve the clarity of the trend with temperature. The same data can be seen on a logarithmic scale in Figure 6.17. As can be seen, the current through the diode increases with increasing temperature and the I-V characteristic appears more linear with increasing temperature.

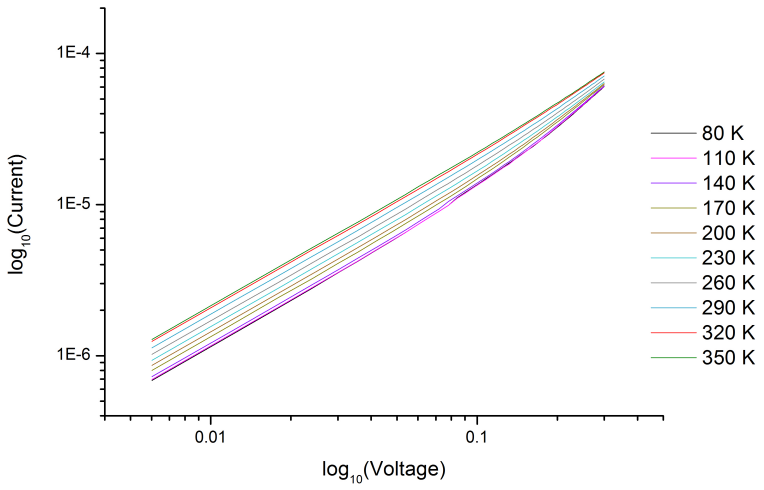

Figure 6.17 *– I-V characteristics (log scale) of a typical 4 hour furnace diode for a selection of temperatures (some intermediate temperatures removed for additional clarity)*

The subsequent results were then analysed against theoretical conduction mechanism trends, as discussed in Table 4.3, with the results summarised below. The following mechanisms were tested: Schottky, Poole-Frenkel, Fowler-Nordheim and Direct electron tunnelling.

The values of critical parameters were determined via an iterative approach, with the parameters which had the biggest impact being found and varied until the theoretical trend matched the experimental data as closely as possible. The aim was to find values which resulted in a close correlation between experimental results and the conduction mechanism equations. In order for this to be successful, values had to be found which made the two trends agree, but also the values chosen to make them match had to be realistic physical values. If the trends could not be made to match with realistic values then it was determined that the mechanism was not a valid one for the device under test. It was found that certain parameters had little effect on the results, whereas other dominated, so these dominant parameters were focussed upon to optimise the correlation between the two trends then their feasibility discussed. Any measured values were kept constant to the measured values, thus reducing the number of parameters to be varied.

Schottky Mechanism

As described in Chapter 4, Schottky conduction is described using Equation 6.1, where, for Schottky emission, this is reduced to J=J_s, and thus Equation 6.2. The exponential in Equation 6.1 is due to band bending at an interface, which is only applicable to semiconductor devices, and therefore not relevant for this application. Equation 6.2 shows the natural logarithm of the current density being proportional to $V^{\frac{1}{2}}$, which is as a result of barrier height effects caused by the presence of insulators. However, for the purposes of this analysis the full equation was used.

$$J = J_S \left\{ exp\left(\frac{eV}{nkT}\right) - 1 \right\} \tag{6.1}$$

where,

$$J_S = A^* T^2 exp\left\{ -\frac{\left(e\varphi_{bn} - e\left(\frac{eV}{4\pi d\varepsilon_0 \varepsilon_r}\right)^{\frac{1}{2}} \right)}{kT} \right\} \tag{6.2}$$

Table 6.1 shows the critical parameters for this analysis and their values.

Table 6.1 – *Critical parameters used for Schottky analysis*

Parameter	Description	Value
ϵ_r	Relative Permittivity	20
A	Area (measured)	$1.2 \times 10^{-10}\,\mathrm{m}^2$
d	Oxide Thickness (measured)	$7.6 \times 10^{-9}\,\mathrm{m}$
ϕ_{bn}	Barrier Height	0.09 eV
m_{ox}	Effective Electron Mass in Oxide	$4.55 \times 10^{-31}\,\mathrm{kg}$ $(0.5 * m_e)$

As can be seen, the barrier height is very low but the other parameters are realistic. Figure 6.18 shows the temperature plot for this data; the gradients do not even match in polarity, thus ruling out Schottky as the conduction mechanism.

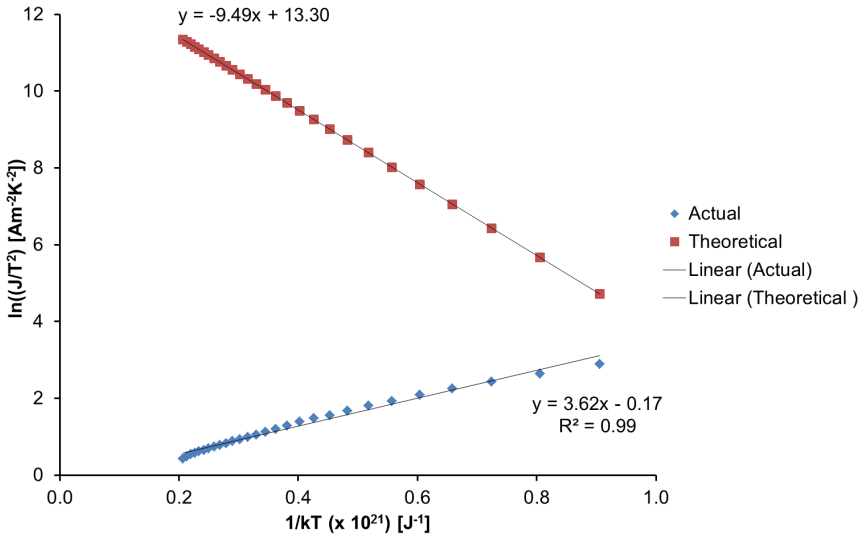

Figure 6.18 – *Graph showing $ln(J/T^2)$ versus $1/kT$ to compare the theoretical Schottky temperature dependence with the experimental results*

The voltage plot can be seen in Figure 6.19, showing a closer comparison, but neither the intercept nor the gradient is close to the theoretical value, thus showing that Schottky is not an appropriate mechanism.

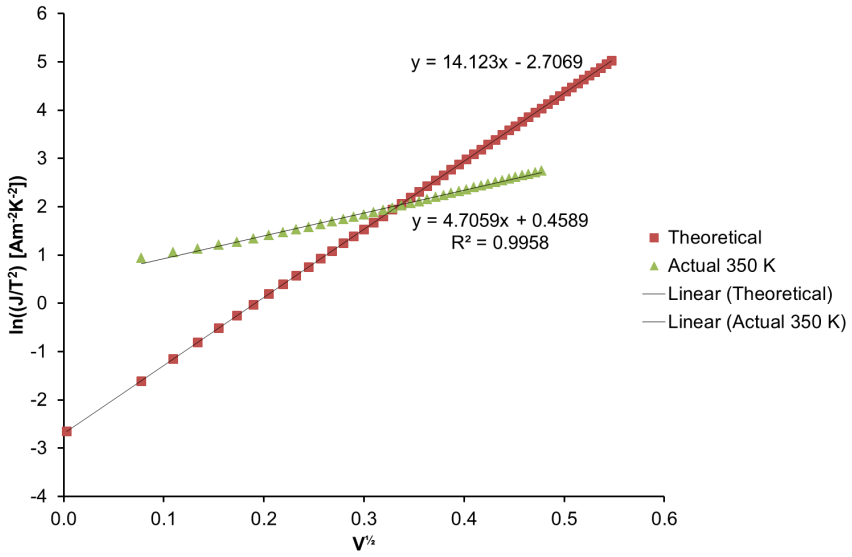

Figure 6.19 – *Graph showing $ln(J/T^2)$ versus $V^{\frac{1}{2}}$ to compare the theoretical Schottky voltage dependence with the experimental results*

Poole-Frenkel Mechanism

As discussed in Chapter 4, Poole-Frenkel conduction is described by Equation 4.13. A summary of the critical parameters for this analysis can be seen in Table 6.2. In order to determine whether Poole-Frenkel is a relevant mechanism both temperature and voltage plots must be considered.

Table 6.2 *– Critical parameters used for Poole-Frenkel analysis*

Parameter	Description	Value
ϵ_r	Relative Permittivity	200
A	Diode Cross Sectional Area (measured)	$1.2 \times 10^{-10}\,\mathrm{m}^2$
d	Oxide Thickness (measured)	$7.6 \times 10^{-9}\,\mathrm{m}$
ϕ_{bn}	Barrier Height	$0.15\,\mathrm{eV}$
μ_e	Electron Mobility in oxide	$1 \times 10^{-4}\,\mathrm{m}^2\,\mathrm{V}^{-1}\,\mathrm{s}^{-1}$
N_c	Density of States in oxide conduction band	$8.5 \times 10^{20}\,\mathrm{m}^{-3}$

Figure 6.20 shows the Poole-Frenkel temperature plot, with the theoretical and actual data. Firstly the actual data plotted should be a straight line, and here with an adjusted R squared value of 0.9561 that is a good fit but only over a small results range. Thereafter, the gradients and intercepts of the results are compared. The intercept here matches but the gradient does not. Regardless of changing critical parameters, seen in Table 6.2, these gradients cannot be made to match with realistic values. Furthermore, of these chosen values, the barrier height is lower than the expected 0.7 and the relative permittivity is higher than expected, although the permittivity range of titanium oxides varies a great deal [73], as previously discussed, and so a relative permittivity of 200 is not infeasible. As with the barrier height, both the electron mobility within the oxide and the density of states of the oxide will be unique to the oxide produced in this process and therefore they are all difficult to estimate.

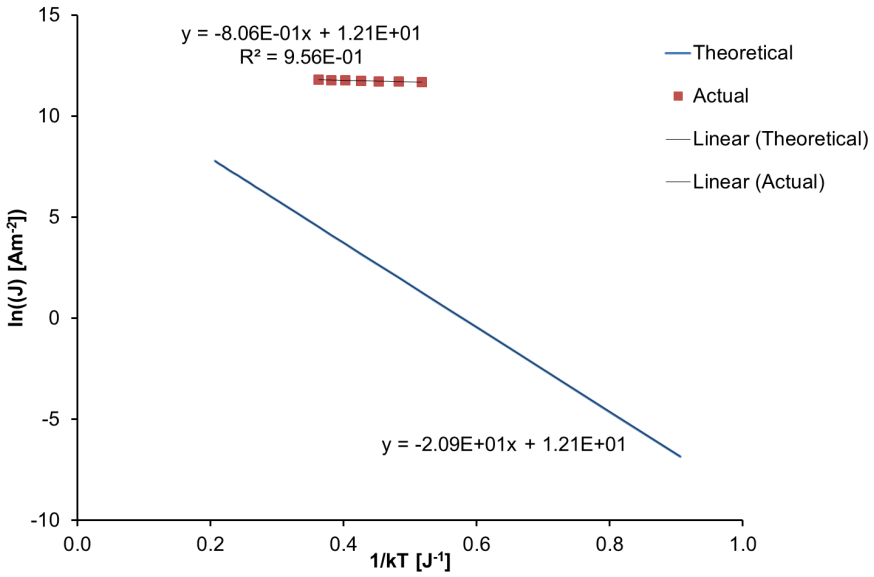

Figure 6.20 – *Graph showing ln(J) versus 1/kT to compare the theoretical Poole-Frenkel temperature dependence with the experimental results*

Figure 6.21 shows the voltage plot. As can be seen, for the same parameters as used above, neither the gradients nor the intercepts match, thus ruling out Poole-Frenkel as a conduction mechanism.

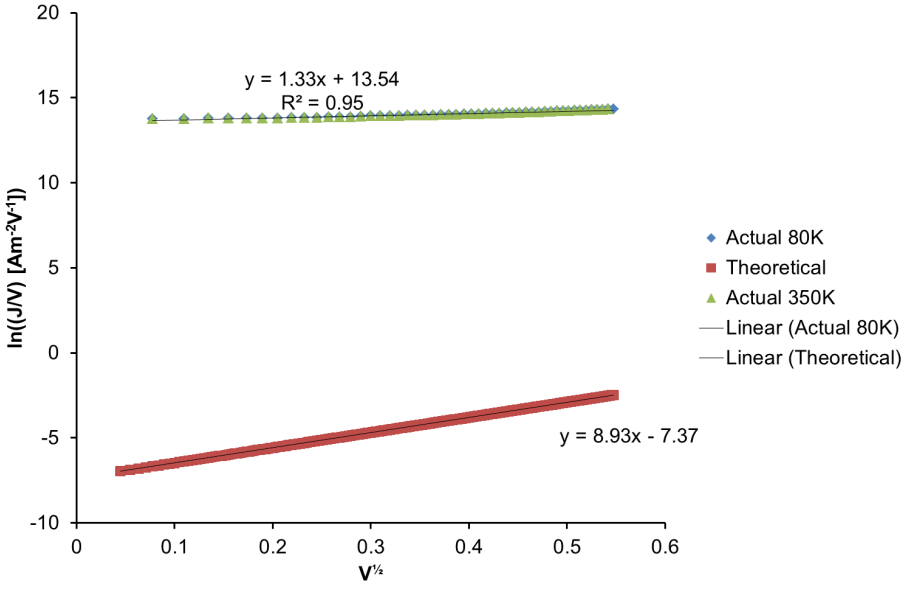

Figure 6.21 – *Graph showing ln(J/V) versus $V^{\frac{1}{2}}$ to compare the theoretical Poole-Frenkel voltage dependence with the experimental results*

Fowler-Nordheim Mechanism

Table 6.3 shows the critical parameters for the comparison between the results and the Fowler-Nordheim theoretical line graphs.

Table 6.3 *– Critical parameters used for Fowler-Nordheim analysis*

Parameter	Description	Value
A	Diode Cross Sectional Area (measured)	$1.2 \times 10^{-10}\,\mathrm{m}^2$
d	Oxide Thickness (measured)	$7.6 \times 10^{-9}\,\mathrm{m}$
ϕ_{bn}	Barrier Height	$0.09\,\mathrm{eV}$
m_{ox}	Effective Electron Mass in Oxide	$1.00 \times 10^{-30}\,\mathrm{kg}$
m_m	Effective Electron Mass in Metal	$1.91 \times 10^{-28}\,\mathrm{kg}$

As can be seen, the barrier height is low, but the area and oxide thickness are correct based on previously discussed physical analysis. As with the density of states and electron mobility earlier, it is very difficult to assign effective electron mass values for these devices, particularly within the oxide, given that both the oxide and the evaporated thin film metal will be unique to these devices. Therefore estimates based on previously published values were used and varied slightly in order to fit the theoretical and actual plots together. Figure 6.22 shows the voltage plot for this mechanism, which is not temperature dependent and therefore does not have an equivalent temperature plot. The graph shows the theoretical line and the actual results, at 80 K, and the two lines do not agree in either gradient or intercept.

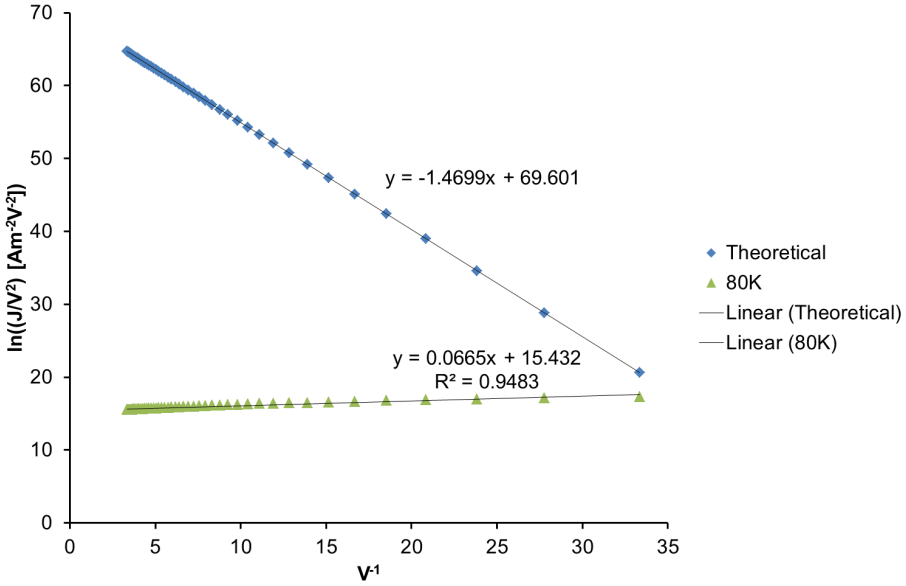

Figure 6.22 – *Graph showing $ln(J/V^2)$ versus $1/V$ to compare the theoretical Fowler-Nordheim voltage dependence with the experimental results*

Direct Electron Tunnelling

Table 6.4 shows the critical parameters for the direct electron tunnelling analysis.

Table 6.4 – *Critical parameters used for direct electron tunnelling analysis*

Parameter	Description	Value
A	Diode Cross Sectional Area (measured)	$8 \times 10^{-11}\,\mathrm{m}^2$
d	Oxide Thickness (measured)	$7.6 \times 10^{-9}\,\mathrm{m}$
ϕ_{bn}	Barrier Height	$0.8\,\mathrm{eV}$
m_{ox}	Effective Electron Mass in Oxide	$6.7 \times 10^{-31}\,\mathrm{kg}$

As can be seen, the barrier height is much more realistic that previous analysis comparisons, with the other values also realistic. Figure 6.23 shows the comparison between the theoretical and actual values obtained from cryostat data. A linear fit is not appropriate for direct electron tunnelling, hence the curved plots seen. However, these plots appear to be much closer in comparison than other mechanisms,

particularly at lower voltages. However, given the oxide thickness it would not be expected that direct electron tunnelling would be the mechanism responsible for the conduction in these devices, unless localised thin regions within the rough oxide are dominating the conduction. Furthermore, it can be seen that both the 80 K and 350 K results agree.

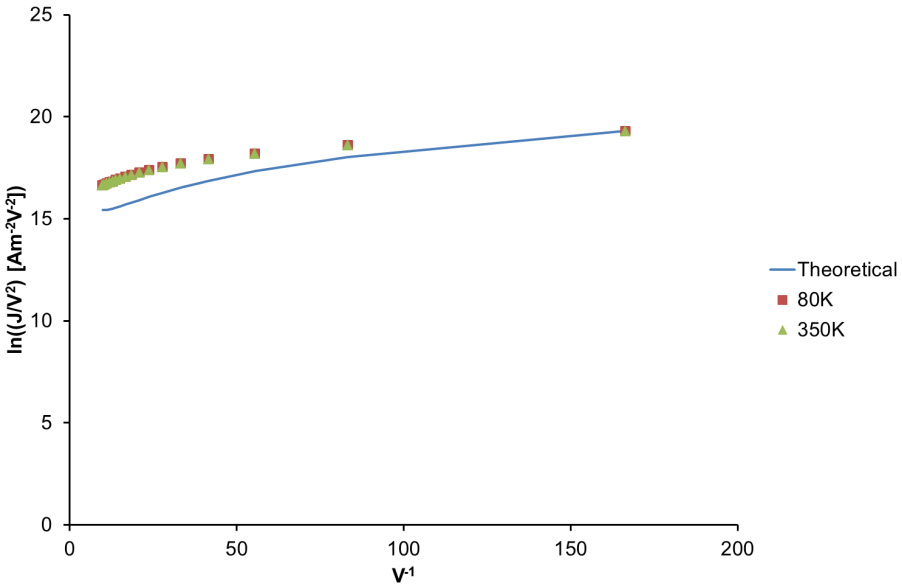

Figure 6.23 – *Graph showing $ln(J/V^2)$ versus $1/V$ to compare the theoretical direct electron tunnelling voltage dependence with the experimental results*

Conduction Mechanisms Conclusion

From the various mechanism comparisons shown, direct electron tunnelling could be deemed comparable, and this diminishes with voltage. This is for a 7.6 nm oxide, which is much thicker than the 5 nm limit state earlier. Therefore, it implies that a complex interaction between mechanisms is responsible for the effect seen in these devices, with perhaps a form of tunnelling occurring (either indirect tunnelling or direct tunnelling through a non-uniform thin defect region in the oxide) at low voltages, and a combination of mechanisms occurring at higher voltages.

6.3.4 AC Analysis and COMSOL

As previously discussed, N-type ⟨100⟩ silicon of 10 to 30 Ω cm resistivity was chosen as the initial substrate material (2” diameter wafers) and was oxidised to provide

an insulating 1000 Å film. However, upon initial AC testing for these devices, it became apparent that stray capacitances were present in the system, as modelled in COMSOL, and therefore borosilicate glass wafers were used as the preferred substrate.

A 3D COMSOL model was used to verify this, with a geometry produced, which replicated the contact pads and tracks of the devices, as seen in Figure 6.24. The electrostatics physics package was used to model the different dielectrics in the system: the substrate and the air, with the metal conductors being voids in the model, with a 1 V signal applied to the left contact (seen in red) and the right contact being grounded (seen in blue).

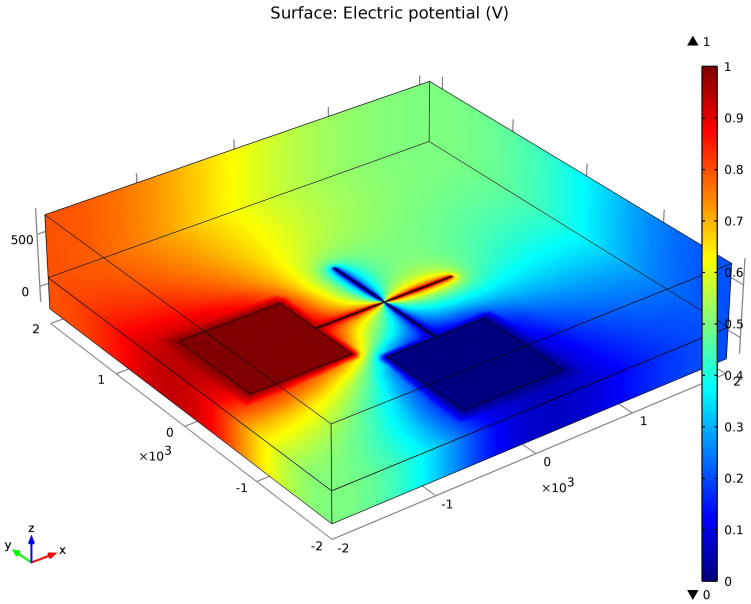

Figure 6.24 – *COMSOL simulation of contact pads*

A 200 nm gap was left between the anode track and cathode track (the crossover region wasn't included), as seen in Figure 6.25. The crossover region was omitted due to the relative size of the oxide layer (4 nm) compared to the size of the contact pads and tracks (measured in millimetres). These 6 orders of magnitude difference in dimensions resulted in a model which was too complex to solve with the computational power available. As a result, a simplified version of the diode (contact pads and track only) was used to give a qualitative comparison between an SiO_2 on silicon substrate and a borosilicate substrate.

In order to successfully model this system a custom mesh had to be used. This involved producing a free triangular mesh on the bottom of the contact pads and tracks, following by a free triangular mesh on the exposed substrate surface. These meshes were then swept down through the substrate, with a free triangular mesh being used on the top of the contacts and on a plane level with the top of the contacts, which was then swept upwards through the air domain.

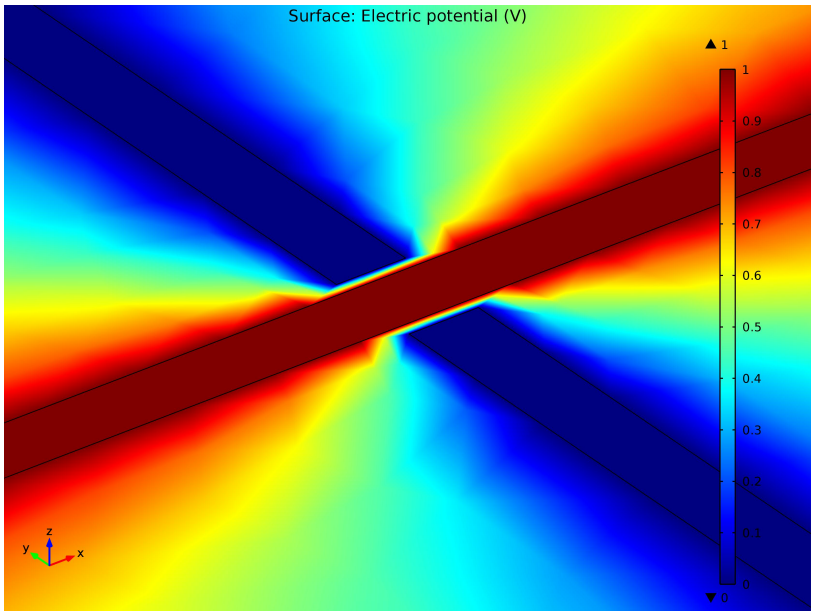

Figure 6.25 – *COMSOL simulation of contact pads - gap between contacts visible*

Due to the difference in relative permittivity between the SiO_2 and the borosilicate, the capacitances of the systems varied. The SiO_2 system had a global capacitance of 0.139 pF compared to the glass substrate system capacitance of 0.071 pF thus showing that this configuration of contacts has a greater capacitive impact on the system than the equivalent glass-based device. However, the results cannot be used quantitatively, as in the real device stray capacitances will be caused by a much smaller gap between the tracks, which will be as small as the oxide is thick, which cannot be modelled here, as discussed. It is believed that there are also stray conduction paths not only through the SiO_2 alone but through the oxide into the silicon substrate, which is conductive, and then back through the oxide again into the other track thus adding further parallel capacitances, as seen in Figure 6.26. By using just the glass substrate, the capacitances are reduced and provide results

which are more realistic.

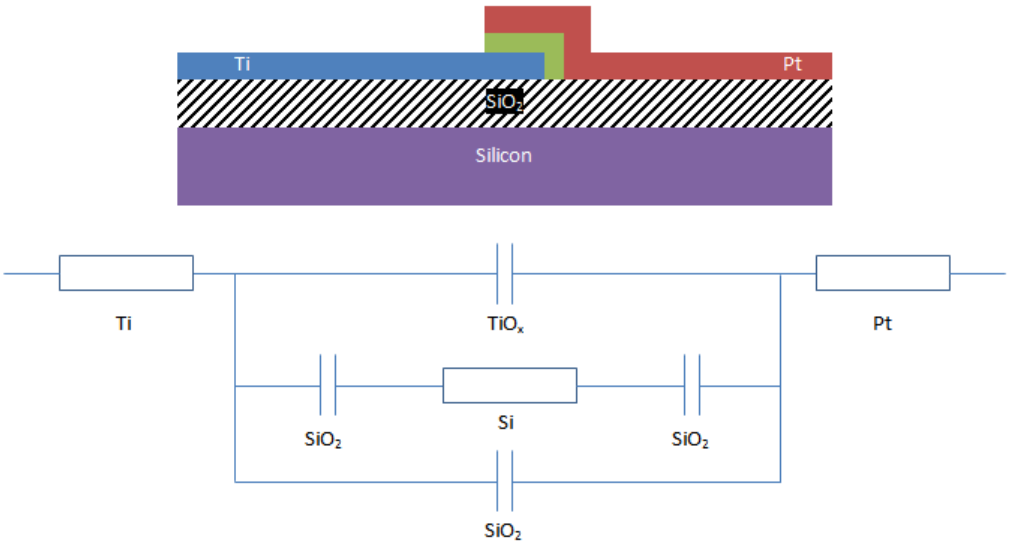

Figure 6.26 – *Diagram of side profile of crossover region - layers labelled, plus the TiO_x in green*

With the substrate choice confirmed, AC capacitance measurements could then take place. Figure 6.27 shows the capacitances for various 4 hour furnace diodes on a glass substrate, as tested on an impedance analyser. As can be seen the capacitances vary from 1.3 to 2.5 pF, which equates to a relative permittivity range of 11.5 to 26.5

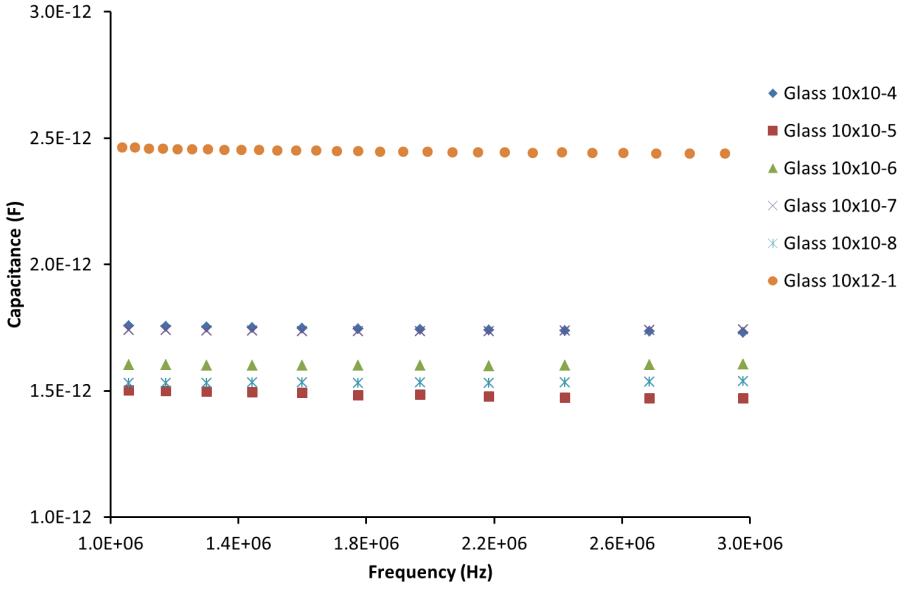

Figure 6.27 – *Capacitance graph for various 4 hour furnace diodes*

6.4 Failure Mechanisms

In order to fully appreciate the functionality of the fabricated diodes, it is also important to determine the main causes for their failure. Lifetime testing, current stressing and voltage breakdown tests took place to discuss the diodes weaknesses.

6.4.1 Current Stressing Results

Four triaxial probes were used to in turn connect the diode under test to the HP 4145B parameter analyser and then to an analogue signal generator. The I-V data from the diode was recorded, and then the probes were swapped over to the signal generator which was used to cycle the diode with a range of ±0.3 V for a given number of cycles at 10 to 60 Hz. The cycling was halted at intervals to allow an I-V measurement to be taken, and then this process was repeated for the desired number of cycles. The normalised current was then calculated and compared to previous results by Hoofring *et al.* [106], which can be seen in Figure 6.28.

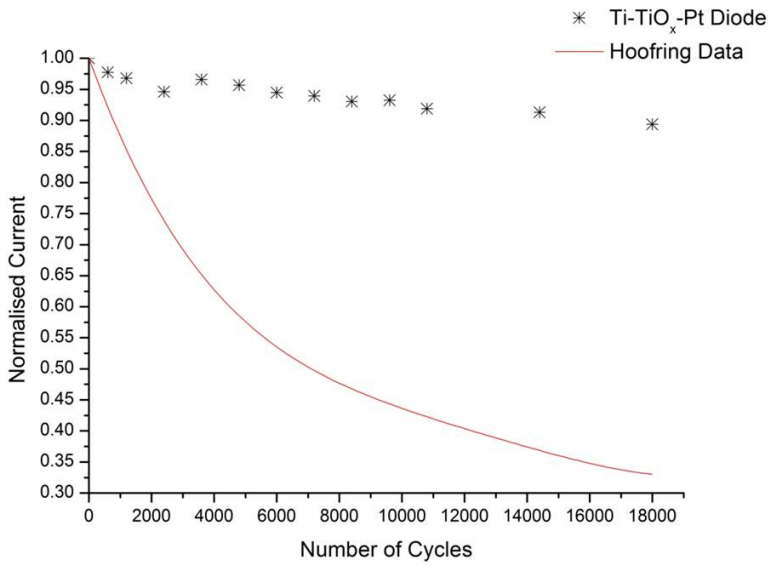

Figure 6.28 – *Graph showing the effects of current stressing on furnace diodes compared to diodes published by Hoofring et al.*

As can be seen, the furnace based diodes in Figure 6.28 show a 10 % drop in normalised current over 18000 cycles, compared to a 65 % drop in the Hoofring data, with the same frequency range and voltage levels compared to the breakdown

voltage of the diodes used, in order to ensure that the results could be compared. As can be seen our diodes appear to degrade less with cycling than those previously published.

Furthermore, preliminary testing has also shown that diodes which have been current stressed are more robust that those which have not. This involved finding two similar diodes and current stressing one, then performing a voltage sweep with sufficient voltages to destroy the diode. Those which had been current stressed appeared to have higher subsequent breakdown voltages. However, this is a difficult thing to test reliably, given the likelihood of finding two identical diodes.

6.4.2 Lifetime Testing

In order to fully decouple the effects of current stressing and age-based degradation, it was necessary to measure the I-V characteristics of a diode over time to note variation. Figure 6.29 shows the degradation of a Ti-Pt furnace diode over the period of hours without any additional external intervention. As can be seen there is a fivefold increase in resistance over that period. It is thought that this is due to the thickness of the platinum layer (here 30 nm) being sufficiently thin to allow the diode oxide to continue to be affected by atmosphere once fabricated.

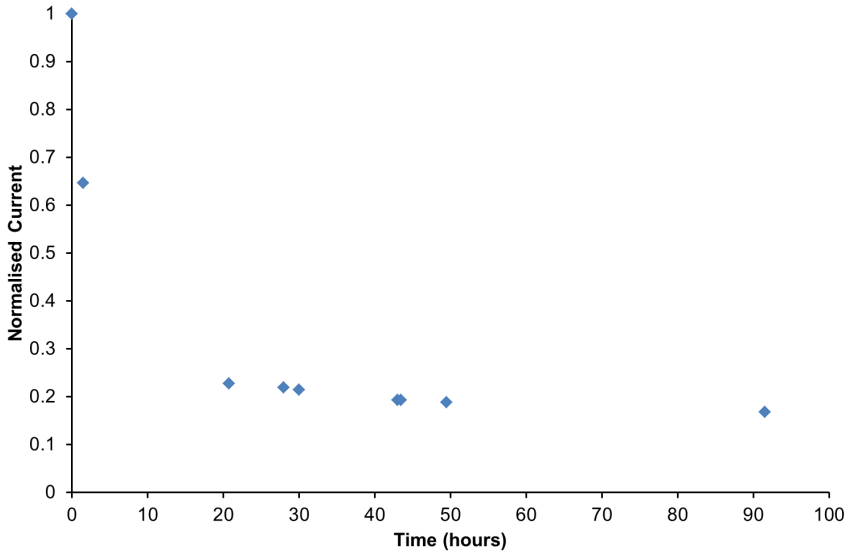

Figure 6.29 – *Graph showing the effects of time on the normalised current in a* $Ti/TiO_x/Pt$ *diode*

6.4.3 Effects of Static Discharge

It is worth noting that these diodes are extremely sensitive to static electricity and therefore anti-static precautions need to be in place to prevent significant yield problems. The fabrication and analysis environment is humidity controlled and all handling work is performed either on an antistatic mat or with the use of wrist straps. Furthermore, cleanroom clothing is washed in antistatic detergent as is the cleanroom floor, in order to try to minimise any static build up. All fabricated diodes are stored in conductive boxes. This effect is only a concern after the final platinum deposition.

6.5 Initial Diode Production Conclusions

MOM diodes using a Ti/TiO_x/Pt metallurgy, and a simple titanium oxidation technique, have been fabricated and tested. Initial diodes show DC electrical results of curvature coefficient, which are among the best published, as well as a high yield of working devices, despite the susceptibility of the diodes to static damage. It has also been shown that care must be taken when using data extracted from polynomial fits to quote results. Physical analysis of the titanium oxide shows that the oxide is thicker than our desired value and also not very uniform. Furthermore, the oxide layer actually consists of a number of different oxides, as confirmed by ToFSIMS. In order to produce a superior electrically functional diode the oxide must be thinner and of a higher quality. The conduction mechanism analysed proved inconclusive, with the variation of critical parameters affecting the results too severely to draw any definitive conclusions. However, the trends of direct electron tunnelling were compatible with the measured results in two separate voltage regimes and the devices were also temperature independent, thus implying that a tunnelling mechanism is occurring. The furnace diode production has established the Ti/TiO_x/Pt diode as a 'successful' diode, as well as acting as a vehicle for electrical and physical testing procedures.

Table 6.5 details the key parameters of the diodes discussed in this chapter.

Table 6.5 – *Diode summary*

Parameter	4 Hour Furnace Diode
Base Material	Titanium
Top Material	Platinum
Oxidation	Wet furnace oxide (4 hour 100 °C)
Oxide Thickness	6.9 to 7.6 nm
Diode Cross Section (typical)	$80\,\mu m^2$
Typical Peak Current Density	1 to $100\,A\,cm^{-2}$
Voltage Test Range	$\pm 0.3\,V$
Typical Curvature Coefficient (zero bias)	$3.1\,V^{-1}$
Best Curvature Coefficient (zero bias)	$6.8\,V^{-1}$
Current Ratio	1.7 to 3.5
Capacitance	1.3 to 2.5 pF
Relative Permittivity	11.5 to 26.5

Chapter 7

Oxide Layer Development

7.1 Introduction

In Chapter 6, furnace oxidised diodes were produced with electrical results, which were promising. However, the furnace oxide was too rough, too thick at 6.9 to 7.6 nm and non-uniform, which was confirmed via TEM analysis, as well as a significant variation in electrical results between diodes. A more controllable thinner oxide was needed. Therefore, in order to control the process on a refractory metal, we had to remove any existing uncontrolled oxide and then reoxidise the pure metal in a controlled manner. However, once exposed to atmospheric conditions, any stripped titanium would reoxidise natively immediately. Therefore, the oxidation must occur immediately after the native oxide is stripped, without exposing the metal to any atmospheric oxygen. A combined plasma etch/reactive ion etch (RIE/PE) system allowed this by swapping between modes without removing samples in the transition. The RIE mode was used to etch away the titanium, and then in-situ regrowth of the oxide occurs in the plasma mode. A 100 % O_2 gas concentration plasma initially produced promising but variable results, so instead the gas concentration was lowered to 50 % O_2 and 50 % Ar to improve the repeatability between devices.

7.2 100% Oxygen Concentration Results

7.2.1 Fabrication

In order to oxidise the titanium in a more controlled manner, the photoresist was removed after the gold etch step of the process described in Section 6.2.1 and the sample placed in an Oxford Instruments combined plasma etch/reactive ion etch (PE/RIE) system. Here the sample underwent an initial titanium etch process in RIE mode to remove any native oxide, which will have formed on the exposed titanium (100 W, 100 mT, 20 sccm CF_4, 2 sccm O_2 for 15 seconds in RIE mode). Without removing the sample from the vacuum, a plasma oxidation then took place in plasma etch mode, which resulted in an oxide forming in a controllable way on the surface of the titanium (100 to 150 W, 500 mT, 100 sccm O_2, for 5 minutes in PE mode). Droulers *et al.* [82] show that this process is power and not time dependent and hence the use of a power range for constant plasma times.

The mask design was also altered in order to reduce the amount of platinum being deposited on to the substrate with poor adhesion. Figure 7.1 shows the new design, where both sets of contact pads are made during the first titanium/gold deposition, with the platinum, seen as the horizontal line, only having to span a 10 µm gap between the exposed titanium and the wide gold contact pad.

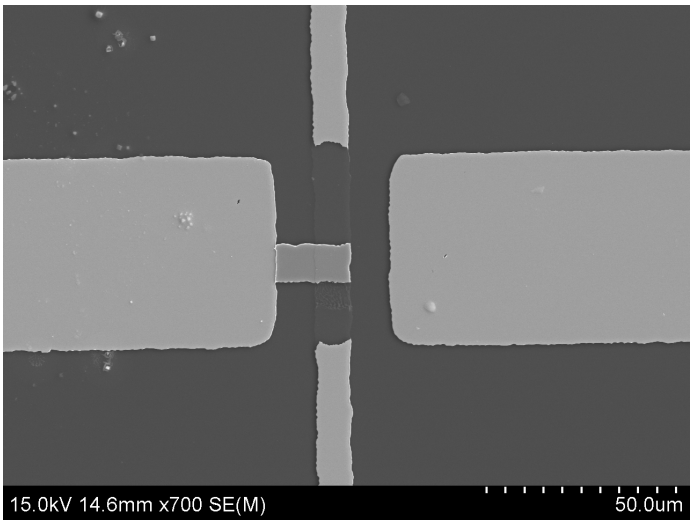

Figure 7.1 *– SEM image of adapted mask design - vertical line is a titanium/gold line, with central gold region removed to expose titanium, wide horizontal line is a gold contact and thin horizontal line is platinum to form the diode at the crossover*

7.2.2 Physical Analysis

In order to fully analyse and compare the two different oxidation techniques, ToFSIMS analysis was used to determine both the thickness and stoichiometry of the resulting oxides. Figure 7.2 shows the negative ion analysis of a 100% gas concentration plasma oxide. As can be seen, the oxide is not dominated by TiO_2, as suggested in [82], but rather by sub-stoichiometric TiO. In contrast to the previously discussed 4 hour furnace diode, seen in Figure 6.8, the PE is a comparatively simple oxide, as it is composed of fewer oxide stoichiometries.

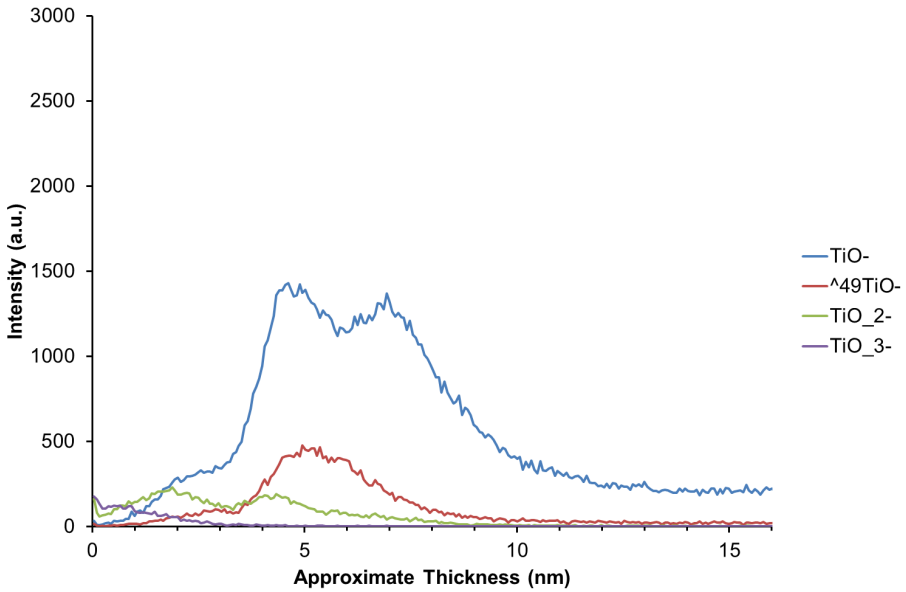

Figure 7.2 *– ToFSIMS analysis of composition of 100% O_2 gas concentration plasma oxide*

Figure 7.3 shows a profile of the TiO- ions in the following structures: 100 W, 110 W, 120 W and 150 W plasma diodes and a 4 hour furnace diode. As can be seen, there are two peaks present in the TiO- ion trace of the ToFSIMS analysis with a trough region in between them. This secondary, lower peak, which occurs away from the surface of the oxide, could occur for a number of reasons. The peak could be caused by a sputtering effect, whereby inconsistencies caused by the sputtering of the sample affect the intensity profile, which is unlikely in such a comparatively robust sample (more likely in organic samples). Finally, this second peak could be a real effect caused by the plasma oxidation process. The central trough region in

the TiO- trace occurs at the same time as a corresponding hydrogen peak, which could have been cause by hydrocarbon contamination in the RIE. While interesting, this second peak does not affect the comparison between the resultant trend in the oxide thickness, which has been confirmed via TEM analysis.

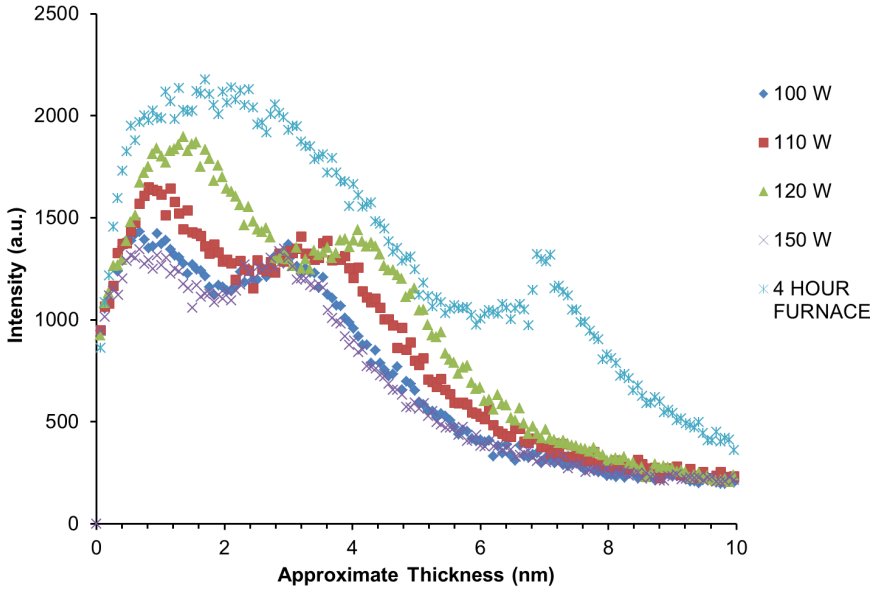

Figure 7.3 *– ToFSIMS analysis comparison between the TiO- ion of the furnace diode and plasma diodes*

Table 7.1 shows the numerical comparison of the oxide thicknesses. As well as comparing the two oxidation methods, the thickness of different power plasmas was of significant interest. An intensity half way between the peak intensity and the titanium baseline intensity was chosen as a suitable cut-off for comparison between the oxides. As can be seen, all of the plasma oxides are thinner than the furnace oxide (6.9 nm), and all are in the region of 5 nm or thinner, which provides an ideal range for conduction mechanism testing, with the aim of achieving electron tunnelling.

As was discussed in [82], the variation in oxide thickness in this process is determined by the plasma power rather than the time. Therefore, diodes were produced using a range of plasma powers, which resulted in a variation in oxide thicknesses. The thickness of the oxide can be controlled by the power of the plasma, resulting in the ability to tailor the oxide to the requirements of MOM diodes. It is noted (and repeatable) that the oxide thickness reaches a maximum with

plasma power, and then falls away with further power increases. One explanation is that this is due to the interaction of two simultaneous processes taking place during the plasma oxidation; the oxide growth and surface etching from the plasma bombardment. At low powers the oxidation dominates, with a range of powers causing thickness variations. However, beyond a certain threshold power, etching begins to dominate causing a sudden decrease in oxide thickness with any further power increase. The value of our process is in combining RIE with low power PE of a readily oxidisable metal (i.e. titanium) to etch and then regrow a thin oxide in a controllable manner.

Table 7.1 *– Numerical comparison between oxide thicknesses for different plasma diodes*

Oxide Preparation Method	Average ToFSIMS Measurement (nm)
100 W Plasma 100 % O_2	4.1
110 W Plasma 100 % O_2	4.6
120 W Plasma 100 % O_2	5.1
150 W Plasma 100 % O_2	4.0
4 hour furnace	6.9

The thickness measurements were confirmed by transmission electron microscopy (TEM) analysis, which also confirmed the improved uniformity of the plasma oxides, which can be seen in Figure 7.4. The TEM images shown are cross-sections of each of the diodes. Here, defects in the furnace oxide are evident in Figure 7.4 (left), whereas the uniformity of the PE oxide is apparent in Figure 7.4 (right). The electrical results of the furnace diodes exhibited a noticeable variation across a wafer [55], and it is believed that this was due to localised defects in the oxide. However, as can be seen in Figure 7.4, a smaller variation in oxide thickness should result in more uniform electrical results for the PE diodes; electrical tests suggest this to be the case.

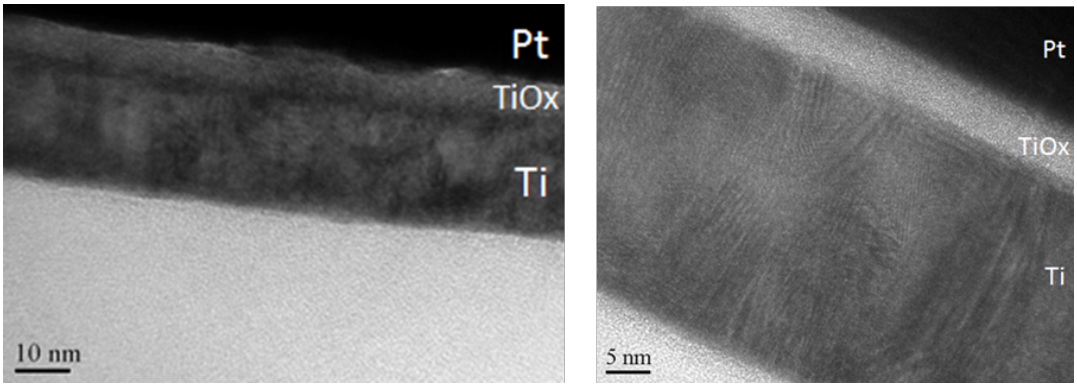

Figure 7.4 *– TEM image comparison between oxide in 4 hour furnace diode (left) and a plasma diode (right)*

7.2.3 Electrical Analysis

Although the physical analysis of the diodes suggests that a more suitable oxide had been found, this must be confirmed electrically. Table 7.2 shows a summary of the effect of varying power (and so thickness) on the zero bias curvature coefficient and the device yield. As can be seen, the yield, regardless of power, is low (c.f. 78 % in Figure 6.13). The curvature coefficient is also significantly lower than previous furnace diodes.

Table 7.2 *– Comparison of oxide thickness, curvature coefficient and yield for plasma diodes produced with different plasma powers*

Diode	Oxide Thickness	Average Curvature Coefficient	Yield
100 W	4.1 nm	$0.5\,V^{-1}$	9 %
110 W	4.6 nm	$0.4\,V^{-1}$	17 %
120 W	5.1 nm	$0.7\,V^{-1}$	25 %
150 W	4.0 nm	$2.1\,V^{-1}$	13 %

As a result of these preliminary electrical results and the promising physical results, it was decided that the power range over which the oxides could be produced was too narrow and therefore the oxygen concentration within the RIE

was reduced in order that the results were more distinct and repeatable, as discussed in Section 7.3.

7.2.4 Cryostat Testing and Conduction Mechanisms

In order to compare the performance of the plasma grown oxide to the furnace grown oxide, a cryostat was used to provide temperature based I-V measurements, as seen in Figure 7.5, and then conduction mechanism theory was compared to the results, the method of which was previously described in Section 6.3.3. The critical parameters for the theoretical fit were varied to attempt to find an agreement between theoretical values and experimental ones, with the chosen parameter values then analysed to determine if they are realistic. If the trends agree and the parameter values are realistic then the mechanism is deemed to be a feasible mechanism for conduction within the device.

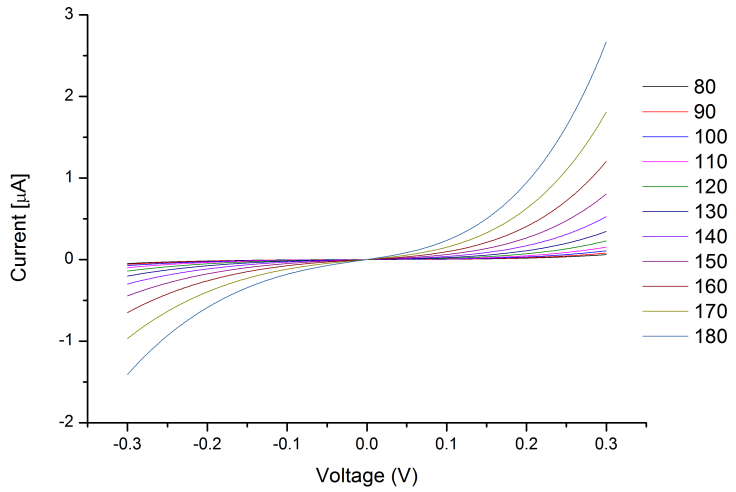

Figure 7.5 *– I-V characteristics of a typical plasma diode for a selection of temperatures*

The same data can be seen on a logarithmic scale in Figure 7.6. As can be seen, as was true with the furnace diode analysis, the current through the diode increases with increasing temperature and the I-V characteristic appears more linear with increasing temperature.

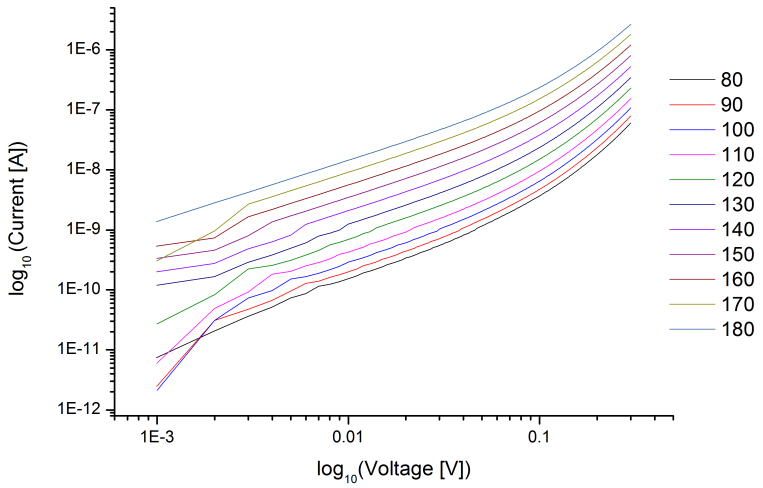

Figure 7.6 *– I-V characteristics (log scale) of a typical plasma diode for a selection of temperatures*

Schottky Mechanism

Table 7.3 shows the critical parameters for this analysis and their values.

Table 7.3 *– Critical parameters used for Schottky analysis*

Parameter	Description	Value
ϵ_r	Relative Permittivity	20
A	Area (measured)	$6.4 \times 10^{-11}\,\mathrm{m}^2$
d	Oxide Thickness (measured)	5 nm
ϕ_{bn}	Barrier Height	0.12 eV
m^*	Effective mass of electron	$2.39 \times 10^{-30} (2.62 * m_e)$

As can be seen, the permittivity, cross-sectional area and oxide thickness are realistic. The barrier height is low and the effective mass of an electron is taken from theory [62]. It is worth noting, however, that the relative effective electron mass can vary from 1 to 10 depending on the type of titanium oxide present [107] and given that the titanium oxide grown here has been proven to be a specific and

unique oxide this value could vary significantly. The resulting temperature plot can be seen in Figure 7.7.

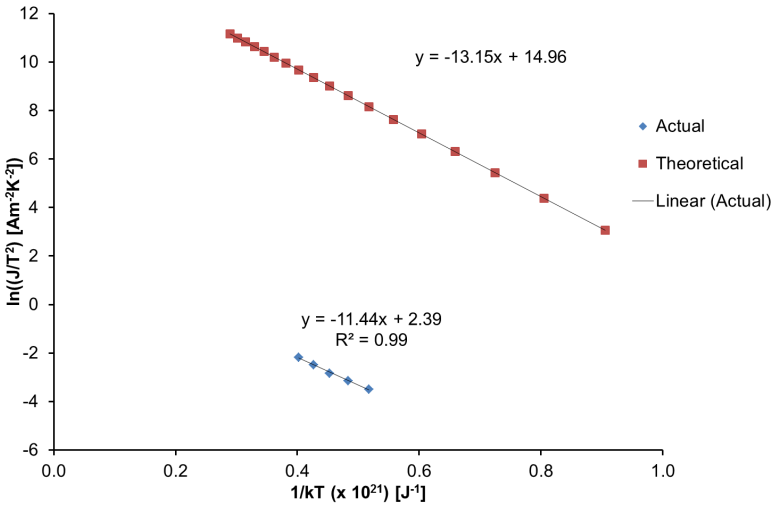

Figure 7.7 *– Graph showing $ln(J/T^2)$ versus $1/kT$ to compare the theoretical Schottky temperature dependence with experimental results*

The temperature plot shows that the gradients of the actual and theoretical values match, in that they are both very small. However, the intercepts disagree with 14.96 for the theoretical compared to 2.39 for the actual value. The gradient is determined by the effective mass of an electron as defined previously.

The Schottky voltage plot can be seen in Figure 7.8.

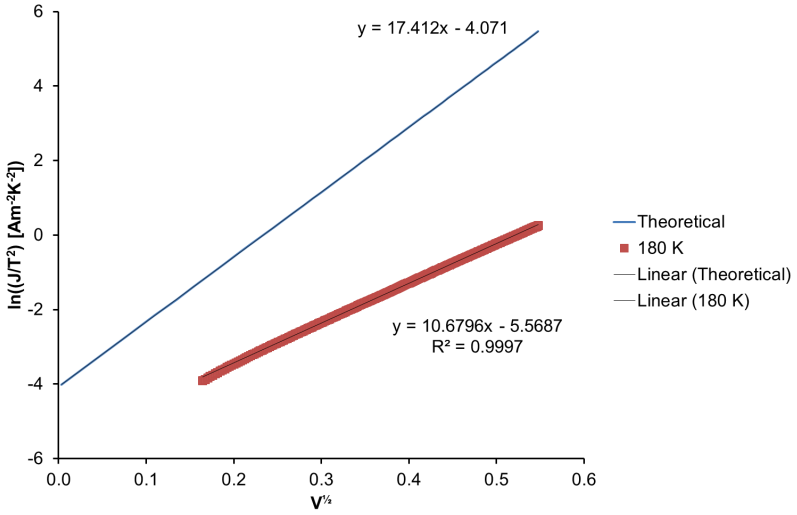

Figure 7.8 *– Graph showing $ln(J/T^2)$ versus $V^{\frac{1}{2}}$ to compare the theoretical Schottky voltage dependence with experimental results*

The voltage dependence of this diode more closely resembles the theoretical data, with similar gradient and intercept results. The gradient here is determined by the relative permittivity and the oxide thickness and the intercept is determined by the effective electron mass and the barrier height, all of which are either measured or theoretically determined. It is possible that Schottky emission is partially responsible for the conduction in this diode. However, the gradients of the temperature plot are very different and therefore even if it does play a part there is a more complex combination of mechanisms involved. It is also worth noting that the straight lines presented here are not the full range of data as the curves were not linear at voltage extremes.

Poole-Frenkel Mechanism

A summary of the critical parameters for this analysis can be seen in Table 7.4.

Table 7.4 *– Critical parameters used for Poole-Frenkel analysis*

Parameter	Description	Value
ϵ_r	Relative Permittivity	200
A	Diode Cross Sectional Area (measured)	$6.4 \times 10^{-11}\,\mathrm{m}^2$
d	Oxide Thickness (measured)	6 nm
ϕ_{bn}	Barrier Height	0.15 eV
μ_e	Electron Mobility in oxide	$1 \times 10^{-4}\,\mathrm{m}^2\,\mathrm{V}^{-1}\,\mathrm{s}^{-1}$
N_c	Density of States in oxide conduction band	$5 \times 10^{21}\,\mathrm{m}^{-3}$

The relative permittivity is high but still within the range specified by [73] and the barrier height is low, with the electron mobility and density of states estimated in order to provide as close a fit as possible. The Poole-Frenkel temperature plot can be seen in Figure 7.9. The oxide thickness has also been increased to 6 nm to improve the fit but this number does not agree with physical TEM and ToFSIMS

analysis.

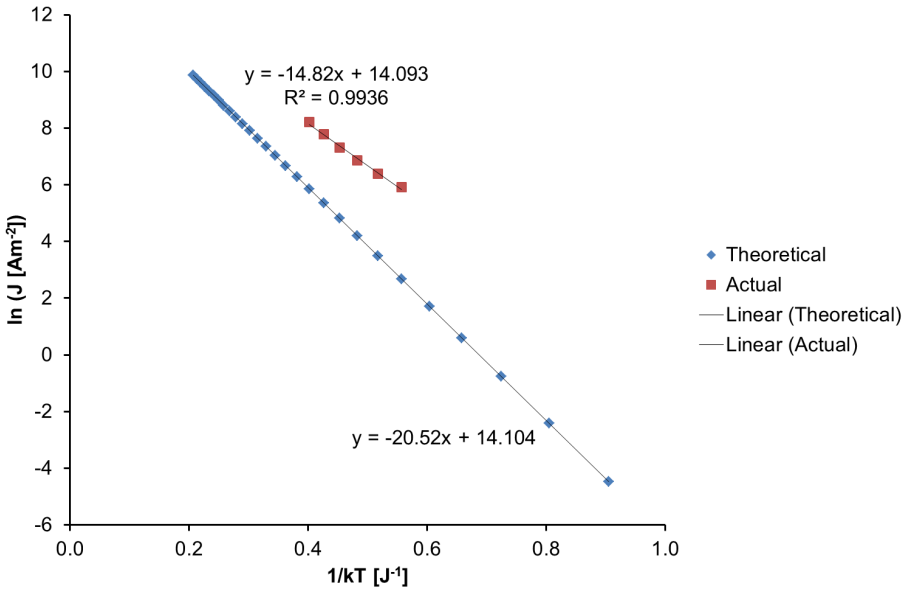

Figure 7.9 *– Graph showing ln(J) versus 1/kT to compare the theoretical Poole-Frenkel temperature dependence with experimental results*

The gradient and intercept of this plot are very similar, although the data range used is very small in order to obtain a linear fit. Both gradient and intercept are determined by the applied voltage, with the barrier height also affecting the gradient.

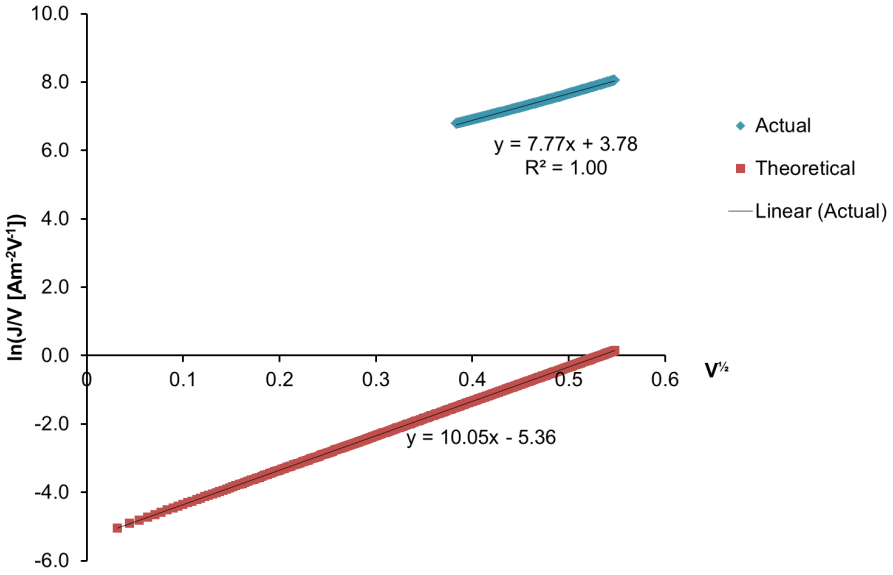

Figure 7.10 *– Graph showing ln(J/V) versus $V^{\frac{1}{2}}$ to compare the theoretical Poole-Frenkel voltage dependence with the experimental results*

Figure 7.10 shows the voltage plot. As can be seen, the gradient values are similar between actual and theoretical at 7.77 and 10.05 respectively. However the intercepts do not agree. The intercept is a complicated dependence on the barrier height and a logarithmic function of the carrier mobility, density of states and the oxide thickness and therefore finding a combination of all of the values which provides good correlations on both graphs is very difficult.

Fowler-Nordheim Mechanism

Table 7.5 shows the critical parameters for the comparison between the results and the Fowler-Nordheim theoretical line graphs.

Table 7.5 *– Critical parameters used for Fowler-Nordheim analysis*

Parameter	Description	Value
A	Diode Cross Sectional Area (measured)	$6.4 \times 10^{-11}\,\mathrm{m}^2$
d	Oxide Thickness (measured)	5 nm
ϕ_{bn}	Barrier Height	0.1 eV
m_{ox}	Effective Electron Mass in Oxide	$2.39 \times 10^{-30}\,\mathrm{kg}$
m_m	Effective Electron Mass in Metal	$2.39 \times 10^{-29}\,\mathrm{kg}$

For the tunnelling mechanisms, only one graph is plotted as these mechanisms are temperature independent. However, as seen in both Figure 7.11 and Figure 7.12, the 80 K and 180 K have different plots, thus showing a temperature dependence. This alone disproves tunnelling mechanisms as the sole conduction mechanism. This is also in contrast the the 4 hour furnace diode results, which showed the same curve at the different temperature extremes for direct and Fowler-Nordheim tunnelling plots.

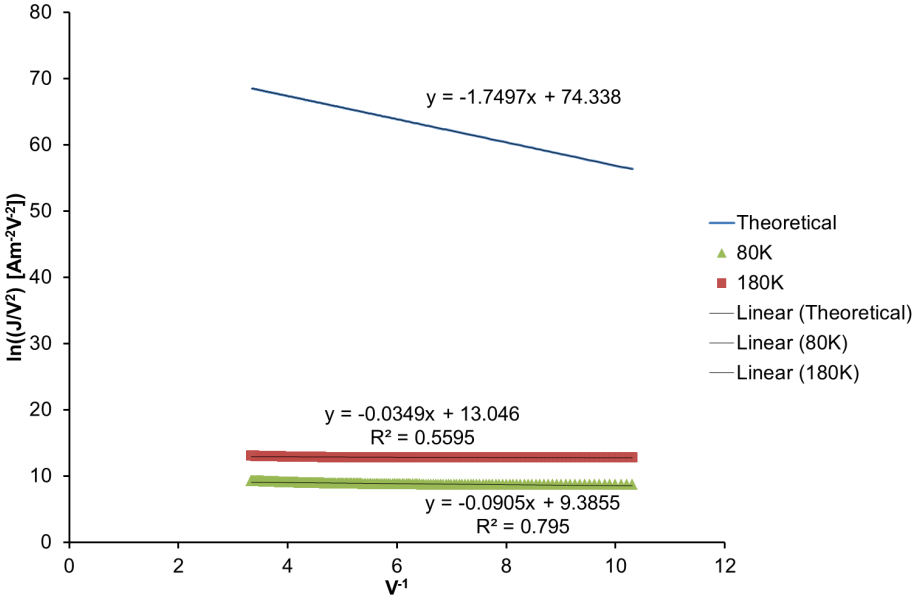

Figure 7.11 *– Graph showing $ln(J/V^2)$ versus $1/V$ to compare the theoretical Fowler-Nordheim voltage dependence with experimental results*

Direct Electron Tunnelling

Table 7.6 shows the critical parameters for the direct electron tunnelling analysis.

Table 7.6 *– Critical parameters used for direct electron tunnelling analysis*

Parameter	Description	Value
A	Diode Cross Sectional Area (measured)	$6.4 \times 10^{-11}\,\mathrm{m}^2$
d	Oxide Thickness (measured)	5 nm
ϕ_{bn}	Barrier Height	0.65 to 0.70
m_{ox}	Effective Electron Mass in Oxide	1.95×10^{-30} to 2.39×10^{-30}

The direct tunnelling equation does not produce a linear slope, resulting in the curve seen in Figure 7.12. The barrier height can be used to move the theoretical curve to match either the 80 K (barrier height = 0.65 eV) or 180 K (0.70 eV) but a further quantitative analysis cannot take place due to the non-linearity of the theoretical line. It is evident that there is a temperature dependent mechanism

involved in the conduction of this diode however. The barrier height is much higher than previously in order to try to improve the actual and theoretical fit, however this value is still a realistic barrier height.

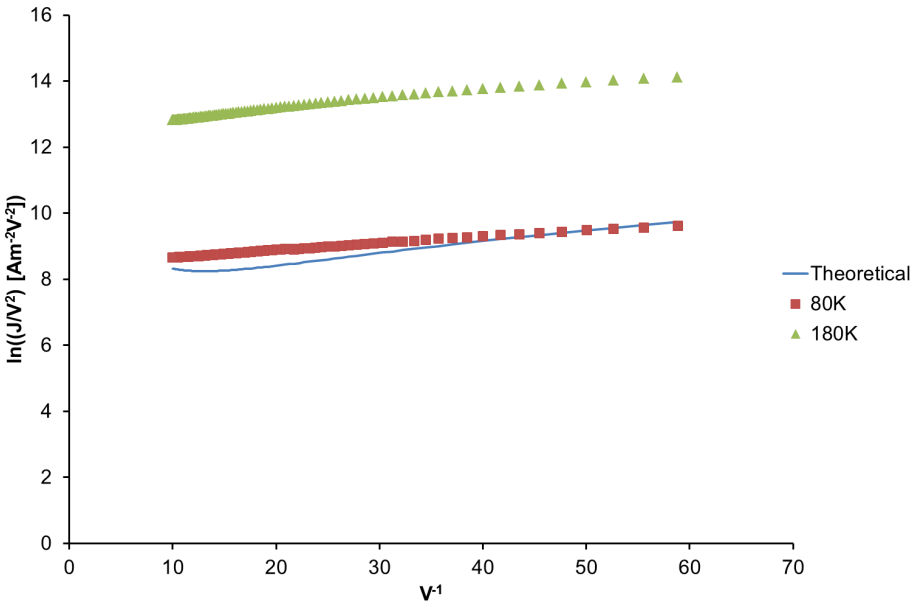

Figure 7.12 *– Graph showing $ln(J/V^2)$ versus $1/V$ to compare the theoretical direct electron tunnelling voltage dependence with experimental results*

By focussing on the low voltage regime for these fits, Figure 7.13 and Figure 7.14 show the fit for different barrier heights. Figure 7.13 shows the theoretical data compared to the actual data at 80 K, where a barrier height of 0.65 eV has been used.

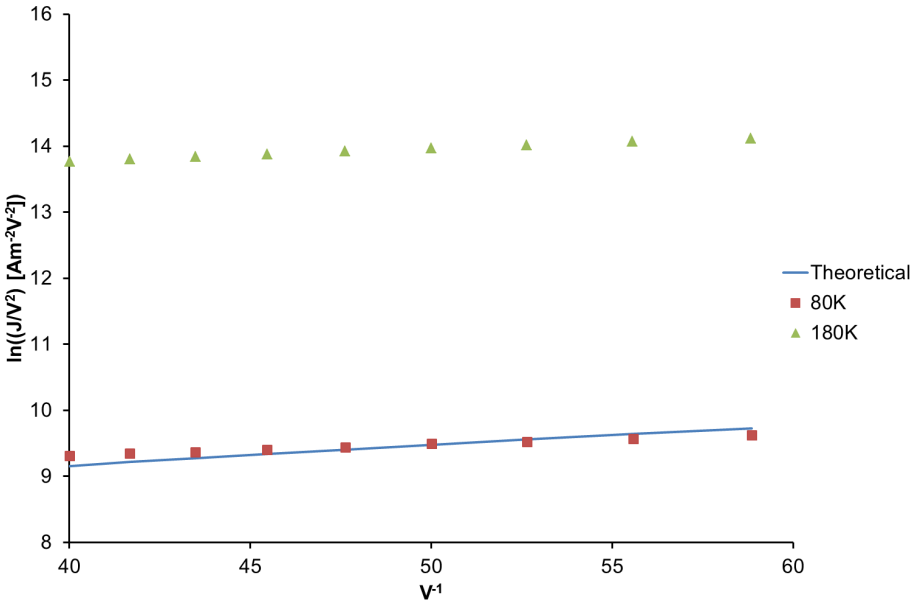

Figure 7.13 – *Graph showing $ln(J/V^2)$ versus $1/V$ to compare the theoretical direct electron tunnelling voltage dependence with experimental results at* 80 K

Similarly, Figure 7.14 shows the comparison between the theoretical line and the actual data collected at 180 K for an assumed barrier height of 0.70 eV

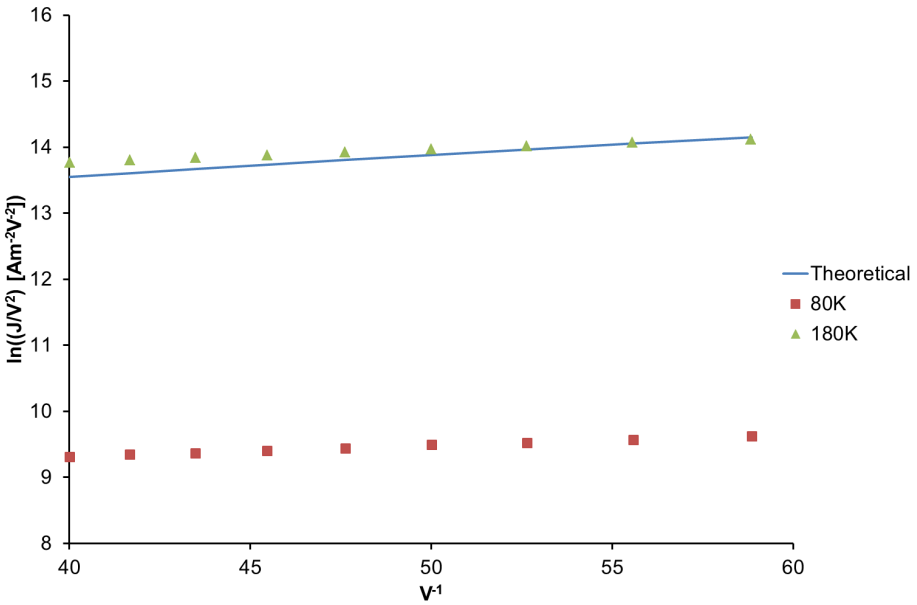

Figure 7.14 – *Graph showing $ln(J/V^2)$ versus $1/V$ to compare the theoretical direct electron tunnelling voltage dependence with experimental results at* 180 K

Both of these fits are very good, implying some form of electron tunnelling is occurring. However the fact that these two actual plots do not overlap shows

that there is a temperature dependence within the system and thus an additional mechanism must be contributing to the overall effect.

Conduction Mechanisms Conclusion

With the application of different parameter values, theoretical calculations can be made to agree with the experimental results. However, no definitive mechanism has been confirmed for the conduction through this diode. The main finding of this experiment was the temperature dependence of the I-V plots compared to the previous 4 hour furnace diode results, which showed no such dependence. The mechanisms involved are likely to be multiple in nature, and this is due to the different oxide structures between the furnace and plasma diodes, within each oxide there are different stoichiometric and physical structures.

7.3 50% Oxygen Concentration Results

7.3.1 Fabrication

As previously discussed, the 100 % oxygen concentration plasma growth of the oxide involves oxide thickness changes which depend on plasma powers which are too similar, so it was decided to gain additional control of the repeatability of the process. This was achieved using a reduced oxygen concentration within the plasma. The sample still underwent an initial titanium etch process in RIE mode to remove any native oxide which will have formed on the exposed titanium as above. The plasma oxidation then took place in plasma etch mode, which resulted in an oxide forming in a more repeatable and controllable way on the surface of the titanium (150 to 350 W, 500 mT, 50 sccm O_2, 50 sccm Ar for 5 minutes, PE mode). Furthermore, the newly oxidised titanium then underwent an annealing process, as is was discovered that this annealing step can improve the diode figures of merit by reducing the number of defects in the oxide [86, 89]. Further information on the effects of annealing on diode performance can be found in Section 7.3.3.

7.3.2 Physical Analysis

ToFSIMS analysis has been used to determine the thicknesses of the 50 % oxygen plasma diodes compared to the previous 100 % ones. As can be seen from Figure 7.15, 50 % O_2 diodes have a much more gradual variation in oxide thickness for various plasma powers. Furthermore, the peak thickness using this technique is thinner that the 100 % O_2 diodes.

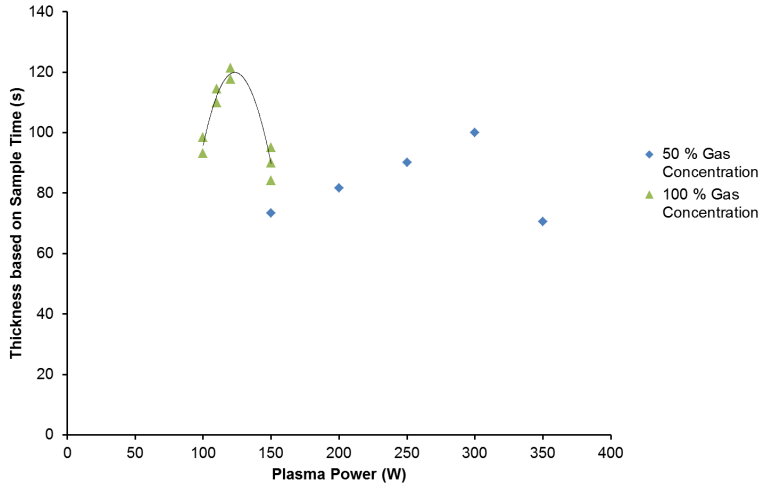

Figure 7.15 – *ToFSIMS comparison between* 100 % *oxygen plasma diodes (green) and* 50 % *oxygen plasma diodes (blue) (line is for visual guidance)*

Table 7.7 – *Numerical comparison between oxide thicknesses*

Oxide Preparation Method	Average ToFSIMS Measurement (nm)
150 W Plasma 50 % O_2	3.1
200 W Plasma 50 % O_2	3.4
250 W Plasma 50 % O_2	3.8
300 W Plasma 50 % O_2	4.2
350 W Plasma 50 % O_2	2.9
250 W Plasma 50 % O_2 (bake)	3.2

Based on the oxide thicknesses found, I-V testing and the earlier result that a slightly thicker oxide results in a higher curvature coefficient, the 300 W plasma oxide was used hereafter as the chosen oxidation method for diode fabrication. A thinner oxide would be preferred for lower resistance operation, however, 4.2 nm still has the ability to conduct via tunnelling and was therefore chosen.

The last row in Table 7.7 shows the thickness of a 250 W sample which had been annealed prior to analysis. As can be seen this annealing process actually reduces the oxide thickness, thus implying that the structure of the oxide has been changed by this process to make the insulator more dense.

TEM was used to confirm the oxide thickness measurements from the ToFSIMS analysis. Figure 7.16 shows a 4.2 nm uniform oxide film, which agrees exactly with the ToFSIMS results, which confirms the uniformity and repeatability of this oxide, compared to the furnace oxidised diodes, where the thickness was measured with a thickness range of 6.9 to 7.6 nm.

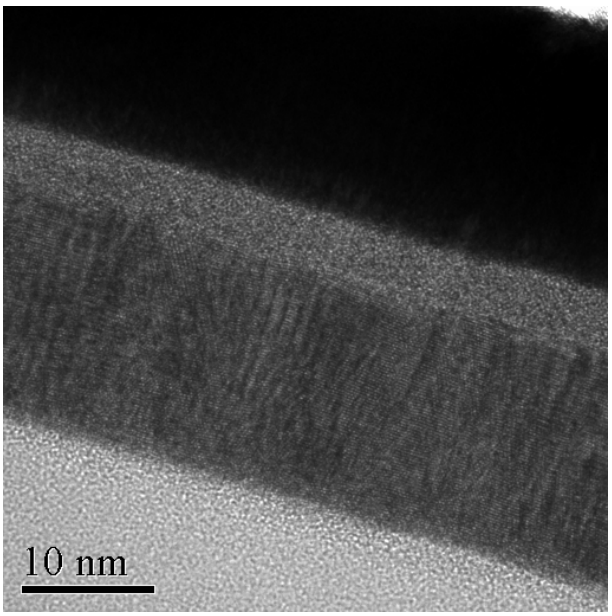

Figure 7.16 – 300 W 50 % *O_2 diode - from bottom to top: SiO_2 substrate (light grey), titanium, titanium oxide and platinum (black)*

7.3.3 Oxide Annealing

In order to improve the characteristics of the central oxide layer, annealing was investigated as previous works have shown that a titanium oxide layer can be

altered through the application of heat [69, 90]. In order to investigate the effect of thermally annealing the oxide layer prior to depositing platinum and completing the diode, devices were produced which had been annealed at different temperatures in a pure nitrogen environment. By annealing in a pure nitrogen environment, it ensures that further oxidation does not occur. Diodes were fabricated as discussed but immediately after the RIE oxidation, an anneal step took place, with the temperature varying. 50 °C, 100 °C, 150 °C, 200 °C, 250 °C, and 300 °C were tested and their results compared. As can be seen from Table 7.8 the set temperature and actual peak temperature varied due to the nature of the programmable furnace used.

Table 7.8 – *Desired and actual anneal temperatures*

Anneal Set Temperature (°C)	Peak Anneal temperature (°C)
50	78
100	139
150	154
200	225
250	295
300	316

Despite this, the results presented will use the set temperature to distinguish between the samples, e.g. W100 would refer to the wafer with a set temperature of 100 °C, but it was actually annealed up to 139 °C. Critical parameters were compared between the different temperature samples in order determine the effects of anneal temperature, as discussed in [88], which suggests that anneal temperature improves curvature coefficient up to a threshold point, after which the diodes are damaged by this process. As can be seen from Table 7.9, a similar effect is determined here, in that the W250 and W300 samples have significantly inferior figures of merit

values compared to the lower temperature samples. However, there is no discernible trend prior to that point, thus proving that, despite having better results than non-annealed diodes, the diodes up to threshold point are not heavily affected by the temperature they are annealed at. The findings in [88] are based on nickel/chromium junctions with a threshold of 350 °C, with the change in materials perhaps explaining the change in threshold point. Table 7.9 shows the average values for curvature coefficient and current ratio with the standard deviation in those results shown in brackets. It is also worth commenting on the current density values shown. This value is an average of the successful diodes on the associated wafer but the standard deviation of the current density is often high. This is most likely caused by cross-section area measurement inaccuracies.

Table 7.9 *– Comparison between diodes with different anneal temperatures*

Diode	Highest CC_{ZB} (V^{-1})	Average CC_{ZB}(V^{-1})	Average Current Ratio	Average Current Density ($A\,cm^{-2}$)
W50	4.6	3.4 (0.6)	1.8 (0.2)	119
W100	3.9	3.0 (0.2)	1.7 (0.2)	46
W150	3.5	2.6 (0.5)	1.5 (0.2)	183
W200	4.6	3.4 (0.8)	1.8 (0.3)	45
W250	2.2	1.6 (0.3)	1.2 (0.1)	53
W300	2.0	1.4 (0.3)	1.2 (0.2)	256

Furthermore, [88] shows that the surface roughness of the sample varies with annealing temperature, which may be an issue in diode production as roughness will reduce the repeatability of the devices produced. However a 100 °C annealed oxide has a roughness of 0.57 nm, which is comparable with all diodes annealed below the threshold point. By contrast, Figure 7.17 shows an example of an oxide which has been annealed above the threshold temperature at 300 °C, which is rougher at 1.12 nm, so much so that visual inspection can be used to notice the difference. These diodes have significantly worse electrical results.

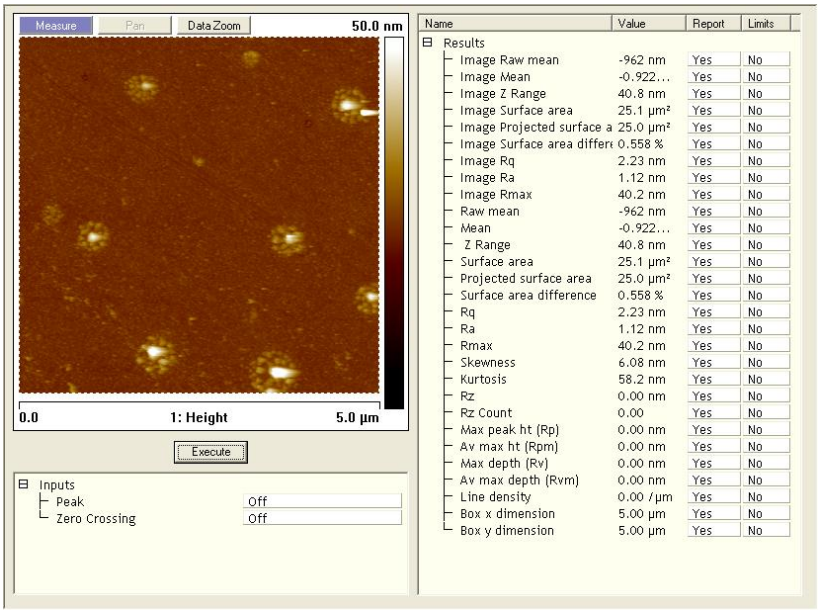

Figure 7.17 *– W300 AFM roughness - localised rough regions can be seen, which only appear on oxides annealed above the threshold temperature*

Based on these results it is apparent that an anneal step restructures the oxide in such a way that it performs better in a rectifying diode structure as long as it is below the threshold point. Therefore, all subsequent discussions will include this anneal step in the fabrication process. It is also worth noting the local peaks on this AFM analysis which have been caused by the anneal step. These local peaks will be affecting the overall roughness calculation but occur in isolated regions, which could mean that some small diodes do not contain such a defect, whereas others will.

7.4 Reduced Size Diodes

Once the fabrication process had been refined, new smaller sized diode devices were produced using a higher resolution laser cut mask set. This mask set incorporates coplanar wave-guide based diodes which could be tested using GSG probes and a VNA at high frequencies, as seen in Figure 5.8 with feature sizes down to 1 µm. The diodes were fabricated using a 300 W 50 % plasma and a subsequent anneal at 150 °C.

7.4.1 DC Analysis

Table 7.10 shows a summary of the curvature coefficient, current ratio and average current density information for the reduced size 50 % O_2 diodes created with the reduced size mask set (with the standard deviation shown in brackets). As can be seen the average curvature coefficient is higher than previous diodes, as is the current ratio. Furthermore, the current density is on average lower than previous average current densities, which is consistent with the previous findings that a lower current density results in better curvature coefficient results. A full diode summary can be found in Table 7.13.

Table 7.10 *– Diode summary*

Parameter	Value
Average Peak CC_{ZB} (V^{-1})	10.6 (1.9)
Average CC_{ZB}(V^{-1})	3.9 (0.9)
Average Current Ratio	2.1 (0.2)
Average Current Density ($A\,cm^{-2}$)	8.9 (5.4)

Figure 7.18 shows a typical J-V curve for these diodes, displaying the significantly lower current density compared to previous results. As before, a 9th order polynomial was fitted to this curve and this curve was then used to calculate the resistance and the curvature coefficient of the diode at each voltage.

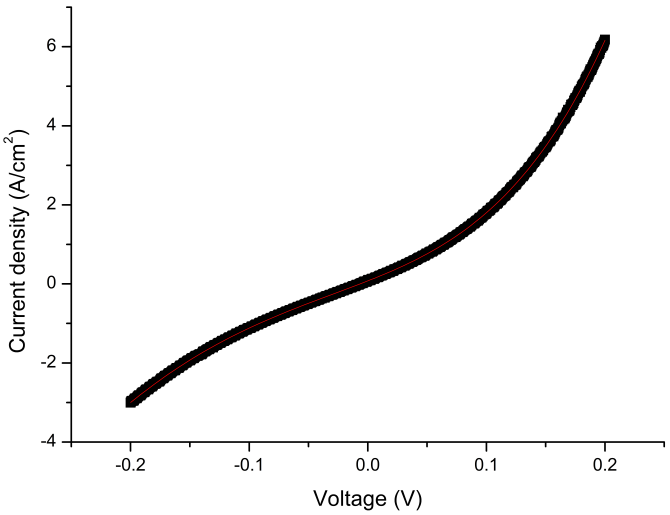

Figure 7.18 *– A typical J-V for the reduced size diodes*

Figure 7.19 shows the resistance of the same diode, which has been found using the 9th order polynomial curve fitting technique, which was discussed previously, in Figure 7.18, and taking the inverse of the first derivative of this best fit curve to provide the resistance data. The asymmetry of this diode is clear from this graph, with the peak being at slightly below 0 V.

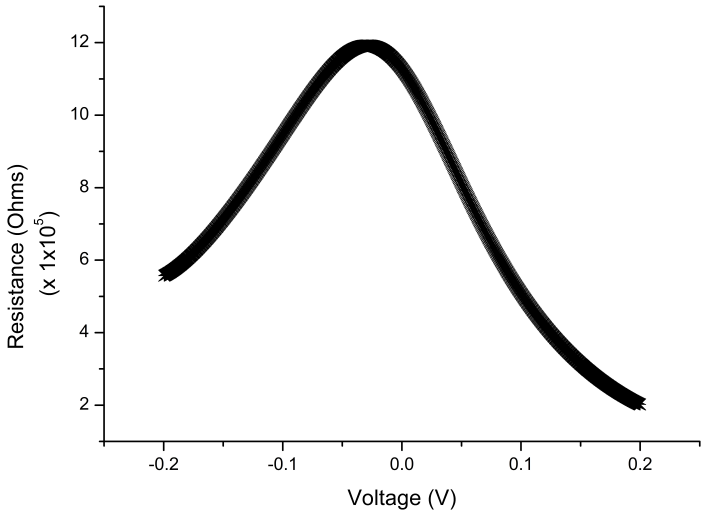

Figure 7.19 *– A typical R-V for the reduced size diodes*

Figure 7.20 shows the first derivative, or conductance, graph for the diode, which

is an inverse of Figure 7.19. As previously discussed, work by [70] discusses the use of the conductance graph to gain an insight into the nature of the device under test. It was previously believed that the offset of the minimum point of this graph from zero was simply due to the asymmetry of the graph, however [70] investigates whether the physical barrier structure can result in this offset, based on different barrier shapes. They showed that the conductance minimum only occurs at the origin for symmetric barriers. Furthermore, while small offsets (approximately 50 mV) can be explained by barrier asymmetry, larger offsets (approximately 250 mV) cannot be the result of barrier asymmetry and must therefore be due to other things, such as oxide defects and impurities. Here the conductance minimum is at −29 mV, which is significantly lower than the 50 mV discussed thus implying that the boundary is not dominated by defects. However, the materials being used here are significantly different from [70], which will affect the direct comparison of these findings.

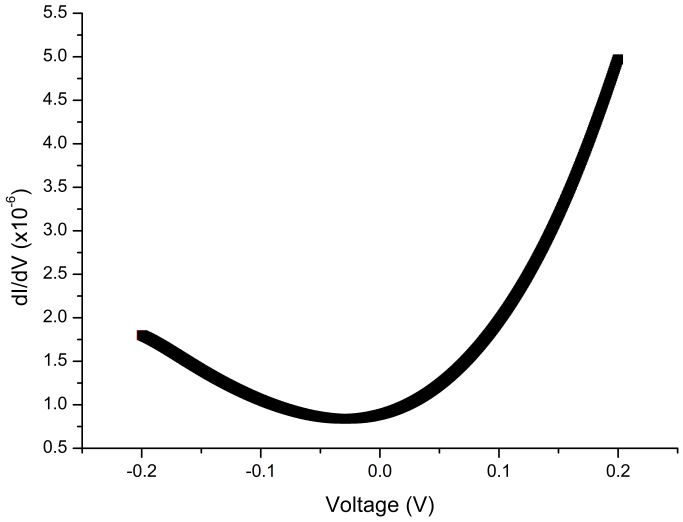

Figure 7.20 *– A typical conductance plot for the reduced size diodes*

Figure 7.21 shows the curvature coefficient for the same diode, which is the second derivative of the I-V best fit curve multiplied by the resistance (seen in Figure 7.19). Given the desire to operate these diodes at zero bias, the aim is to have the curvature coefficient peak as close to 0 V as possible, i.e. the diode to be at its most non-linear in the regime it will be used in. Here the peak is closer to 0.5 V but there is still a

significant zero bias curvature and a clearly visible asymmetry.

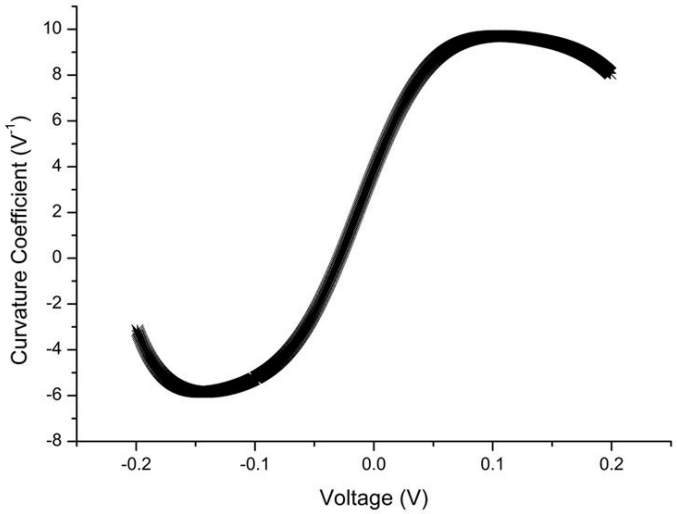

Figure 7.21 *– A typical CC-V for the reduced size diodes*

These diodes show promise based upon their DC measurements but more conclusive experiments must take place to confirm the capabilities of these diodes, in the form of AC measurements.

7.4.2 AC Analysis

The diodes were AC tested using a VNA, as described in Chapter 5. Each device underwent both a power and frequency sweep. The power sweep took place in the range -5 to 0 dBm at 10 MHz and the frequency sweep took place in the range 300 kHz to 3 GHz at 0 dBm. Table 7.11 shows a summary of the VNA data findings (with the standard deviation shown in brackets).

Table 7.11 *– Summary of critical parameters from VNA testing*

Parameter	Value
Capacitance [F]	1.8×10^{-13} to 2×10^{-12}
Voltage Responsivity [$\mathrm{V\,W^{-1}}$]	30.9 (5.1)
Current Responsivity [$\mathrm{A\,W^{-1}}$]	9.6×10^{-4} (5.96×10^{-4})
Area Range [μm^2]	0.7 to 48.9
Cut off Frequency Range [Hz]	1.45×10^{7} to 5.00×10^{8}
Relative Permittivity Range	9.9 to 32.3

As can be seen these smaller diodes have a comparable relative permittivity range with the previous results, showing that the anneal step does not significantly affect the relative permittivity. The cut off frequency was calculated by multiplying the maximum voltage of each trace by $\frac{1}{\sqrt{2}}$.

It would also be expected that the cut off frequency and cross-sectional area would have a strong negative correlation, according to Equation 4.15 and Equation 4.16. However, the error associated with taking the frequency measurements seen in Figure 7.22 is significant. Furthermore, measuring the cross-sectional area of these diodes is also difficult to do accurately.

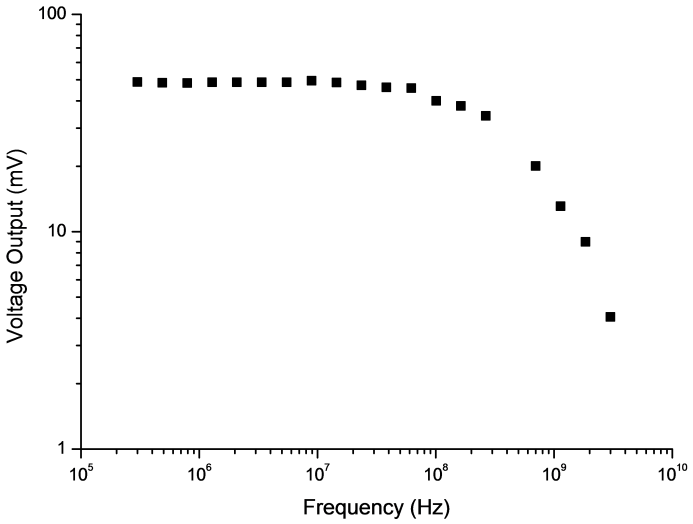

Figure 7.22 *– A typical V-f graph for small size diodes*

A typical power graph, used to calculate the voltage and current responsivity can be seen in Figure 7.23. The power in decibels was converted to milliwatts using Equation 7.1

$$P_{mW} = 10^{\frac{P_{dBm}}{10}} \tag{7.1}$$

where,

P_{dBm} = power [dBm]

P_{mW} = power [mW]

This milliwatt power was then used to plot a voltage and current versus power graph for each device, as seen in Figure 7.23. The gradient of the two lines in the graph equates to the rate of voltage output per power input, i.e. the responsivity, as seen in Equation 3.3.

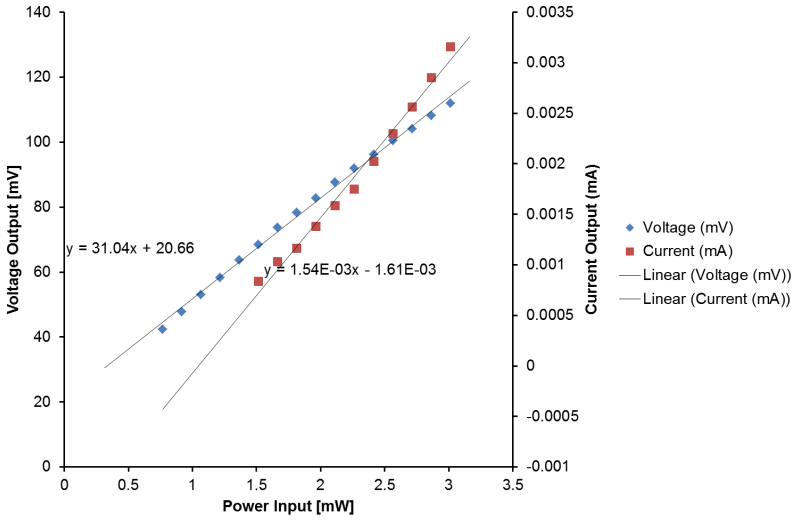

Figure 7.23 – *A typical responsivity graph for small size diodes*

The capacitance of each device was also retrieved from the VNA using the interface program. A typical capacitance graph can be seen in Figure 7.24.

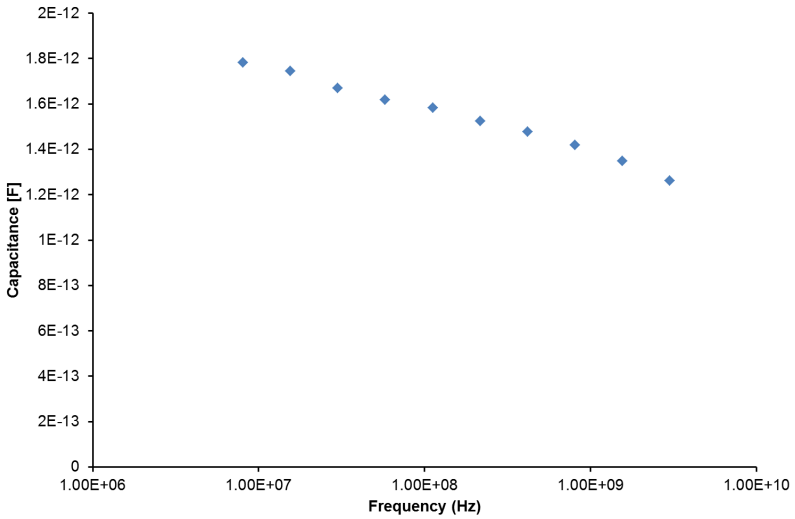

Figure 7.24 – *A typical C-f graph for small size diodes*

7.4.3 Matlab Simulation

In order to compare the DC experimental results and the VNA results and to determine their validity, a Matlab simulation was used, which took the polynomial coefficients of the 9th order polynomial fit from the DC I-V analysis and simulated the expected current and voltage responsivity for a given power input. By simulating

the VNA results and comparing them with the experimental results, the validity of those experimental results could be verified.

Firstly, a function was created which can return the average DC current output from a rectifying system. The output voltage from the system will be a combination of the AC input signal, $V_0.cos\omega t$, and the rectified DC signal, V_{DC}. Therefore, the output signal can be defined by Equation 7.2

$$V_D(t) = -V_{DC} + V_0.cos\omega t \tag{7.2}$$

This input was then simulated for one full oscillation of the sinusoid waveform, and then the I-V characteristics determined using the polynomial coefficients from a previous analysis of experimental results, as seen in Equation 7.3

$$I_D(t) = f(V_D(t)) = a_0+a_1.V+a_2.V^2+a_3.V^3+a_4.V^4+a_5.V^5+a_6.V^6+a_7.V^7+a_8.V^8+a_9.V^9 \tag{7.3}$$

The average current can then be determined from this. This function was then used in a Matlab program which, for a given power range equal to the VNA power range of the tested diodes, calculated the DC voltage output for an average DC current of zero. The input AC voltage across the diode was previously derived in Equation 5.7, but as these devices are not impedance matched to 50 Ω as previously described, Equation 5.7 is adapted by a factor of 2, as seen in Equation 7.4.

$$V_{0(rms)} = 2\sqrt{2.R_A.P} \tag{7.4}$$

This input voltage was then input into the Matlab function, which returns the DC voltage at which the current is zero, for a given input AC voltage of $V_0(rms)$. The DC current is also returned for a zero DC voltage. Therefore, both the voltage and current responsivity could be calculated from voltage-power and current-power graphs respectively and compared with the actual results.

Figure 7.25 shows a typical responsivity graph from a plasma diode fabricated in a 300 W 50 % oxygen plasma and subsequently annealed at 200 °C, tested between

−5 to −1 dBm.

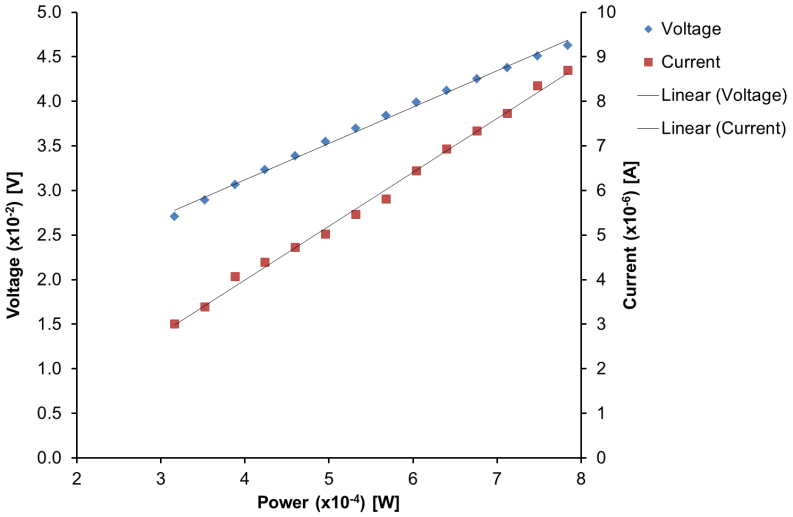

Figure 7.25 – *Typical VNA diode responsivity graph*

The trendlines fitted to these results provide an estimation of the voltage and current responsivities. The voltage responsivity is 38.7 V W^{-1} and the current responsivity is 13 mA W^{-1}. Figure 7.26 and Figure 7.27 show the Matlab simulations of these curves, as calculated from the polynomial curve fitting of the I-V characteristics of the same diode, with the actual simulated data show in blue and the straight line trend used for responsivity calculations shown in green. Figure 7.26 shows the DC output voltage varying in the range 20 to 45 mV compared to the actual results varying in the range 27 to 46 mV for the same applied input power. The simulated voltage responsivity is 48.7 V W^{-1}, which was calculated using the trendline visible in Figure 7.26. The fit of this line could explain the difference in responsivities between the actual and simulated results.

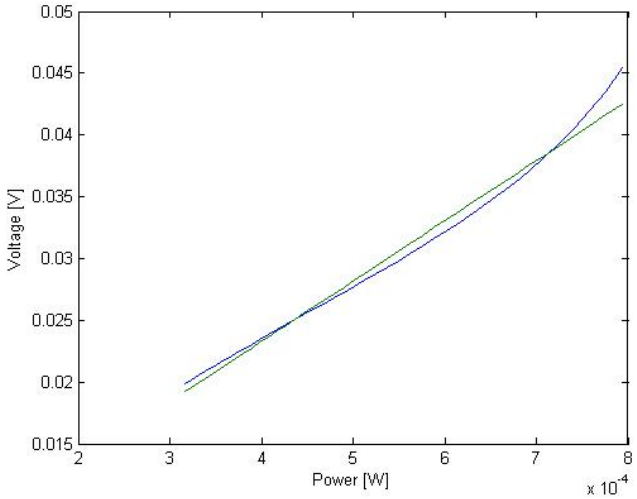

Figure 7.26 *– Matlab Simulation of a typical V_{out} Vs P_{in} graph*

Figure 7.27 shows the current-power graph simulated in Matlab for the same diode. The output current varies in the range 2.8×10^{-6} to $8 \times 10^{-6}\,\mathrm{A\,W^{-1}}$, compared to 3.0×10^{-6} to $8.6 \times 10^{-6}\,\mathrm{A\,W^{-1}}$. The current responsivity of the simulated results is $11.4\,\mathrm{mA\,W^{-1}}$, comparable to the experimental values of $13\,\mathrm{mA\,W^{-1}}$.

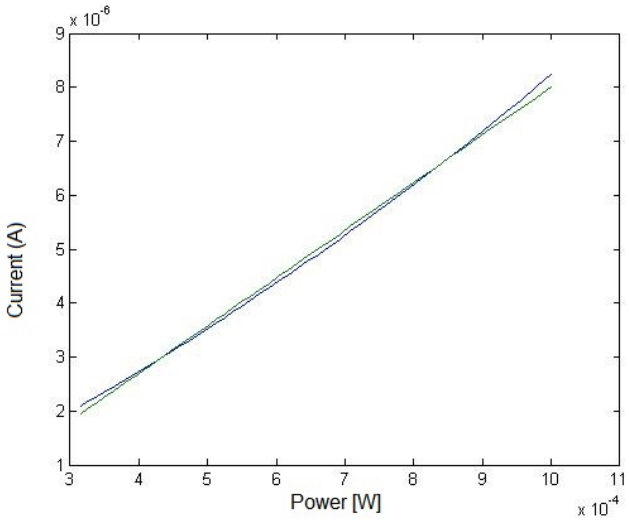

Figure 7.27 *– Matlab Simulation of a typical I_{out} Vs P_{in} graph*

This simulation could be used in future to predict the most suitable diodes for AC analysis, based solely on the DC results. However, it must be ensured that the polynomial fit to the I-V curve is accurate in order to ensure reliable prediction of the AC results. Furthermore, this simulation was also used to perform a power

calibration on the VNA, as it was discovered that the results varied consistently by 6 dBm. Therefore, this variation is accounted for in the Matlab software.

7.4.4 Phase Shift Lithography

As described in Chapter 5, phase shift lithography can be used to produce lines in the 200 to 400 nm range. Figure 7.28 and Figure 7.29 show SEM images of these phase shift lithography based lines incorporated into diodes, with a 10 µm common connection overlapped by phase shifted platinum lines, which have been shortened via the etching of a sacrificial chromium layer.

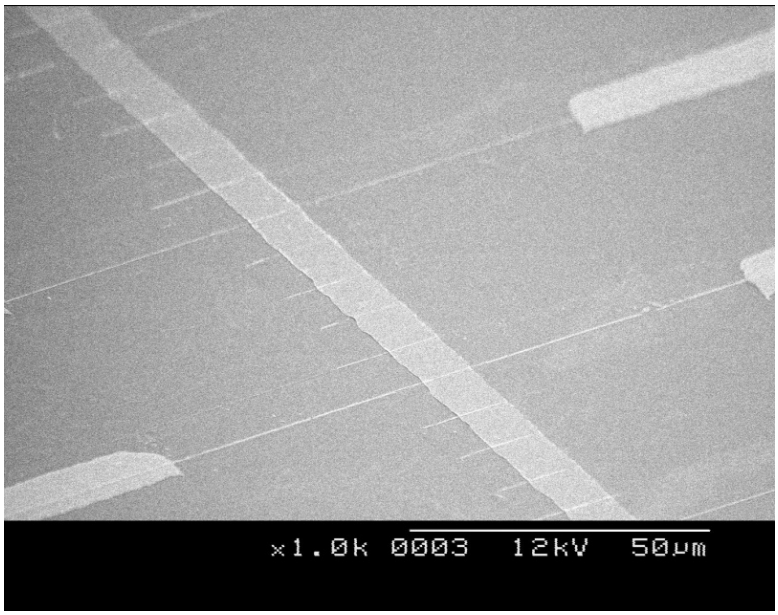

Figure 7.28 – 400 nm x 10 µm *diode produced using phase shift lithography*

These images combined with electrical results show the process to be robust, with phase shifting still occurring at the interface of the existing steps height for the contact pads.

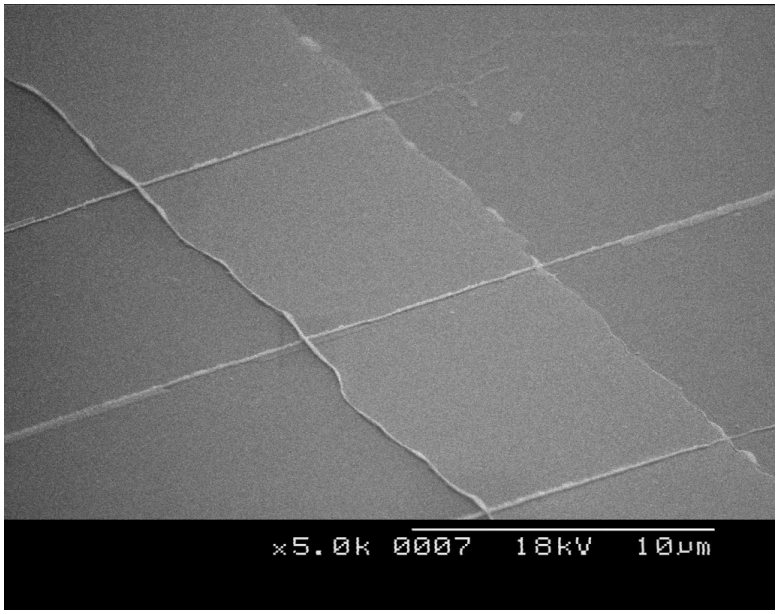

Figure 7.29 *– Crossover of phase shift Ti-TiO_x-Pt diode*

Due to the lift-off process, the edge roughness of the phase shifted lines would result in reduced yield if used as a base layer in diode production, which is why the phase shifted lines were used as top layer, as then the edge profile of the platinum layer does not affect the functionality of the diodes. The yield of the diodes is limited by the ability to align the sub-micron lines with the contact pad and by the number of defect in those lines, neither of which have posed significant issues.

Phase Shift Lithography Furnace Diodes

These devices were also successful electrically as diodes, as can be seen from a typical J-V graph in Figure 7.30. This diode has a zero bias curvature coefficient of 1.3 V^{-1} and a forward to reverse current ratio of 1.4. These values are comparable with results published by others [26].

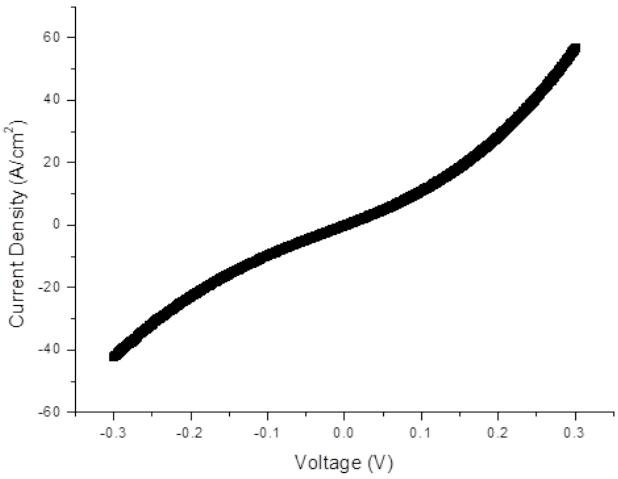

Figure 7.30 *– 4 hour furnace phase shifted diode*

Phase Shift Lithography Plasma Oxidation Diodes

In order to improve yield as well as electrical characteristics, plasma oxidation of the titanium was applied to the phase shift diodes. Figure 7.31 shows a good J-V characteristic for a phase shifted diode, with asymmetry and non-linearity comparable to previous, larger diodes [55].

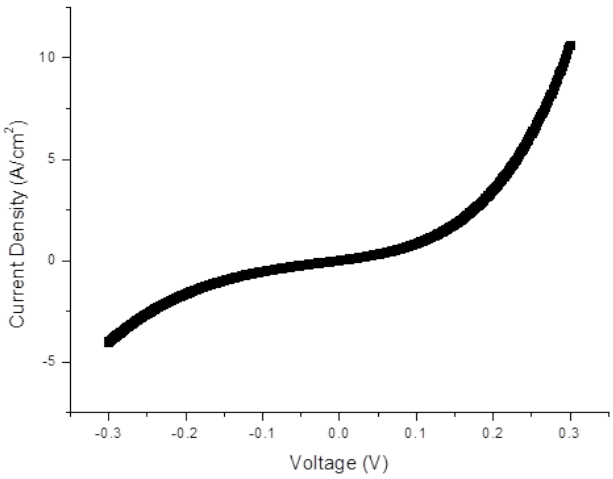

Figure 7.31 *– Phase shifted plasma oxidised diode*

It has been found that a peak current density of $100\,\mathrm{A\,cm^{-2}}$ or smaller is consistent with a diode with good rectifying capabilities, as confirmed by the

curvature coefficient and forward to reverse current ratio. The zero bias curvature coefficient of this diode is 4.1 V^{-1}, with a biased curvature coefficient of 12.5 V^{-1}. The diode also has a forward to reverse current ratio of 2.6, which is comparable with the results from the larger diodes, a typical J-V of which can be seen in Figure 7.32, with a zero bias curvature coefficient of 3.3 V^{-1} and a forward to reverse current ratio of 2.1.

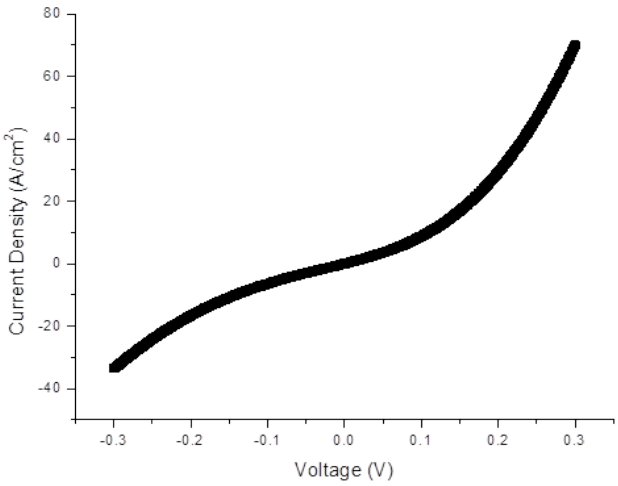

Figure 7.32 – 300 W *50 % O_2 plasma* 9 µm x 9 µm *diode*

7.4.5 Extrapolating Results for Smaller Diodes

The cut-off frequency of the diodes should scale with surface area, so although nanoscale diodes cannot be produced, their cut-off frequency can be estimated. The relative permittivity range can be used to determine the cut off frequency for given cross-sectional areas. By combining Equation 4.16 and Equation 4.15, Equation 7.5 can be derived.

$$f_c = \frac{d}{2\pi R_A \epsilon_0 \epsilon_r A} \tag{7.5}$$

Assuming an oxide thickness of 5 nm, an antenna resistance of 50 Ω, a permittivity ϵ_r in the range 15 to 25 , and a desired operating frequency of 62.5 THz (as discussed in Chapter 3) the desired area for the diodes would be 1.15×10^{-15} to 1.90×10^{-15} m^2, or a feature size of 34 to 44 nm.

7.5 Failure Mechanisms

Throughout the fabrication and analysis of the metal-oxide-metal diodes, numerous factors became apparent in their failure, including: static discharge, lifespan, current stressing, DC voltage breakdown and electrical annealing. Each of these must be fully understood in order to prolong the functionality and lifespan of the devices.

7.5.1 Lifespan Testing

Lifespan tests took place, which involved leaving the devices in atmosphere and being periodically I-V tested to see if their characteristics changed with time and no other external influence. Initially, the current of furnace oxidised diodes would drop by 80 % from the original values within the first 24 to 48 hours, as previously discussed and seen in Figure 6.29.

With modifications to the fabrication process, namely a thicker platinum layer and the annealing of the oxide layer, this improved to a 10 % drop in normalised current over a 2 week period. One possible solution is that the thicker platinum could have resulted in reduced diffusion of oxygen to the oxide layer and that the annealing step has restructured any oxide defects such that it is more robust to the effects of the environment, thus reducing the change in normalised current. Based on the assumption that interaction with the environment is causing this effect, it is possible that this initial degradation could be further reduced by encapsulating devices to isolate them.

7.5.2 Current Stressing

As can be seen in Chapter 6, following current stressing tests the furnace based diodes shown in Figure 6.28 show a 10 % drop in normalised current over 18000 cycles, compared to a 65 % drop in the Hoofring data, as previously discussed. This has further been improved through the annealing of plasma oxides, which show a significantly lower degradation of 2 % over a much larger number of cycles, as confirmed in collaborative work with an undergraduate project student. Furthermore, current stressed diodes have a higher breakdown voltage value than unstressed diodes, thus

implying that the changes to the oxide as a result of current stressing makes them more robust.

7.5.3 DC Voltage Breakdown

The diodes were then tested by applying a DC voltage significantly higher than they are usually tested at until some for a breakdown occurred. A typical I-V curve for these diodes can be seen in Figure 7.33, prior to any breakdown testing taking place.

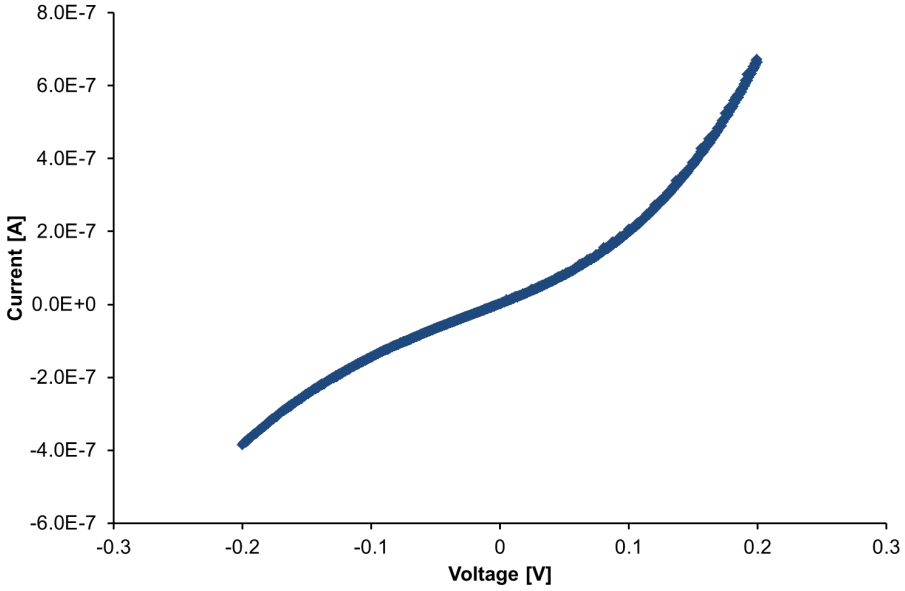

Figure 7.33 – *A standard I-V curve for an anneal Ti/TiO_x/Pt diode*

Figure 7.34 then shows the I-V characteristic which commonly occurred as a result of higher voltages being applied. On annealed devices, the diode does not form an open circuit or short circuit as a result of extreme voltage but instead increases in resistance, which is in contrast to previous furnace oxidised diodes. The initial discontinuities appear to be the diode being damaged and reverting to a resistor/short circuit regime, but then with further applied voltage, and therefore heat, the resistance suddenly increases and a non-linear regime occurs.

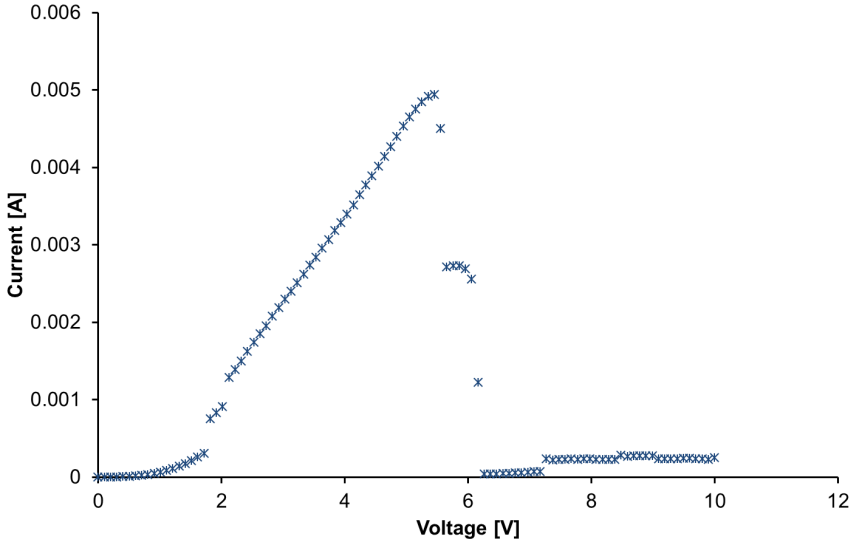

Figure 7.34 – *Breakdown curve for typical diode*

Furthermore, as seen in Figure 7.35, the device continues to function as a diode, but in a high voltage regime and in reverse polarity.

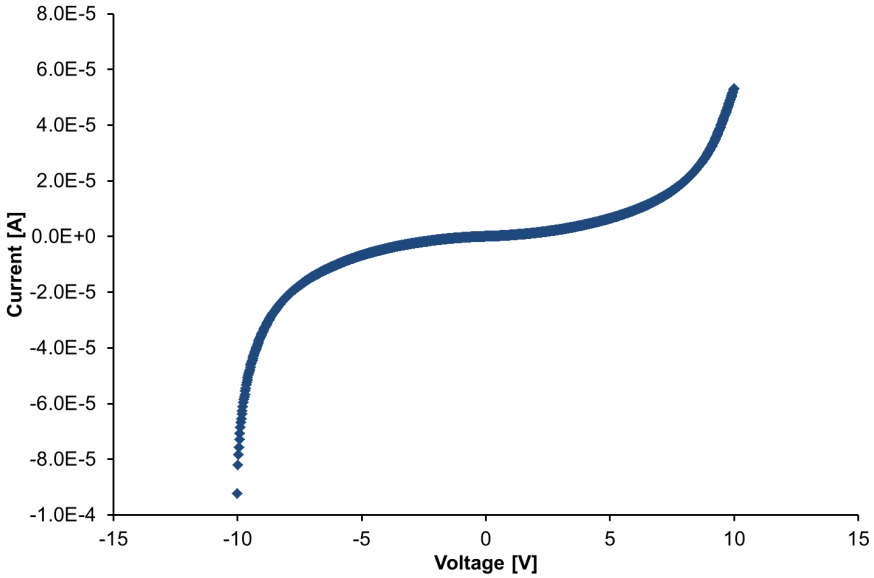

Figure 7.35 – *I-V characteristics of diode after breakdown has occurred*

Figure 7.36 shows SEM images of breakdown diodes. The top left image shows a device prior to testing, the top right shows a 'bubble' formed in the titanium layer, the bottom left shows a close-up of the bubble and the bottom right image shows the remaining electrical connection responsible for conduction. It is believed that

these 'bubbles' form during the high voltage testing due to thermal expansion of the metal combined with adhesion issues with the substrate. As the heating increases, the bubble expands until the point at which the maximum stress within the bubble exceeds the breakdown stress and it tears at the maximum stress point, i.e. over the top of the bubble. The device still conducts due to a very small region at the edge of the bubble which is still connected.

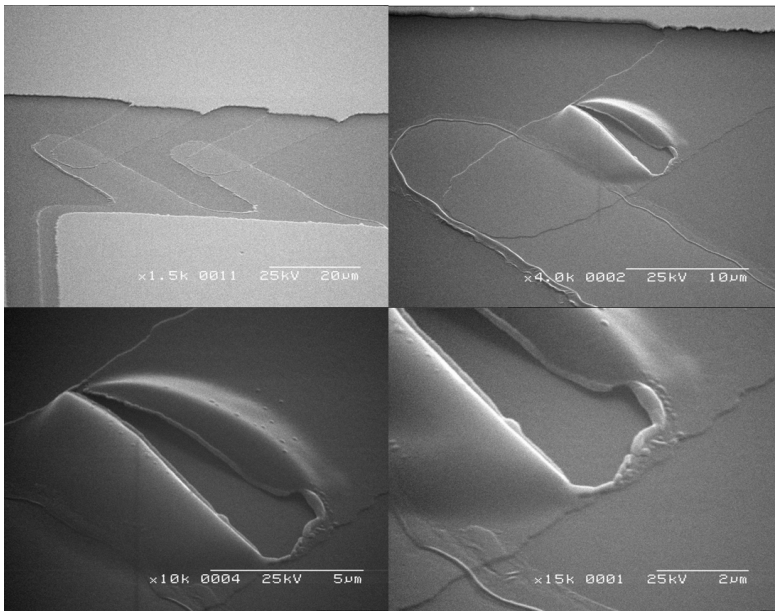

Figure 7.36 *– SEM images of breakdown diodes - (top left) a device prior to testing, (top right) a 'bubble' formed in the titanium layer, (bottom left) a close-up of the bubble, (bottom right) the remaining electrical connection responsible for conduction*

The subsequent I-V characteristic, seen in Figure 7.35, is believed to be due to a combination of the original I-V characteristic and the high resistance connection next to the bubble which will be limiting the current through the crossover region. Either this high resistance region is ohmic and the inversion has taken place in the crossover, or the diode crossover had been unaffected by the high voltage and the high resistance link is non-linear and the combination of the two results in the I-V seen. A non-linear region here is feasible as the increased temperature could have caused the titanium at this point to oxidise.

Energy-Dispersive X-Ray Spectroscopy (EDX)

On occasions where bubbles do not form on the surface of the titanium substrate, an alternative effect occurs, which can be seen in Figure 7.37. Figure 7.37 is an AFM image of the crossover seen in Figure 7.38, with the region shown in the AFM image highlighted by a red square.

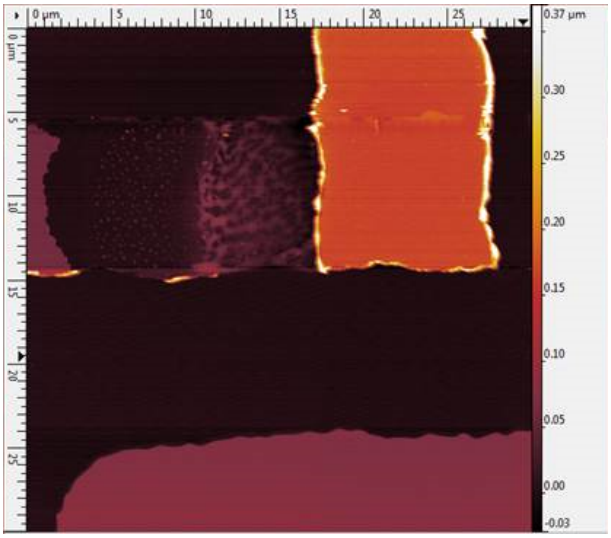

Figure 7.37 *– AFM of damage to diode crossover*

Instead of a bubble forming, the titanium first forms small bubbles, then the area nearest the crossover begins to warp and the oxygen concentration becomes non-uniform.

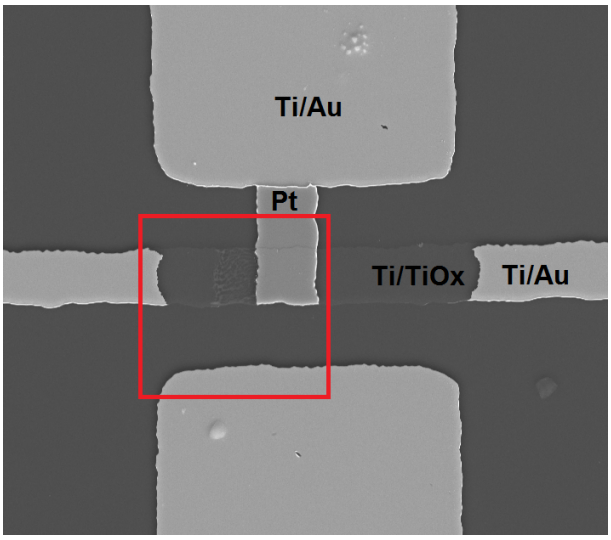

Figure 7.38 *– AFM of damage to diode crossover*

Energy-dispersive X-ray spectroscopy (EDX) was used to confirm the oxygen variation caused by the high voltages. Figure 7.39 shows the the various samples taken in the 'dark' regions of the affected region, with an average of the oxygen and titanium weight percentages summarised in Table 7.12 (with the standard deviation of each reading shown in brackets).

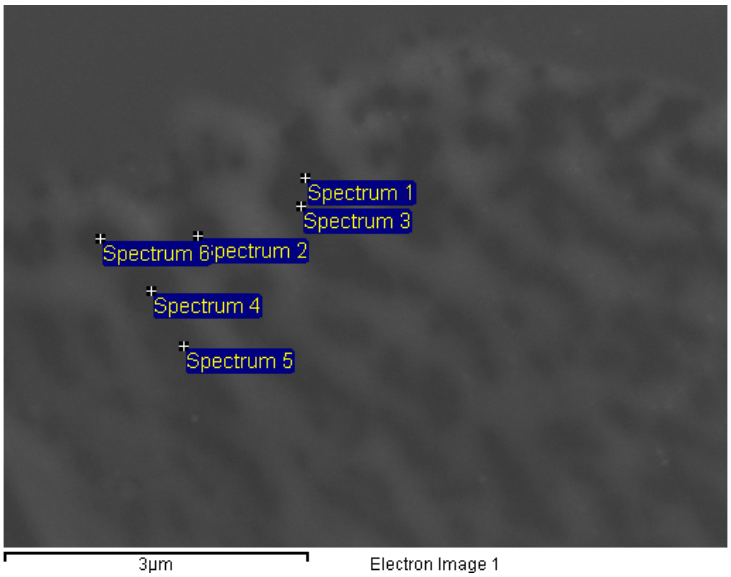

Figure 7.39 *– EDX of 'dark' regions within the oxide*

Figure 7.40 shows the samples taken in the 'light' region, again with the averaged results visible in Table 7.12.

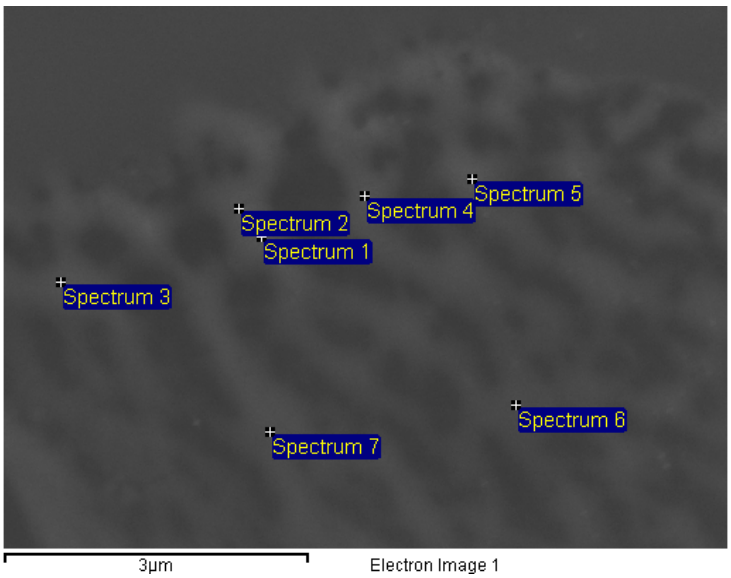

Figure 7.40 *– EDX of 'light' regions within the oxide*

As can be seen in Table 7.12, the dark regions of the sample have a significantly higher oxygen concentration than the light regions, 95.8 % compared to 84.2 %, which explains why they appear darker on the SEM image, as they are more insulating.

Table 7.12 *– EDX summary*

Region	Oxygen Percentage	Titanium Percentage
Dark	95.8 (1.1)	4.2 (1.1)
Light	84.2 (1.8)	15.8 (1.8)

A summary of the diode comparison can be found in Table 7.13. The phase shifted diode results are comparable with the 50 % anneal plasma diode results, with the best curvature coefficients being 5.9 V^{-1} on the plasma diode and 5.8 V^{-1} on the phase shifted diode. The current ratios are also comparable with a range of 1.6 to 2.6 versus the 2.1 of the plasma diode. The current density of the plasma diode is significantly lower than other diodes produced at 0.4 to 8 $A\,cm^{-2}$, where others have been in the range 1 to 20 $A\,cm^{-2}$. This is most likely due to difficulties in accurately measuring the diode crossover area rather than a true variation between standard plasma diodes and phase shifted plasma diodes.

Table 7.13 *– Diode summary*

Parameter	4 Hour Furnace Diode	100 % Plasma Diode	50 % Anneal Plasma Diode	Phase Shifted Furnace Diode	Phase Shifted Plasma Diode
Oxidation	Wet furnace oxide (4 hour 100 °C)	100 % O_2 Plasma (no anneal)	50 % O_2 Annealed Plasma	50 % O_2 Annealed Plasma	50 % O_2 Annealed Plasma
Oxide Thickness [nm]	7.6	4.0	4.2	4.2	4.2
Diode Cross Section (typical) [μm^2]	80	80	1 to 9	4	4
Peak Current Density [$A\,cm^{-2}$]	1 to 100	1 to 135	1 to 20	50 to 200	0.4 to 8
Voltage Test Range [V]	±0.3	±0.3	±0.2	±0.2	±0.2
Typical Curvature Coefficient [V^{-1}]	3.1	2.8	3.9	1.1	1.9
Best Curvature Coefficient [V^{-1}]	6.8	2.9	5.9	1.3	5.8
Current Ratio (at ±0.2 V)	1.7 to 3.5	1.7	2.1	1.3	1.6 to 2.6
Capacitance [pF]	1.3 to 2.5	4.9 to 5.8	0.18 to 2 pF	n/a	n/a
Relative Permittivity	11.5 to 26.5	20.1 to 28.1	9.9 to 32.3	n/a	n/a

7.6 Oxide Layer Development Conclusion

In Chapter 6, diodes were produced using a furnace oxidation method, however; the oxide layer was not optimised. In this chapter, oxide layer development took place. A plasma etch and regrowth of the oxide with a 100 % oxygen plasma was used during the fabrication process. These diodes were fabricated and analysed [108] but the oxidation process was not very repeatable, batch to batch, due to the high oxygen content within the plasma. Therefore, in order to improve the plasma oxidation process, the oxygen concentration was reduced with the addition of argon into the plasma chamber. This resulted in more control over the thickness of the oxide layer, with higher plasma powers being needed to achieve similar thicknesses as were produced previously with the 100 % concentration oxygen plasma.

Additional improvements in the oxide took place as a result of investigating the effect of temperature during a post oxidation annealing step. This resulted in diodes which were both uniform and repeatable, which was verified both electrically and physically, as can be seen in Table 7.13. The DC and AC results were confirmed through Matlab simulation, which used the polynomials from the best fit curve on an I-V trace to predict the voltage and current responsivity of a particular diode.

Finally, a diode size reduction took place via a novel phase shift lithography technique, with features sizes of 200 nm being produced using standard lithographic equipment. Furthermore, extrapolation of the cut-off frequencies has shown that, using this oxide, these diodes would have a sufficiently high cut off frequency such that they would be able to successfully rectify near infrared radiation, if they were fabricated with features sizes in the range 34 to 44 nm, which is possible.

The aim hereafter would be to incorporate the diodes with suitable antennas, with the impedance matching of the antenna and diode being of the highest importance. However, a combination of experimental analysis, comparison with theoretical values and simulations have shown that the diodes produced here are competitive and they would, if made small enough, be able to rectify high frequency radiation.

Chapter 8

Conclusions and Future Work

This work has provided a comprehensive coverage of the fabrication of metal-oxide-metal (MOM) diodes for high frequency rectification. The key results from this thesis are:

- Diodes have been produced with zero bias curvature coefficients that are competitive with those from other international groups [26, 56, 58, 80]
- The oxide layer has been optimised in thickness, uniformity and stoichiometry for the use in these devices using a plasma etch and regrowth method
- A novel method of small feature production, phase shift lithography, has been adapted using a positive photoresist for lift-off fabrication of MOM diode features
- The application for such a device has been determined; single wavelength devices could have efficiencies approaching 100 %
- Given the current cut-off frequency results, if the devices were made smaller they could operate sufficiently fast to rectify terahertz radiation

8.1 Conclusions

There is demand for a device, which can detect and/or recover infrared radiation in a large range of applications, which was discussed in detail in Chapter 2. Various

technologies exist but they have disadvantages. A possible alternative is the rectenna array, which consists of an antenna and diode combination. Antenna designs have a huge impact on device efficiency but once designed the fabrication of these antennas involves standard lithography practices and therefore this project has focussed on the other component in this device, i.e. the diode.

Many different diodes with different conduction mechanisms exist and they vary in their suitability (mainly determined by their speed/voltage requirements). As can be seen from the conduction mechanisms, only certain ones are desirable, namely the tunnelling mechanisms due to their inherent speed. Therefore, any diodes produced should aim to achieve tunnelling in some form. In order to do this the diodes must have a thin oxide.

Subsequently, MOM diodes using a Ti/TiO_x/Pt metallurgy, and a simple titanium oxidation technique, have been fabricated and tested. Initial diodes showed DC electrical results which are among the best published, as well as a high yield of working devices, despite the susceptibility of the diodes to static damage. It has also been shown that care must be taken when using data extracted from polynomial fits to quote results. Physical analysis of the titanium oxide shows that the oxide is thicker than our aim and also not very uniform. Furthermore, it actually consists of a number of different oxides, as confirmed by ToFSIMS. In order to produce an effective diode we need a better oxide. However, the initial diode production has established the Ti/TiO_x/Pt diode as a 'successful' diode, as well as acting as a vehicle for electrical and physical testing procedures.

Initial fabrication of diodes using a furnace oxidation method provided diodes which were successful but the oxide layer was not optimised. As a result, oxide layer development took place. Initially 100 % oxygen plasma diodes were fabricated and discussed but the high oxygen level resulted in a process which was not as repeatable as required. This process was then improved by reducing the oxygen concentration with the addition of argon into the plasma chamber, resulting in higher powers being needed to produce diodes, as well as gaining more control over the oxide thickness as a function of the plasma power.

Further improvements were found as a result of investigating the effect of the

temperature of a post-oxidation anneal step, which resulted in diodes, which were more uniform and repeatable, with these findings confirmed using both electrical and physical analysis. Finally, a size reduction took place, with extrapolation of the cut-off frequency showing that using this oxide these diodes would be fast enough to rectifying terahertz radiation if they were fabricated with feature sizes in the range of 34 to 44 nm, which is possible. The coupling of the antenna impedance and diode impedance would still have to be considered, however.

A summary of all of the diode types and a comparison between their zero bias resistance and zero bias curvature coefficient can be seen in Figure 8.1

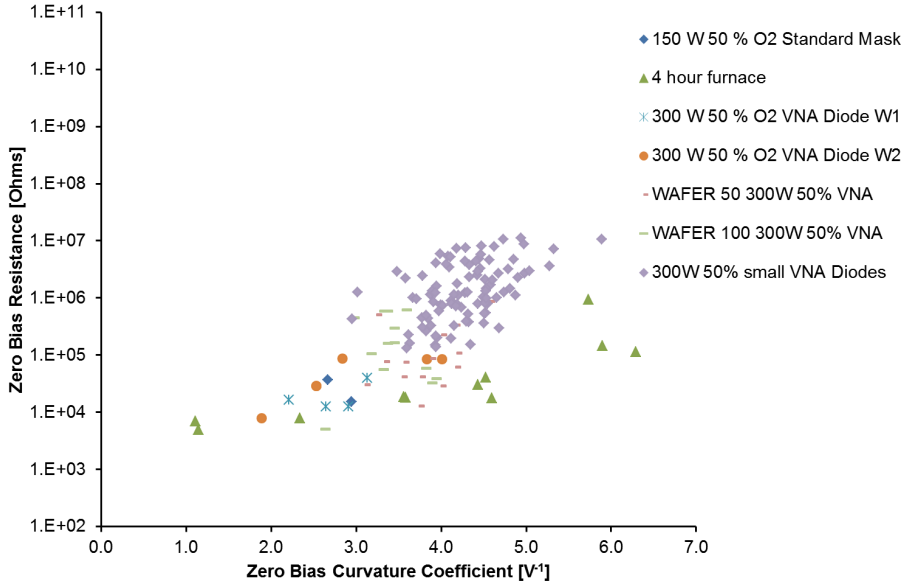

Figure 8.1 – *Diode Summary showing resistance versus zero bias curvature coefficient*

As can be seen, the two most successful types of diodes are the 300 W 50 % "small VNA Diodes" with features down to 1 µm and the 4 hour furnace diodes, although the furnace diodes have a very variable curvature coefficient. The plasma diode are consisted in both resistance and curvature. These diode results were then compared to results published by [26], which can be seen in Figure 8.2.

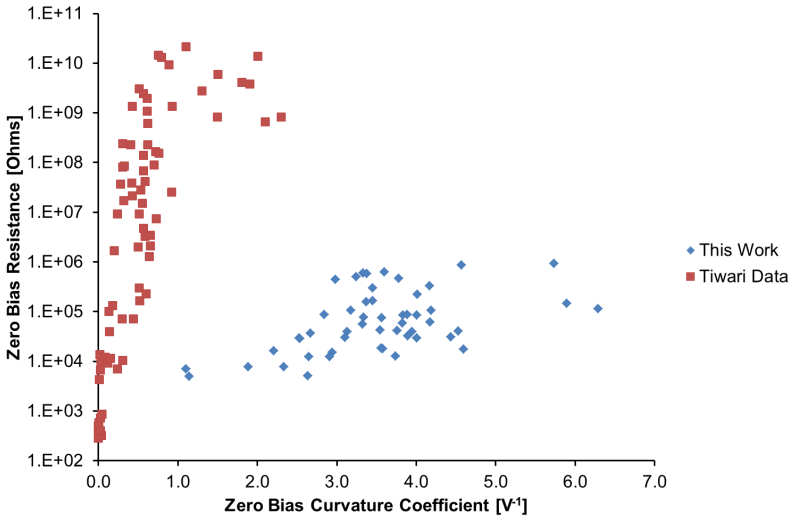

Figure 8.2 – *Resistance versus zero bias curvature presented by Tiwari et al. compared to diodes presented here*

Results by Tiwari *et al.* show a variation in resistance over 8 orders of magnitude, with a maximum zero bias curvature coefficient of $2.3\,\mathrm{V}^{-1}$, compared to the diodes from this project having a variation in resistance across 3 order of magnitude at the lower end of the scale and a maximum zero bias curvature coefficient of over $6\,\mathrm{V}^{-1}$. This improved repeatability is further confirmed by Figure 8.3 which shows a strong correlation between zero bias curvature coefficient and the forward to reverse current ratio for the reduced size diodes. It is worth noting that the resistance will be higher in the Tiwari results due to the smaller crossover regions. However, the comparison in variation between the two sets of results is valid.

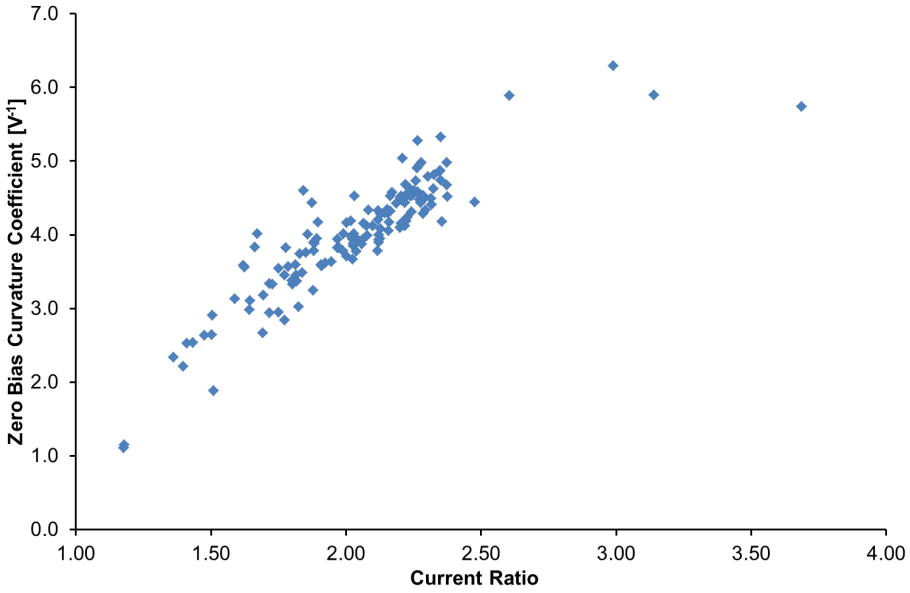

Figure 8.3 – *A typical CC-current ratio for the reduced size diodes*

As can be seen the results of this project compare favourably with published results and are repeatable based on their DC electrical results. The AC measurements also appear both realistic and promising. The capacitance and permittivity results were confirmed using COMSOL Multiphysics analysis and the current ratio. Furthermore, the electrical results were further confirmed by the findings of the physical results, with a uniform thin oxide being measured by both TEM and ToFSIMS analyses.

8.2 Future Work

8.2.1 2D Phase Shift Lithography and Larger Scale Production

Diodes which are sub-micron in one dimension have been achieved and have been proven as diodes by their I-V characteristic. The phase shifted process could be repeated but in two dimensions, resulting in smaller diode areas of approximately 400 nm by 400 nm, although the fabrication process would involve careful thought in order to ensure the correct design of masks and suitable alignment/etching considerations. This process could be used to make masters for NIL, which would

be the larger scale process for diode production at a later time.

Once this is achieved testing with radiation could take place, followed by the rectenna devices being configured into small arrays and finally large scale production. Temperature considerations need to be taken into account as cryostat data shows that high temperatures reduce diode effectiveness

Once this is achieved larger scale production could take place using roll to roll technology to produce arrays of these devices on flexible substrates which could then be wrapped around radiation sources in order to provide a detection capability.

8.2.2 Detectivity and Efficiencies

One of the major challenges associated with the successful conversion of the radiation into useful power is the efficiency issues with the conversion. The detectivity equation, Equation 8.1 (originally seen in Chapter 3) details four efficiencies which must be considered.

$$D^* = \frac{(A_{\text{ant}}\Delta f)^{0.5}}{NEP}\eta_a\eta_s\eta_c\eta_j \tag{8.1}$$

The antenna efficiency (η_a) should be easy to accommodate through intelligent antenna design. The propagation efficiency (η_s) should be able to be maximised by positioning the antenna as close to each other as possible, or one on top of the other, which again should be relatively simple. However the two remaining efficiencies, the coupling efficiency (η_c) and the junction efficiency (η_j) (i.e. the Carnot efficiency - which as discussed is a function of the temperature difference between the source and the diode, as well as the bandwidth of the incident radiation) required further consideration. Maximising the coupling efficiency involves trying to impedance match the antenna and diode, which could be difficult to do repeatably due to the the 3 orders of magnitude resistance variation, seen in Figure 8.3. Furthermore, typical antenna impedances are either 50 Ω or 100 Ω, which is significantly lower than the diode resistances achieved currently. Finally, the junction efficiency involves the efficiency associated with electron tunnelling through the diode junction. Currently, the oxide thickness of 4.2 nm combined with the conduction mechanism results imply

that the oxide is quite thick for high efficiency electron tunnelling to occur and that alternative mechanisms might be partially responsible, resulting in a decrease in efficiency across the junction. This issue could be partially resolved by using a thinner oxide layer but plasma growth of such an oxide layer could be difficult. Therefore, a technology such as Atomic Layer Deposition (ALD) could be used to provide a sufficiently thin layer which also has more easily chosen parameters, such as relative permittivity, more suited to this project. However, it is possible that this impedance mismatched device, despite low efficiencies, could be used to just detect infrared radiation rather than recover it, where the efficiency is less vital to the operation of the device. It would simply mean that the device would be limited with regards to its minimum detectable signal.

References

[1] D.P. DeWitt and F.P. Incropera, *Introduction To Heat Transfer*. John Wiley and Sons Inc., 1996, no. 0-471-30458-1.

[2] H.C. Ohanian, *Physics*. W.W. Norton and Company Inc., 1989, no. 0-393-95825-6.

[3] L. Ho, M. Pepper and P. Taday, "Terahertz spectroscopy: Signatures and fingerprints," *Nature Photonics*, vol. 2, no. 12, pp. 541–543, 2008. [Online]. Available: http://dx.doi.org/10.1038/nphoton.2008.174

[4] F. Stabler, "Automotive Thermoelectric Generators: Design and Manufacturing," in *Symposium N: Material and Devices for Thermal-to-Electric Energy Conversion, Proc. MRS Spring Meeting*. San Francisco, California, USA, 13 April 2009, p. 9.

[5] BMW, "BMW Technology Guide: Brake Energy Regeneration," http://www.bmw.com/com/en/insights/technology/technology_guide/articles/mm_brake_energy_regeneration.html, Accessed online: 8 January 2013.

[6] J. Erion, "LEDs in Exterior Vehicle Lighting," *Photonics Spectra*, vol. 40, no. 12, pp. 50–52, December 2006. [Online]. Available: http://www.photonics.com/Article.aspx?AID=27518

[7] W. Jansen, [Email], Coventry: Jaguar Land Rover, March 2009.

[8] Jaguar Cars Ltd., *Jaguar XJ V8 Series Model Guide*, 1998, p. 3.

[9] Practical Action, "Diesel Engines," http://practicalaction.org/practicalanswers/product_info.php?products_id=34, Accessed online: 28 April 2010.

[10] Car Pages, "Toyota Yaris TR 1.4 D-4D Specification," http://www.carpages.co.uk/guide/toyota/toyota-yaris-tr-1.4-d-4d-5dr.asp, Accessed online: 28 April 2010.

[11] InfoVision Technologies Inc., "Technical Brief: Thermoelectric thermal regulation systems," http://electronics-cooling.com/articles/1996/may/may96_tb.php, May 1996, Accessed online: 3 September 2009.

[12] British Geological Survey, *World Mineral Production 2005-09*, 2011, p. 95.

[13] OICA. (2011) Production statistics. [Online]. Available: http://oica.net/category/production-statistics/

[14] F. Stabler, "Benefits of thermoelectric technology for the automobile," in *DOE Thermoelectric applications workshop.* San Diego, California, USA, 2011.

[15] W.M. Yang, S.K. Chou, C. Shu, Z.W. Li, and H. Xue, "Research on micro-thermophotovoltaic power generators," *Solar Energy Materials and Solar Cells*, vol. 80, no. 1, pp. 95–104, October 2003. [Online]. Available: http://dx.doi.org/10.1109/JSEN.2008.920715

[16] W.M. Yang, S.K. Chou, C. Shu, H. Xue and Z.W. Li, "Research on micro-thermophotovoltaic power generators with different emitting materials," *Journal of Micromechanics and Microengineering*, vol. 15, no. 9, pp. S239–S242, September 2005. [Online]. Available: http://dx.doi.org/10.1088/0960-1317/15/9/S11

[17] W.M. Yang, S.K. Chou, C. Shu, H. Xue, Z.W. Li, D.T. Li and J.F. Pan, "Microscale combustion research for application to micro thermophotovoltaic systems," *Energy Conversion and Management*, vol. 44, no. 16, pp. 2625–2634, September 2003. [Online]. Available: http://dx.doi.org/10.1016/S0196-8904(03)00024-4

[18] H. Shao, W. Li, A. Torfi, D. Moscicka, and W.I. Wang, "Room-temperature inassb photovoltaic detectors for mid-infrared applications," *IEEE Photonics Technology Letters*, vol. 18, pp. 1756–1758, July-August 2006. [Online]. Available: http://dx.doi.org/10.1109/LPT.2006.879941

[19] L.C. Chia and B. Feng, "The development of a micropower (micro-thermophotovoltaic) device," *Journal of Power Sources*, vol. 165, no. 1, pp. 455–480, February 2007. [Online]. Available: http://dx.doi.org/10.1016/j.jpowsour.2006.12.006

[20] W.M. Yang, D.Y. Jiang, S.K. Chou, K.J. Chua, K. Karthikeyan and H. An, "Experimental study on micro modular combustor for micro-thermophotovoltaic system application," *International Journal of Hydrogen Energy*, vol. 37, no. 12, p. 95769583, June 2012. [Online]. Available: http://dx.doi.org/10.1016/j.ijhydene.2012.03.129

[21] R. Corkish, M.A. Green and T. Puzzer, "Solar energy collection by antennas," *Solar Energy*, vol. 73, no. 6, pp. 395–401, December 2002. [Online]. Available: http://dx.doi.org/10.1016/S0038-092X(03)00033-1

[22] B. Berland, "Photovoltaic technologies beyond the horizon: Optical rectenna solar cell," *National Renewable Energy Laboratory*, February 2003, contract number: DE-AC36-99-GO10337.

[23] R.L. Bailey, P.S. Callahan and M. Zahn, "Electromagnetic wave energy conversion research," 1975, NASA-CR-145876 (76N-13591).

[24] A.M. Marks, "Device for conversion of light power to electric power," *US patent no.: 4445050*, April 1984, United States of America.

[25] A. M. Marks, "Femto diode and applications," *US patent no.: 4720642*, January 1988, United States of America.

[26] B. Tiwari, J.A. Bean, G.H. Bernstein, P. Fay and W. Porod, "Thermal infrared detection using dipole antenna-coupled metal-oxide-metal diodes," *Journal of*

Vacuum Science and Technology B, vol. 27, no. 1, pp. 11–14, January-February 2009. [Online]. Available: http://dx.doi.org/10.1116/1.3039684

[27] C. Fumeaux, W. Herrmann, F.K. Kneubuhl, and H. Rothuizen, "Nanometer thin-film Ni-NiO-Ni diodes for detection and mixing of 30 THz radiation," *Infrared Physics and Technology*, vol. 39, no. 3, pp. 123–183, April 1998. [Online]. Available: http://dx.doi.org/10.1016/S1350-4495(98)00004-8

[28] E.R. Brown, A.W.M. Lee, B.S. Navi, and J.E. Bjarnason, "Characterization of a planar self-complementary square-spiral antenna in the THz region," *Microwave and Optical Technology Letters*, vol. 48, no. 3, pp. 524–529, March 2006. [Online]. Available: http://dx.doi.org/10.1002/mop.21398

[29] J. Bean, *Thermal Infrared Detection Using Antenna-Coupled Metal-Oxide-Metal Diodes.* Notre Dame, Indiana, USA: PhD Thesis, 2008.

[30] P. Esfandiari, G. Bernstein, P. Fay, W. Porod, B. Rakos, A. Zarandy, B. Berland, L. Boloni, G. Boreman, B. Lail, B. Monacelli and A. Weeks, "Tunable Antenna-Coupled Metal-Oxide-Metal (MOM) Uncooled IR Detector," *Infrared Technology and Application XXXI, Proceedings of the Society of Photo-Optical Instrumentation Engineerings (SPIE)*, vol. 5783, pp. 470–482, June 2005. [Online]. Available: http://dx.doi.org/10.1117/12.606874

[31] P. Horowitz and W. Hill, *The Art of Electronics.* The Pitt Building, Trumpington Street, Cambridge, CB2 1RP: Cambridge University Press, 1993, ch. 7, pp. 433–434.

[32] B.M. Kale, "Electron tunneling devices in optics," *Optical Engineering*, vol. 24, no. 2, pp. 267–274, April 1985.

[33] S. Joshi and G. Moddel, "Efficiency limits of rectenna solar cells: Theory of broadband photon-assisted tunneling," *Applied Physics Letters*, vol. 102, February 2013. [Online]. Available: http://dx.doi.org/10.1063/1.4793425

[34] W. Feist and G. Wade, "Thermodynamical Limits on the Bandwidth and Conversion Efficiency of Incoherent Recombination Radiation from a

Semiconductor Diode," *Journal of Applied Physics*, vol. 41, no. 4, pp. 1799–1804, September 1969. [Online]. Available: http://dx.doi.org/10.1063/1.1659106

[35] D. Wood, *Optoelectronic Semiconductor Devices.* UK: Prentice Hall, 1994, ch. 2, pp. 33–58.

[36] H. Bentarzi, *Transport in Metal-Oxide-Semiconductor Structures.* Berlin, Germany: Springer, 2011, ch. 4, p. 30.

[37] S. Sze and K. Ng, *Physics of Semiconductor Devices.* USA: Wiley Interscience, 2007, ch. 7, p. 232.

[38] R. Eisberg and R. Resnick, *Quantum Physics of Atoms, Molecules, Solids, Nuclei, and Particles.* USA: John Wiley & Sons, 1985, ch. 6, pp. 199–214.

[39] J.G. Simmons, "Electric tunnel effect between dissimilar electrodes separated by a thin insulating film," *Journal of Applied Physics*, vol. 34, no. 9, pp. 2581–2590, September 1963. [Online]. Available: http://dx.doi.org/10.1063/1.1729774

[40] M. Depas, B. Vermeire, P.W. Mertens, R.L. Van Meirhaeghe and M.M. Heyns, "Determination of Tunnelling Parameters in ultra-thin oxide layer poly-Si/SiO_2/Si Structures," *Solid State Electronics*, vol. 38, no. 8, pp. 1465–1471, August 1995. [Online]. Available: http://dx.doi.org/10.1016/0038-1101(94)00269-L

[41] A. Gehring, "Simulation of tunneling in semiconductor devices." [Online]. Available: http://www.iue.tuwien.ac.at/phd/gehring/node62.html

[42] J. Indrek, *Conduction Mechanisms in Thin Atomic Layer Deposited Films Containing TiO_2*, 2007.

[43] M.K. Massey, C. Pearson, D.A. Zeze, B.G. Mendis and M.C. Petty, "The electrical and optical properties of oriented Langmuir-Blodgett films of single-walled carbon nanotubes," *Carbon*, vol. 49, no. 7, pp. 2424–2430, June 2011. [Online]. Available: http://dx.doi.org/10.1016/j.carbon.2011.02.009

[44] P. Dimitrakis, P. Normand, D. Tsoukalas, C. Pearson, J.H. Ahn, M.F. Mabrook, D.A. Zeze, M.C. Petty, K.T. Kamtekar, C. Wang, M.R. Bryce and M. Green, "Electrical behaviour of memory devices based on fluorene-containing organic thin films," *Journal of Applied Physics*, vol. 104, August 2008. [Online]. Available: http://dx.doi.org/10.1063/1.2968551

[45] A.S. Jombert, K.S. Coleman, D. Wood, M.C. Petty and D.A. Zeze, "Poole-Frenkel conduction in single wall carbon nanotube composite films built up by electrostatic layer-by-layer deposition," *Journal of Applied Physics*, vol. 104, November 2008. [Online]. Available: http://dx.doi.org/10.1063/1.3006015

[46] W.T. Read, "A proposed high frequency, negative-resistance diode," *Bell System Technical Journal*, vol. 37, no. 2, pp. 401–446, March 1958. [Online]. Available: http://dx.doi.org/10.1002/j.1538-7305.1958.tb01527.x

[47] B. Streetman and S. Banerjee, *Solid State Electronic Devices*. New Jersey, USA: Prentice Hall, 2006, ch. 10, pp. 508–518.

[48] A. Westlund, G. Moshchetti, H. Zhao, P.A. Nilsson and J. Grahn, "Fabrication and DC characterization of InAs/AlSb Self-Switching Diodes," *Proc. 2012 International Conference on Indium Phosphide and Related Materials*, pp. 65–68, August 2012. [Online]. Available: http://dx.doi.org/10.1109/ICIPRM.2012.6403320

[49] A.M. Song, "Self-switching diode," http://personalpages.manchester.ac.uk/staff/A/Song/research/SelfSwitchingDevice.htm, Accessed online: 14 August 2009.

[50] K.Y. Xu, X.F. Lu, A.M. Song and G. Wang, "Enhanced terahertz detection by localized surface plasma oscillations in a nanoscale unipolar diode," *Journal of Applied Physics*, vol. 103, no. 11, June 2008. [Online]. Available: http://dx.doi.org/10.1063/1.2937175

[51] C. Balocco, S.R. Kasjoo, L.Q. Zhang, Y. Alimi and A.M. Song, "Low-frequency noise of unipolar nanorectifiers," *Applied Physics Letters*, vol. 99, September 2011. [Online]. Available: http://dx.doi.org/10.1063/1.3636437

[52] C. Balocco, M. Halsall, N.Q. Vinh and A.M. Song, "THz operation of asymmetric-nanochannel devices," *Journal of Physics Condensed Matter*, vol. 20, August 2008. [Online]. Available: http://dx.doi.org/10.1088/0953-8984/20/38/384203

[53] C. Balocco, S.R. Kasjoo, X.F. Lu, L.Q. Zhang, Y. Alimi, S. Winner and A.M. Song, "Room-temperature operation of unipolar nanodiode at terahertz frequencies," *Applied Physics Letters*, vol. 98, May 2011. [Online]. Available: http://dx.doi.org/10.1063/1.3595414

[54] S. P. Kwok, G. I. Haddad and G. Lobov, "Metal-oxide-metal (M-O-M) detector," *Journal of Applied Physics*, vol. 42, no. 2, pp. 554–563, July 1970. [Online]. Available: http://dx.doi.org/10.1063/1.1660062

[55] L.E. Dodd, A.J. Gallant and D. Wood, "Ti-TiOx-Pt Metal-Oxide-Metal Diodes Fabricated via a Simple Oxidation Technique," *Proc. Material Research Society Meeting*, vol. 1415, pp. 41–46, November 2011. [Online]. Available: http://dx.doi.org/10.1557/opl.2012.72

[56] M.R. Abdel-Rahman, F.J. Gonzalez and G.D. Boreman, "Antenna-coupled metal-oxide-metal diodes for dual-band detection at 92.5 GHz and 28 THz," *Electronics Letters*, vol. 40, no. 2, pp. 116–118, January 2004. [Online]. Available: http://dx.doi.org/10.1049/el:20040105

[57] J. Karlovsky, "The curvature coefficient of germanium tunnel and backward diodes," *Solid State Electronics*, vol. 10, no. 11, pp. 1109–1111, November 1967. [Online]. Available: http://dx.doi.org/10.1016/0038-1101(67)90131-1

[58] J.A. Bean, A. Weeks and G. D. Boreman, "Performance optimization of antenna-coupled Al/AlO_x/Pt tunnel diode infrared detectors," *IEEE Journal of Quantum Electronics*, vol. 47, no. 1, pp. 126–135, January 2011. [Online]. Available: http://dx.doi.org/10.1109/JQE.2010.2081971

[59] B. Rakos, H, Yang, J.A. Bean, G.H. Bernstein, P. Fay, A.I. Csurgay and W. Porod, "Investigation of Antenna-Coupled MOM Diodes for Infrared

Sensor Applications," *Nonequilibrium Carrier Dynamics in Semiconductors: Proceedings of the 14th International Conference*, vol. 110, pp. 105–108, July 2005. [Online]. Available: http://dx.doi.org/10.1007/978-3-540-36588-4_23

[60] K. Choi, F. Yesilkoy, G. Ryu, S.H. Cho, N. Goldsman, M. Dagenais and M. Peckerar, "A Focused Asymmetric MetalInsulatorMetal Tunneling Diode: Fabrication, DC Characteristics and RF Rectification Analysis," *IEEE Transactions on Electron Devices*, vol. 58, no. 10, pp. 3519–3528, October 2011. [Online]. Available: http://dx.doi.org/10.1109/TED.2011.2162414

[61] J.L. Hesler and T.W. Crowe, "Responsivity and Noise Measurements of Zero-Bias Schottky Diode Detectors," *Proc. 18th International Symposium on Space Terahertz Technology*, pp. 844–845, March 2007.

[62] M. Bareiβ, D. Kälblein, C. Jirauschek, A. Exner, I. Pavlichenko, B. Lotsch, U. Zschieschang, H. Klauk, G. Scarpa, B. Fabel, W. Porod and P. Lugli, "Ultra-thin titanium oxide," *Applied Physics Letters*, vol. 101, August 2012. [Online]. Available: http://dx.doi.org/10.1063/1.4745651

[63] M. Lenzlinger and E.H. Snow, "Fowler-Nordheim tunneling into thermally grown SiO_2," *Journal of Applied Physics*, vol. 40, no. 1, pp. 278–283, January 1969. [Online]. Available: http://dx.doi.org/10.1063/1.1657043

[64] V. I. Denisov, V. F. Zakhar'yash, V. M. Klement'ev and S. V. Chepurov, "Very-high-speed metal-oxide-metal diodes on W-Ni, Pt-Ti, and Pt-W contacts," *Instruments and Experimental Techniques*, vol. 50, no. 4, pp. 517–523, November 2007. [Online]. Available: http://dx.doi.org/10.1134/S002044120704015X

[65] B.L. Yang, P.T. Lai and H. Wong, "Conduction mechanisms in MOS gate dielectric films," *Microelectronics Reliability*, vol. 44, no. 5, pp. 709–718, May 2004. [Online]. Available: http://dx.doi.org/10.1016/j.microrel.2004.01.013

[66] J. Maserjian and N. Zamani, "Behavior of the Si/SiO_2 interface observed by Fowler-Nordheim tunneling," *Journal of Applied Physics*,

vol. 53, no. 1, pp. 559–567, January 1982. [Online]. Available: http://dx.doi.org/10.1063/1.329919

[67] M. Bareiβ, A. Hochmeister, G. Jegert, U. Zschieschang, H. Klauk, R. Huber, D. Grundler, W. Porod, B. Fabel, G. Scarpa and P. Lugli, "Printed array of thin-dielectric metal-oxide-metal (MOM) tunneling diodes," *Journal of Applied Physics*, vol. 110, August 2011. [Online]. Available: http://dx.doi.org/10.1063/1.3615952

[68] T. W. Hickmott, "Defect conduction bands, localization, and temperature-dependent electron emission from Al-Al_2O_3-Au diodes," *Journal of Applied Physics*, vol. 108, November 2010. [Online]. Available: http://dx.doi.org/10.1063/1.3504220

[69] J.J. Huang, C.W. Kuo, W.C. Chang and T.H. Hou, "Transition of stable rectification to resistive-switching in Ti/TiO_2/Pt oxide diode," *Applied Physics Letters*, vol. 96, June 2010. [Online]. Available: http://dx.doi.org/10.1063/1.3457866

[70] W.F. Brinkman, R. C. Dynes and J.M. Rowell, "Tunneling conductance of asymmetrical barriers," *Journal of Applied Physics*, vol. 41, no. 5, pp. 1915–1921, April 1970. [Online]. Available: http://dx.doi.org/10.1063/1.1659141

[71] W. Y. Park, G. H. Kim, J. Y. Seok, K. M. Kim, S. J. Song, M. H. Lee and C. S. Hwang, "A Pt/TiO_2/Ti Schottky-type selection diode for alleviating the sneak current in resistance switching memory arrays," *Nanotechnology*, vol. 21, April 2010. [Online]. Available: http://dx.doi.org/10.1088/0957-4484/21/19/195201

[72] M.K. Lee, H.C. Lee and C.H. Hsu, "High dielectric constant titanium oxide grown on amorphous silicon by metal-organic chemical vapour deposition," *Semiconductor Science and Technology*, vol. 21, pp. 604–607, March 2006. [Online]. Available: http://dx.doi.org/10.1088/0268-1242/21/5/006

[73] V. Bessergenev, "High-temperature anomalies of dielectric constant in TiO_2 thin films," *Materials Research Bulletin*, vol. 44, no. 8, pp. 1722–1728, August

2009. [Online]. Available: http://dx.doi.org/10.1016/j.materresbull.2009.03.014

[74] L. Zhou, R.C. Hoffmann, Z. Zhao, J. Bill and F. Aldinger, "Chemical bath deposition of thin TiO_2-anatase films for dielectric applications," *Thin Solid Films*, vol. 516, no. 21, pp. 7661–7666, September 2008. [Online]. Available: http://dx.doi.org/10.1016/j.tsf.2008.02.042

[75] Phiar Corporation, "Thin-film devices based on metal-insulator tunnel junctions," *A New Technology for Terahertz Electronics*, 2003. [Online]. Available: http://ecee.colorado.edu/~moddel/QEL/MIIM_Overview.pdf

[76] B. Hegyi, A. Csurgay and W. Porod, "Investigation of the nonlinearity properties of the DC I-V characteristics of metal-insulator-metal (MIM) tunnel diode with double-layer insulators," *Journal of Computational Electronics*, vol. 6, no. 1-3, pp. 159–162, September 2007. [Online]. Available: http://dx.doi.org/10.1007/s10825-006-0083-9

[77] S. Krishnan, E. Stefanakos and S. Bhansali, "Effects of dielectric thickness and contact area on current-voltage characteristics of thin film metal-insulator-metal diodes," *Thin Solid Films*, vol. 516, no. 8, pp. 2244–2250, February 2008. [Online]. Available: http://dx.doi.org/10.1016/j.tsf.2007.08.067

[78] B. Tiwari, J.A. Bean, G. Szakmany, G.H. Bernstein, P. Fay and W. Porod, "Controlled etching and regrowth of tunnel oxide for antenna-coupled metal-oxide-metal diodes," *American Vacuum Society*, vol. 27, pp. 2153–2160, August 2009. [Online]. Available: http://dx.doi.org/10.1116/1.3204979

[79] M. Bareiβ, A. Hochmeister, G. Jegert, G. Koblmüller, U. Zschieschang, H. Klauk, B. Fabel, G. Scarpa, W. Porod and P. Lugli, "Energy harvesting using nano antenna array," *Proc. 11th IEEE International Conference on Nanotechnology*, pp. 218–221, August 2011. [Online]. Available: http://dx.doi.org/10.1109/NANO.2011.6144516

[80] E.C. Kinzel, R.L. Brown, J.C. Ginn, B.A. Lail, B.A. Slovick and G.D. Boreman, "Design of an MOM diode-coupled frequency-selective surface,"

Microwave and Optical Technology Letters, vol. 55, no. 3, pp. 489–493, March 2013. [Online]. Available: http://dx.doi.org/10.1002/mop.27363

[81] I. Hotovy, D. Donoval, J. Huran, S. Hascik, L. Spiess, M. Gubisch and S. Capone, "NiO nanostructured film with Pt coating prepared by magnetron sputtering," *Czechoslovak Journal of Physics*, vol. 56, no. 2, pp. B1192–B1198, May 2006. [Online]. Available: http://dx.doi.org/10.1007/s10582-006-0349-2

[82] G. Droulers, A. Beaumont, J. Beauvais and D. Drouin, "Spectroscopic ellipsometry on thin titanium oxide layers grown on titanium by plasma oxidation," *Journal of Vacuum Science and Technology B*, vol. 29, no. 2, March/April 2011. [Online]. Available: http://dx.doi.org/10.1116/1.3553209

[83] R. Ratnadurai, S. Krishnan, E. Stefanakos, D. Y. Goswami and S. Bhansali, "Effects of dielectric deposition on the electrical characteristics of MIM tunnel junctions," *Proc. Eurosensors XXIV, Linz, Austria*, vol. 5, pp. 1059–1062, September 2010. [Online]. Available: http://dx.doi.org/10.1016/j.proeng.2010.09.292

[84] Y. Rawal, S. Ganguly and M. S. Baghini, "Fabrication and characterization of new Ti-TiO_2-Al and Ti-TiO_2-Pt tunnel diodes," *Active and Passive Electronic Components*, vol. 2012, Feruary 2012. [Online]. Available: http://dx.doi.org/10.1155/2012/694105

[85] M. Sreemany, A. Bose and S. Sen, "A study on structural, optical, electrical and microstructural properties of thin TiO_x films upon thermal oxidation: Effect of substrate temperature and oxidation temperature," *Physica B*, vol. 405, pp. 85–93, January 2010. [Online]. Available: http://dx.doi.org/10.1016/j.physb.2009.08.031

[86] Y. Katsuta, A.E. Hill A.M. Phahle and J.H. Calderwood, "D.C. and A.C. conduction in amorphous titanium dioxide thin films," *Thin Solid Films*, vol. 18, no. 1, pp. 53–62, October 1973. [Online]. Available: http://dx.doi.org/10.1016/0040-6090(73)90220-4

[87] E. McCafferty and J.P. Wightman, "An x-ray photoelectron spectroscopy sputter profile study of the native air-formed oxide film on titanium," *Applied Surface Science*, vol. 143, no. 1-4, pp. 92–100, December 1998. [Online]. Available: http://dx.doi.org/10.1016/S0169-4332(98)00927-1

[88] S. Krishnan, Y. Emirov, S. Bhansali, E. Stefanakos and Y. Goswami, "Thermal stability analysis of thin film Ni-NiO_x-Cr tunnel junctions," *Thin Solid Films*, vol. 518, no. 12, pp. 3367–3372, October 2009. [Online]. Available: http://dx.doi.org/10.1016/j.tsf.2009.10.021

[89] Y. Chen, J. Nayak, H. Ko and J. Kim, "Effect of annealing temperature on the characteristics of ZnO thin films," *Journal of Physics and Chemistry of Solids*, vol. 73, no. 11, pp. 1259–1263, November 2012. [Online]. Available: http://dx.doi.org/10.1016/j.jpcs.2012.06.007

[90] Y. Irokawa, "Hydrogen interaction with GaN metal-insulator-semiconductor diodes," *Physica B*, vol. 407, no. 15, pp. 2957–2959, August 2012. [Online]. Available: http://dx.doi.org/10.1016/j.physb.2011.08.054

[91] Nanowerk. (2013) Probing the resolution limits of electron-beam lithography. [Online]. Available: http://www.nanowerk.com/spotlight/spotid=29714.php

[92] M. Okada, T. Kishiro, K. Yanagihara, M. Ataka, N. Anazawa and S. Matsui, "Newly developed electron beam stepper for nanoimprint mold fabrication," *Journal of Vacuum Science and Technology B*, vol. 28, no. 4, pp. 740–743, July 2010. [Online]. Available: http://dx.doi.org/10.1116/1.3449270

[93] R. Inanami, T. Ojima, K. Matsuki, T. Kono and T. Nakasugi, "Sub-100 nm pattern formation by roll-to-roll nanoimprint," *Proc. SPIE*, vol. 8323, March 2012. [Online]. Available: http://dx.doi.org/10.1117/12.916584

[94] D. Lide, *CRC Handbook of Chemistry and Physics 74th Edition.* USA: CRC Press, 1994, ch. 12, p. 105.

[95] E. Atanassova and A. Paskaleva, "Breakdown fields and conduction mechanisms in thin Ta_2O_5 layers on Si for high density DRAMs,"

Microelectronics Reliability, vol. 42, no. 2, pp. 157–173, February 2002. [Online]. Available: http://dx.doi.org/10.1016/S0026-2714(01)00248-7

[96] Y.M. Zhang, R. Han, Y. Kim, D.Y. Kim, H. Shichijo, S. Sankaran, C.Y. Mao, E. Seok, D. Shim and K.O. Kenneth, "Schottky Diodes in CMOS for Terahertz Circuits and Systems," *IEEE 13th Topical Meeting on Silicon Monolithic Integrated Circuits in RF Systems*, pp. 24–26, January 2013. [Online]. Available: http://dx.doi.org/10.1109/SiRF.2013.6489420

[97] TeraSense. (2010) Impatt sub-thz generators. [Online]. Available: http://terasense.com/products/impatt-sub-thz-generators/

[98] A. Khalid, C. Li, V. Papageorgiou, G.M. Dunn, M.J. Steer, I.G. Thayne, M. Kuball, C.H. Oxley, M. Montes Bajo, A. Stephen, J. Glover and D.R.S. Cumming, "$In_{0.53}Ga_{0.47}As$ planar Gunn diodes operating at a fundamental frequency of 164 GHz," *IEEE Electron Device Letters*, vol. 34, no. 1, pp. 39–41, January 2013. [Online]. Available: http://dx.doi.org/10.1109/LED.2012.2224841

[99] K.J. Siemsen and H.D. Riccius, "Experiments with point-contact diodes in the 30-130 THz region," *Applied Physics A*, vol. 35, no. 3, pp. 177–187, November 1984. [Online]. Available: http://dx.doi.org/10.1007/BF00616972

[100] Microchem, "LOR and PMGI Resists," http://microchem.com/pdf/PMGI-Resists-data-sheetV-rhcedit-102206.pdf, Accessed online: 1 October 2012.

[101] Rohm and Haas Electronic Materials, "Megaposit SPR350 Series Photoresist Datasheet," http://www.dow.com/products/market/electronics-and-communications/product-line/megaposit-spr/.

[102] J. A. Rogers, K. E. Paul, R. J. Jackman and G. M. Whitesides, "Using an elastomeric phase mask for sub-100 nm photolithography in the optical near field," *Applied Physics Letters*, vol. 70, no. 20, pp. 2658–2660, May 1997. [Online]. Available: http://dx.doi.org/+10.1063/1.118988

[103] J. Aizenberg, J. A. Rogers, K. E. Paul and G. M. Whitesides, "Imaging profiles of light intensity in the near field: applications to phase-shift photolithography," *Applied Optics*, vol. 37, no. 11, pp. 2145–2152, April 1998. [Online]. Available: http://dx.doi.org/10.1364/AO.37.002145

[104] Oxford Instruments. (2011) Optistat dn. [Online]. Available: http://www.chem.ucla.edu/~craigim/pdfmanuals/appnotes/OI565.pdf

[105] D. H. Williams and I. Fleming, *Spectroscopic Methods in Organic Chemistry*. McGraw-Hill Higher Education, 2007.

[106] A.B. Hoofring and V.J. Kapoor, "Submicron nickel-oxide-gold tunnel diode detectors for rectennas," *Journal of Applied Physics*, vol. 66, pp. 430–437, March 1989. [Online]. Available: http://dx.doi.org/10.1063/1.343841

[107] Y.X. Weng, Y.Q. Wang, J.B. Ashbury, H.N. Ghosh and T. Lian, "Back Electron Transfer from TiO_2 Nanoparticles to $Fe^{III}(CN)_6^{3-}$: Origin of Non-Single-Exponential and Particle Size Independent Dynamics," *Journal of Physical Chemistry B*, vol. 104, no. 1, pp. 93–104, November 1999. [Online]. Available: http://dx.doi.org/10.1021/jp992522a

[108] L.E. Dodd, A.J. Gallant and D. Wood, "Controlled reactive ion etching and plasma regrowth of titanium oxides of known thickness for production of metal-oxide-metal (MOM) diodes," *IET Micro and Nano Letters*, vol. 8, no. 8, p. 476 478, August 2013. [Online]. Available: http://dx.doi.org/10.1049/mnl.2013.0177